2 MINERνA Physics Goals and Detector Design Drivers

The MINERνA neutrino scattering experiment in the NuMI beam offers a unique opportunity to explore a broad spectrum of physics topics. Some have never been studied systematically, while others are plagued by sparse data with large statistical and systematic errors. The complete MINERνA physics program will include high-statistics studies of all the topics listed below. These studies are important for both the elementary particle and nuclear physics communities, providing information complementary to JLab studies with charged leptons in the same kinematic range.

1. Precision measurement of the quasi-elastic neutrino–nucleus cross-section, including its E_ν and q^2 dependence, and study of the nucleon axial form factors. Over **800 K** events are expected in the fiducial volume during a four-year MINERνA run.
2. Determination of cross-sections in the resonance-dominated region for both neutral-current (NC) and charged-current (CC) interactions, including study of isospin amplitudes, measurement of pion angular distributions, isolation of dominant form factors, and measurement of the effective axial mass. A total of **1.6M** one-pion events make up the low-W resonance sample.
3. Precision measurement of coherent single-pion production cross-sections, with particular attention to target A-dependence. NC coherent pion production is a significant background for next-generation of neutrino oscillation experiments probing $\nu_\mu \rightarrow \nu_e$ oscillation. A sample of **85 K** CC events is expected off carbon. The expected NC sample is roughly half the CC sample.
4. Examination of nuclear effects in neutrino interactions, including final-state modifications in heavy nuclei, by employing carbon, iron and lead targets. These effects play a significant role in neutrino oscillation experiments measuring ν_μ disappearance as a function of E_ν. It has recently been suggested that, for a given Q^2, shadowing can occur at much lower energy transfer (ν) for neutrinos than for charged leptons. This effect is unaccounted for in neutrino event generators. With sufficient $\overline{\nu}$ running, a study of flavor-dependent nuclear effects can also be performed. Due to the different mix of quark flavors, this is another way in which neutrino and charged-lepton nuclear effects differ. MINERνA will collect over **1.5M** CC events off both iron and lead, in addition to the carbon sample.
5. Study of nuclear effects on $\sin^2\theta_W$ measurements, and the NC/CC ratio for different nuclear targets.
6. Exploration of the W (hadronic mass) transition region where resonance production merges with deep-inelastic scattering (DIS), testing phenomenological models like quark/hadron duality. A sample of **2.0 M** multi-pion events is expected with W $\leq$ 2.0 GeV.
7. With a sample of over **4.1 M** CC DIS events, a much-improved measurement of the parton distribution functions, particularly at large x_{Bj}, will be possible using a measurement of all three ν structure functions. Although we expect over **100 K** CC $\overline{\nu}$ events in the four year MINERνA ν run, an additional dedicated $\overline{\nu}$ run would be required to measure the three $\overline{\nu}$ structure functions with similar precision.
8. Examination of the leading exponential contributions of perturbative QCD.
9. With nearly **230 K** fully reconstructed exclusive events, precision measurement of exclusive strange-production channels near threshold. This will significantly improve our knowledge of backgrounds in nucleon-decay searches. Also, determination of V_{us}, and searches for

strangeness-changing neutral-currents and candidate pentaquark resonances will be undertaken Measurement of hyperon-production cross-sections, including hyperon polarization, is feasible with exposure of MINERνA to $\overline{\nu}$ beams.

10. Improved determination of the effective charm-quark mass (m_c) near threshold, and new measurements of V_{cd}, $s(x)$ and, independently, $\overline{s}(x)$.

These are worthy research topics in their own right, and improved knowledge in most is essential to minimizing systematic uncertainties in neutrino-oscillation experiments.

2.1 Physics Driven Detector Requirements

To accomplish these physics goals requires a detector with particular attributes. It is not sufficient to simply have a large sample of interactions on the various targets. The kinematics of the events have to be reconstructed with sufficient accuracy to be able to determine the dynamics of the interaction.

To meet the physics goals of the experiment, the required resolution of the detector in measuring such kinematic variables as momentum, energy and angle were studied in detail in terms of three physics channels: quasi-elastic scattering, coherent pion production and deeply inelastic scattering. For each of these channels the purity of the final sample of candidates as well as the efficiency for detecting true candidates was measured as a function of the resolution of the detector. Studied were the momentum and angular resolution in the measurement of the outgoing muon in the three charged-current channels, the momentum resolution of stopping tracks for the quasi-elastic channel, the resolution of the measurement of hadronic energy showers and finally the resolution in the total visible energy of the interacting neutrino.

The details of the studies will be found in the following sections covering each of the channels: section 2.2 on Quasi-elastic scattering, section 2.4 on coherent pion production and section 2.7 on deeply inelastic scattering. Table 1 is a summary of the resolution studies giving the results for all three channels.

Channel	$\Delta P_\mu/P_\mu$	$\Delta\Theta_\mu$	$\Delta p^{stop}/p^{stop}$	ΔE^{int}	ΔE_ν
Quasi-elastic (Sect. 2.1)		note (a)	≤ 0.05	$\leq 0.3/\sqrt{E_H}$	≤ 0.15, note (b)
Coherent (Sect. 2.3)		$\leq 0.5^\circ$		$\leq 0.20/\sqrt{E_H}$	
DIS (Sect. 2.6)	≤ 0.12				≤ 0.12, note (c)

Table 1: Summary of Physics-driven kinematic variable requirements. Notes: (a) Limits low Q^2 reach, (b) at low E_ν, (c) at high y

The remainder of this section provides more detail, and illustrates the rich physics potential of MINERνA.

2.2 Quasi-Elastic Scattering

2.2.1 Introduction

Quasi-elastic scattering dominates the total ν–N interaction rate in the threshold regime $E_\nu \leq 2$ GeV. Precision measurement of the cross-section for this reaction, including its energy dependence and variation with target nuclei, is essential to current and future neutrino-oscillation experiments.

2.2.2 Nucleon Form-factors in Quasi-elastic Scattering

MINERνA's large quasi-elastic samples will probe the Q^2 response of the weak nucleon current with unprecedented accuracy. The underlying V-A structure of this current includes vector and axial-vector form-factors. The essential formalism is given in reference [12].

$$< p(p_2)|J^+_\lambda|n(p_1) >= \overline{u}(p_2)\left[\gamma_\lambda F_V^1(q^2) + \frac{i\sigma_{\lambda\nu}q^\nu \xi F_V^2(q^2)}{2M} + \gamma_\lambda\gamma_5 F_A(q^2)\right] u(p_1),$$

where $q = k_\nu - k_\mu$, $\xi = (\mu_p - 1) - \mu_n$, and $M = (m_p + m_n)/2$. Here, μ_p and μ_n are the proton and neutron magnetic moments. The pseudoscalar form-factor is not shown since it is small for ν_μ.

The vector part of this matrix element can be expressed using $G_E^p(q^2)$, $G_E^n(q^2)$, $G_M^p(q^2)$, and $G_M^n(q^2)$. It has been generally assumed that the q^2 dependence of these form-factors can be described by the dipole approximation:

$$G_D(q^2) = \frac{1}{\left(1 - \frac{q^2}{M_V^2}\right)^2}, \quad M_V^2 = 0.71 \text{ (GeV/c)}^2, \quad F_A(q^2) = \frac{g_A}{\left(1 - \frac{q^2}{M_A^2}\right)^2}$$

$$G_E^p = G_D(q^2), \quad G_E^n = 0, \quad G_M^p = \mu_p G_D(q^2), \quad G_M^n = \mu_n G_D(q^2).$$

As discussed below, the dipole parameterization is far from perfect. MINERνA will be able to measure deviations of F_A from this form. In general, the axial form-factor $F_A(q^2)$ can only be extracted from quasi-elastic neutrino scattering.[1]

2.2.3 Vector form-factors

Electron scattering experiments at SLAC and Jefferson Lab (JLab) have measured the proton and neutron electromagnetic (vector) form-factors with high precision. The vector form-factors can be determined from electron scattering cross-sections using the standard Rosenbluth separation technique[13], which is sensitive to (two-photon) radiative corrections, or from polarization measurements using the newer polarization transfer technique[14]. Polarization measurements do not directly measure form-factors, but rather the ratio G_E/G_M. Recently, discrepancies in electron scattering measurements of some vector form-factors have appeared; study of quasi-elastic reactions in MINERνA may help

[1] At low Q^2, below 0.1 (GeV/c)^2, its behavior can also be inferred from pion electroproduction data.

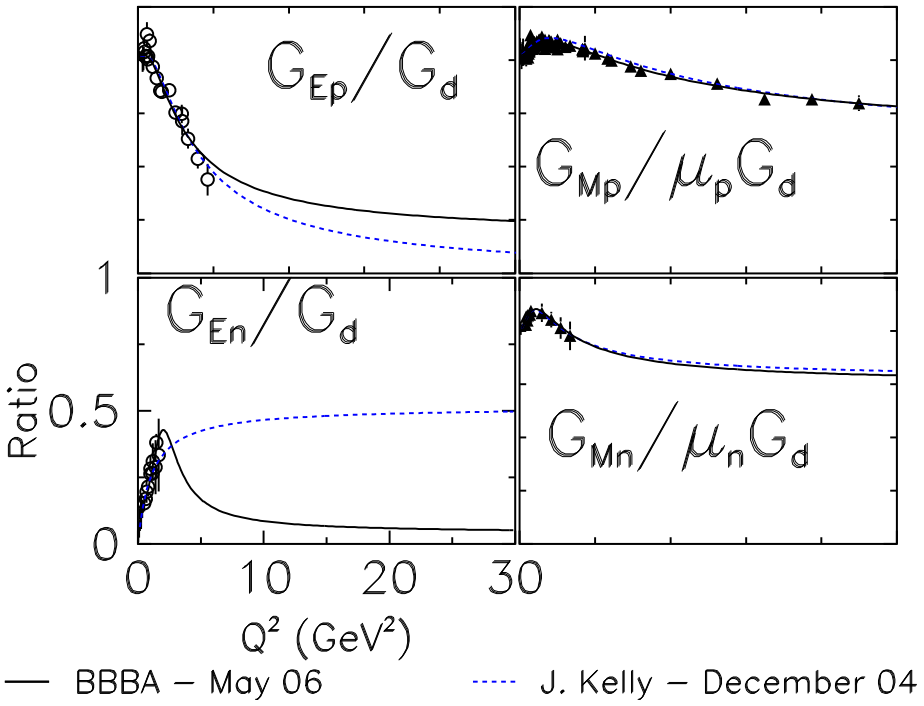

Figure 1: Deviations from dipole approximation are illustrated for two different nucleon form factor parameterizations - J. Kelly [15](dashed Blue) and BBBA05 [16] (solid black). Data are taken from [15].

reveal the origin these discrepancies. Figure 1 shows the BBBA-2005 (Bradford, Bodek, Budd, Arrington 2005) fits. There appears to be a difference between the two methods of measuring this ratio. The newer polarization transfer technique yields a much lower value at high Q^2 and indicates a difference between the electric charge and magnetization distributions. The polarization transfer technique is believed to be more reliable and less sensitive to radiative effects from two-photon corrections. In addition, Figure 1 shows that dipole amplitudes provide only a first-order description of form-factor behavior at high Q^2.

If the electric charge and magnetization distributions of the proton are indeed different, accurate measurement of the axial form-factor's high-Q^2 shape in MINERνA can provide important new input to help resolve differences in electron scattering data.

To obtain the correct neutrino cross-sections [17], the input form-factors must be correct. The Q^2 distribution measured in neutrino scattering is sensitive to both the vector and axial form-factors. However, using an incorrect *axial* form-factor to match the the Q^2 distribution in neutrino scattering

(to compensate for old dipole *vector* form-factors) results in a 6–8% error in the calculated neutrino cross-section. Therefore, updated vector form-factors *and* better-measured axial form-factors are required. MINERνA will measure the Q^2 dependence of F_A in neutrino scattering and compare the calculated cross-section with the measured cross-section.

2.2.4 Axial form-factor

Neutrino scattering provides the only practical route to precision measurement of the axial form-factor above $Q^2 = 0$, and the functional form of $F_A(Q^2)$. The fall-off of the form-factor strength with increasing Q^2 is traditionally parameterized (approximately) using an effective axial-vector mass M_A. Uncertainty in the value of M_A contributes directly to uncertainty in the total quasi-elastic cross-section. Earlier neutrino measurements, mostly bubble-chamber experiments on deuterium, extracted M_A using the best vector form-factors, other parameters, and models available at the time. Changing these input assumptions changes the extracted value of M_A. Hence, precision extractions of M_A and F_A require using the best possible vector form-factors and coupling constants. The value of M_A is $\approx$ 1.00 GeV/c^2, to an accuracy of perhaps 5%. This value agrees with the theoretically-corrected value from pion electroproduction[20], 1.014 ± 0.016 GeV$/c^2$.

The fractional contributions of F_A, G_M^p, G_M^n, G_E^p, and G_E^n to the Q^2 distribution for quasi-elastic neutrino and anti-neutrino scattering cross-sections in energy range of the NuMI beam are shown in Figure 2. The contributions are determined by comparing the BBA-2003 [17] cross-sections with and without each of the form-factors included. MINERνA will be the first systematic study of F_A, which accounts for roughly half of the quasi-elastic cross-section, over the entire range of Q^2 shown in the figure.

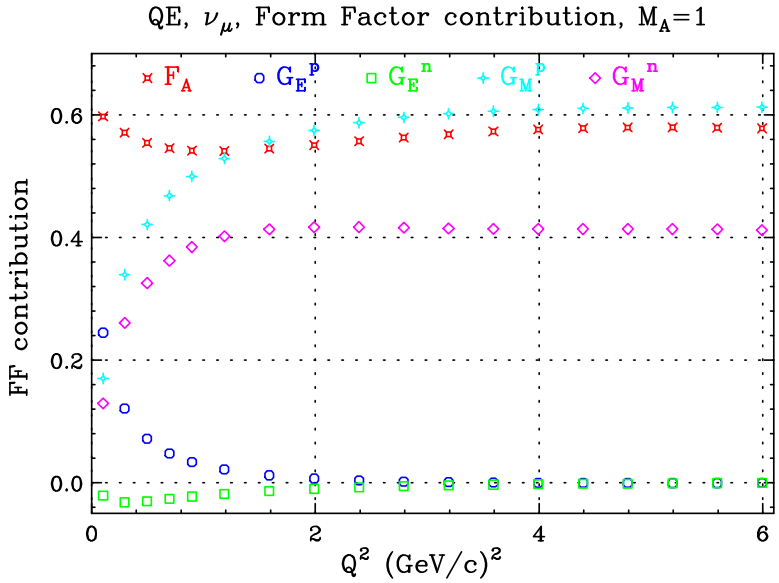

Figure 2: Fractional contributions of G_M^p, G_M^n, G_E^p, G_E^n, and F_A to the Q^2 distributions for quasi-elastic neutrino samples in the energy range of the NuMI beam. Because of interference terms, the sum of the fractions does not necessarily add up to 100%.

2.2.5 Physics of vector and axial form-factors

In deep-inelastic charged-current scattering from quarks, the vector and axial couplings are equal (V-A). Similarly, in electron scattering from quarks (vector current), there is a well-defined ratio between electric and magnetic scattering from point-like Dirac quarks. At low momentum transfers, all of these relations break down. For example in quasielastic and resonant production at very low momentum transfers, the charge and anomalous magnetic moments of the neutron and proton mean the ratio of electric and magnetic scattering for the vector current is not the same as for free quarks. Similarly, from neutron decay, we know that $g_a(Q^2 = 0) = 1.267$ instead of 1.0, so vector and axial scattering differ at $Q^2 = 0$.

There are efforts in progress by lattice gauge programs to calculate the anomalous vector and axial magnetic moments of the proton and neutron, and the Q^2 dependence of all the form-factors in the low- and high-Q^2 regions. The normalization of the magnetic form-factors at Q^2=0 are constrained to equal the charge and anomalous (vector and axial) magnetic moment. The slope at low Q^2 is related to the mean square charge radius of the proton and neutron. The dipole form assumes that the charge and magnetization distributions of the various types of quarks and antiquarks have an exponential form. For Q^2 above 0.5–1.0 (GeV/c)^2 this non-relativistic picture breaks down. The ratio $G_E/\mu G_M \approx 1.0$ (at low Q^2) implies that the charge and magnetization distribution of the proton are the same, but at higher Q^2 the ratio becomes much smaller, and more sophisticated models are required (e.g. lattice gauge theories). Therefore, measurement of the axial form-factor over a wide range of Q^2 is of great interest. In this section, we show MINERνA's sensitivity to three different models of the axial form-factor:

- Model 1: A simple dipole approximation currently used for the magnetic form-factor of the proton, with different axial and vector radii. This is the current standard assumption.
- Model 2: A constitutuent quark model preformed by Wagenbrunn *et al.*[18].
- Model 3: A model based on duality, which requires the axial and vector parts of $W_1^{elastic}$ to be equal above Q^2=0.5 (GeV/c)^2, and therefore increase with Q^2, as described briefly in the next section.

2.2.6 Quark/hadron and local duality

In modern language, the concept of quark-hadron duality can be related to the momentum sum rule in QCD, and various other moments of the structure functions. It has been shown by Bodek and Yang that with inclusion of target mass corrections, NNLO QCD describes deep-inelastic scattering and the average resonant cross-section down to $Q^2 = 0.5$ (GeV/c)^2. The concept of local duality implies that the integral of the QCD predictions (including target mass) in the threshold region up to pion threshold, should be equal to the integral of the elastic peak. Since for QCD, the vector and axial contributions to W_1 and W_2 are equal, local duality predicts that vector and axial part of the quasi-elastic form-factors should become equal around $Q^2 = 0.5$ (GeV/c)^2. This means that the dipole approximation must break down for both vector and axial form-factors.

The vector and axial components of $W_1^{elastic}$ become equal at $Q^2 \sim 0.5$ (GeV/c)^2 for both BBA and dipole form-factors. The requirement that this vector/axial ratio remains equal to 1.0 for higher

Q^2 yields a definite prediction that the axial form-factor is 1.4 times larger than the dipole prediction at higher Q^2.

2.2.7 Axial form-factor measurement in MINERνA

Figure 3 shows a typical quasi-elastic event, as simulated in MINERνA.

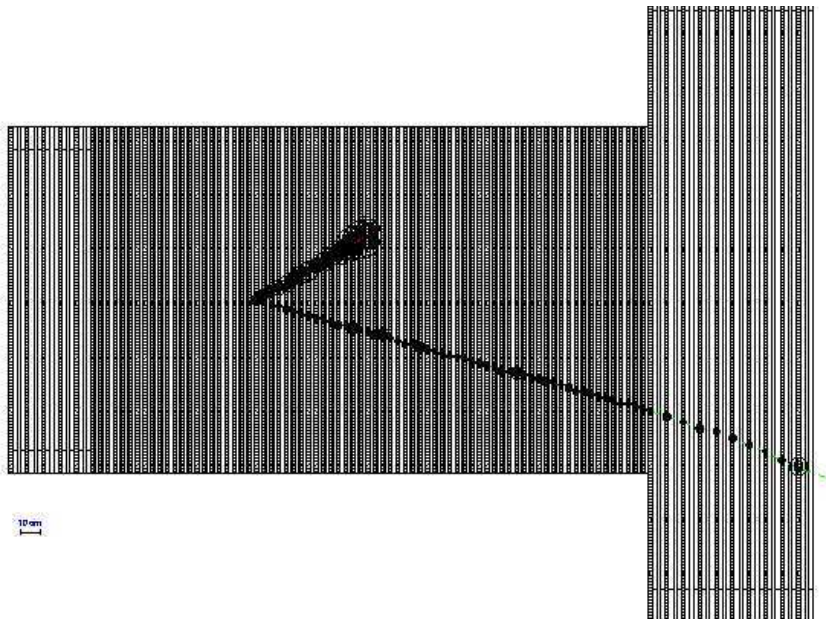

Figure 3: A simulated charged-current quasi-elastic interaction in MINERνA. The proton (upper) and muon (lower) tracks are well resolved. In this display, hit size is proportional to energy loss within a strip. The increased energy loss of the proton as it slows and stops is clear. For clarity the outer detector is not drawn.

In $\nu n \to \mu^- p$, the outgoing proton carries kinetic energy of approximately $Q^2/2M_N$. So for low Q^2, the challenge is identifying events with a very soft recoil proton; for high Q^2, this proton is high energy and may interact in the detector, making particle identification more challenging. The main strategies of the current analysis are:

- At low Q^2, we accept quasi-elastic candidates with a single (muon) track, and require kinematic consistency with $x = 1$.
- At higher Q^2, we reconstruct both the proton and the muon, and require kinematic consistency with $x = 1$ and $p_T^{tot} = 0$

Simple cuts based on these ideas yield reasonable efficiency and good purity, even at high Q^2.

This analysis uses the NEUGEN generator and the hit-level MINERνA detector simulation and tracking package to model signal selection and background processes. The generator uses Fermi smearing and INTRANUKE[19]. INTRANUKE is the procedure used by NEUGEN to simulate the passage of a hadron through dense nuclear matter. It includes the empirically measured phenomena

of π and p re-scattering within the nucleus that can change the momentum vector of the exiting π or p and even eliminate a produced initial-state particle from the observed final state.

Initial event identification requires one or two tracks in the active target. One of these tracks must be non-interacting long range (80 g/cm^2) particle, as expected for a muon. We keep this range requirement low to keep the low energy quasi-elastic events. If a second track forms a vertex with this track, it is assumed to be the proton. No other tracks may be associated with this vertex. If the muon does not range out in the MINERνA , we require the muon to enter MINOS to be able to reconstruct the muon momentum. The main effect of the MINOS requirement is to reduce the acceptance for high Q^2 quasi-elastic events. The muon track momentum is reconstructed with a fractional uncertainty of 5% for muons which range out either in MINERνA or in MINOS and 12% for those muons measured by the magnetic spectrometer in MINOS.

The energy of the proton for the high-Q^2 sample (where the proton almost always interacts) is reconstructed calorimetrically from hits. To get the expected error, we use an expected fractional energy resolution of $4\%/E_{proton} + 18\%/\sqrt{E_{proton}}$. Note that this is only used to calculate the expected error used on Figures 4 and 5.

Although muons are identified by requiring a single long track, no attempt was made to improve particle identification by requiring a dE/dx consistent with the muon or proton tracks. This requirement should be particularly effective for protons of $\mathcal{O}(1)$ GeV momentum[2], and such a requirement can be imposed to optimize the analysis in the future.

If a quasi-elastic interaction is assumed, one can reconstruct the event kinematics from just the momentum and direction of the final state μ. Neglecting the binding energy of the final-state proton,

$$E_\nu^{QE} = \frac{M_N E_\mu - \frac{m_\mu^2}{2}}{M_N - E_\mu + p_\mu \cos\theta_\mu}.$$

If a proton track is identified and its angle and energy are also measured, one can additionally require consistency with the quasi-elastic hypothesis. Two constraints are possible, one on the x of the reconstructed interaction and one on the total p_T of the observed final state.

If the interaction is truly quasi-elastic, then $x = 1$, and therefore $Q^2 = 2M_N\nu$ where ν = E_{had} - M_N, and E_{had} is the energy of the hadronic final state. In this analysis, we test this by comparing Q^2 reconstructed from the lepton kinematics under the quasi-elastic hypothesis to $2M_N\nu$. We form $dx = (Q^2_\mu - 2M_N\nu)/\sigma$ where the σ is the expected 1σ error for dx from the event kinematics. The dominant part of the calculated error σ comes from the smearing of hadronic final-state energy. Figure 4 shows the significance of this Q^2 difference for four Q^2 bins for quasi-elastic, resonant, and deep-inelastic events. This cut can be applied without identifying a proton track if the visible energy, less the muon energy, is assumed to be ν. The efficiencies and purities for the dx cut are shown on the plot for the different Q^2 bins. We note physics from Fermi smearing and INTRANUKE smear dx as much as the detector smearing.

The Q^2 significance cut, dx cut, does not use information on the proton direction. Hence, we impose a second kinematic cut on the total transverse momentum p_T relative to the incoming neutrino direction. If a proton track is identified, we cut on the significance of the difference from $p_T = 0$:

[2] See Chapter 6

Figure 5 shows the significance of this p_T difference for four Q^2 bins for quasi-elastic, resonant and deep-inelastic events. The p_T cuts for the different Q^2 bins are shown on the plot. For $Q^2 < 1$ the p_T cut is not imposed if only one track is found.

2.2.8 Unfolding the Quasi-elastic Q^2 and E_ν Distributions

We have estimated the increase in the statistical errors due to resolution smearing. The limited resolution of the MINERνA detector smears out the measured values of E_ν and θ_μ and hence Q^2. The cross section plot and form factor plots should be in terms of true E_ν and Q^2. The scheme to unfold these distribution is described in [34], and we will use his notation. The quanity we minimize is

$$\chi^2 = (R\mu - n)V^{-1}(R\mu - n) + \alpha * S[f]$$

where $R_{i,j}$ is the response matrix (i - smeared, j - true); n_i is a vector of the data (smeared distribution); μ_j is vector of the true distribution; V is the covarience matrix of the data, $V_{i,j} = \delta_{i,j} n_i$; $S[f]$ is a regularization function; and α is the regulatization parameter. The χ^2 is minimized using Minuit by varing μ_j, the unfolded distribution. The unfolded error increase is the "minos" error in Minuit divided by the unsmeared errors. Without $S[f]$, the solution is $\mu = R^{-1}n$. However, this solution does not give the best answer, as the answer tends to oscillate around. The regularization function, $S[f]$, is added the χ^2 to dampen the oscillations, since physics distributions are supposed to be smooth. This function introduces a bias in the unfolding which one makes smaller than the final statistical error. We use $S[f]$ = sum of $(f''(x))^2 \Delta x$, where f is the true distribution, and Δx is the bin width. Given a unfolded histogram, we determine f with spline fit.

For quasi-elastic events the energy and Q^2 can be calculated from just the muon energy and angle. One can show:

$$\Delta Q^2/Q^2 = (1 + E_\nu/E_\mu)(\Delta E_\mu/E_\mu) + (E_\nu/E_\mu) cot(\theta/2)\Delta\theta$$

$$\Delta E_\nu/E_\nu = (E_\nu/E_\mu)(\Delta E_\mu/E_\mu) + (E_\mu/m) sin(\theta)\Delta\theta$$

and with $E_\nu/E_\mu \sim 1.15$:

$$\Delta Q^2/Q^2 = 2.15(\Delta E_\mu/E_\mu) + 1.15 cot(\theta/2)\Delta\theta$$

$$\Delta E_\nu/E_\nu = 1.15(\Delta E_\mu/E_\mu) + (E_\mu/m) sin(\theta)\Delta\theta$$

For this unfolding result, the muon momentum smearing is given as 5% for $E_\mu < 10GeV$ (for rangeout measurement) and 12% $E_\mu > 10GeV$ (for MINOS magnetic spectrometer measurement). The ΔE_μ terms dominate the smearing as $\Delta\theta \sim .009$. Using the above techniques, we determine the increase in statistical error due to unfolding the smeared distributions.'

2.2.9 Results

Figure 6 shows predictions for the cross-section assuming the BBA-2003 form-factors, with $M_A = 1.00$ (GeV/c)^2. The predicted MINERνA points are shown along with their expected errors. The MIPP experiment will measure particle production off the NuMI target, and from this, we expect

an additional overall uncertainty of 4% from the flux. Figure 6 summarizes current knowledge of neutrino quasi-elastic cross-sections. Among the results shown, there are typically 10–20% normalization uncertainties from knowledge of the fluxes. This plot shows that existing measurements have large errors throughout the E_ν range accessible to MINERνA and especially in the threshold regime crucial to future oscillation experiments.

Figure 7 shows the expected values and errors of F_A in bins of Q^2 for the MINERνA active carbon target, after a four-year exposure in the NuMI beam. The method to extract F_A from $d\sigma/dq^2$ is given in [35]. Clearly the high-Q^2 regime, which is inaccessible to K2K, MiniBooNE and T2K, will be well-resolved in MINERνA. Figure 7 shows these results as a ratio of F_A/F_A(Dipole), demonstrating MINERνA's ability to distinguish between different models of F_A. We effectively show the three different models (described earlier) for F_A as a function of Q^2 . Model 3 (based on duality) is a factor of 1.4 higher than the dipole approximation. Note that resolution effects are included in understanding the statistical error in this extraction of F_A,

Figure 7 shows the extraction of F_A from Miller, Baker, and Kitagaki, using their plots of $d\sigma/dq^2$. For $Q^2 > 2$ (GeV/c)^2 there is essentially no measurement of F_A. Even the measurements of $F_A(Q^2)$ below 2 (GeV/c)^2 have significant errors, hence one cannot assume F_A is a dipole for low Q^2. The maximum Q^2 values that can be achieved with incident neutrino energies of 0.5, 1.0, 1.5 and 2 GeV are 0.5, 1.2, 2.1 and 3.0 (GeV/c)^2, respectively. Since K2K, MiniBooNE, and T2K energies are in the 0.7–1.0 GeV range, these experiments probe the low $Q^2 < 1$ (GeV/c)^2 region where nuclear effects are large (see Figures 8). The low-Q^2 ($Q^2 < 1$ (GeV/c)^2) MiniBooNE and K2K experiments have begun to investigate the various nuclear effects in carbon and oxygen. However, higher Q^2 data are only accessible in experiments like MINERνA, which can span the 2–8 GeV neutrino energy range. MINERνA's measurement of the axial form-factor at high Q^2 will be essential to a complete understanding of the vector and axial structure of the neutron and proton.

2.2.10 Fermi gas model

There are three important nuclear effects in quasi-elastic scattering from bound targets: Fermi motion, Pauli blocking, and corrections to the nucleon form-factors due to distortion of the nucleon's size and its pion cloud in the nucleus. Figure 8 shows the nuclear suppression versus E_ν from a NUANCE[36] calculation[21] using the Smith and Moniz[37] Fermi gas model for carbon. This nuclear model includes Pauli blocking and Fermi motion but not final state interactions. The Fermi gas model uses a nuclear binding energy $\epsilon = 25$ MeV and Fermi momentum $k_f = 220$ MeV/c. Reference [37] shows how the effective k_f and nuclear potential binding energy ϵ (within a Fermi-gas model) for various nuclei is determined from electron scattering data.

2.2.11 Bound nucleon form-factors

The predicted distortions of nucleon form-factors due to nuclear binding are can be as large as 10% at $Q^2 = 1$ (GeV/c)^2 to 15% at $Q^2 = 2$ (GeV/c)^2. With carbon, iron and lead targets, MINERνA can compare measured form-factors for a range of light to heavy nuclei. Figure 6 shows the cross-section suppression due to bound form-factors. As is described in [22], these effects can cause variations up to 10% in the differential cross-sections at MiniBooNE, K2K and T2K energies.

Requiring vector and axial contributions to W_1 be equal for $Q^2 > 0.5$ (GeV/c)^2 introduces further suppression at low Q^2. Changing the various assumptions in $d\sigma/dq^2$ as calculated with dipole form-factors introduces 5–10% effects on the Q^2 distributions these experiments will see.

2.2.12 Intra-nuclear rescattering

In neutrino experiments, detection of the recoil nucleon helps distinguish quasi-elastic scattering from inelastic reactions. Knowledge of the probability for outgoing protons to reinteract with the target remnant is therefore highly desirable. The NEUGEN Monte Carlo used by MINERνA uses the INTRANUKE procedure to estimate this intra-nuclear re-scattering as described earlier in this section. Similarly, quasi-elastic scattering with nucleons in the high-momentum tail of the nuclear spectral function needs to be understood. More sophisticated treatments than the simple Fermi gas model are required. Conversely, inelastic reactions may be misidentified as quasi-elastic if a final-state pion is absorbed in the nucleus. With its constrained kinematics, low-energy neutrino-oscillation experiments use the quasi-elastic channel to measure the (oscillated) neutrino energy spectrum at the far detector; uncertainty in estimation of non-quasi-elastic background due to proton intra-nuclear rescattering is currently an important source of systematic error in K2K.

The best way to study these effects is to analyze electron scattering on nuclear targets (including the hadronic final states) and test the effects of the experimental cuts on the final-state nucleons. MINERνA can address proton intra-nuclear rescattering by comparing nuclear binding effects in neutrino scattering on carbon to electron data in similar kinematic regions. Indeed, MINERνA members will be working with the CLAS collaboration to study hadronic final states in electron scattering on nuclear targets using existing JLab Hall B data. This analysis will allow theoretical models used in both electron and neutrino experiments to be tested. Other work in progress, with the Ghent[38] nuclear physics group, will develop the theoretical tools needed to extract the axial form-factor of the nucleon using MINERνA quasi-elastic data on carbon. The ultimate aim is to preform nearly identical analyses on both neutrino and electron scattering data in the same range of Q^2.

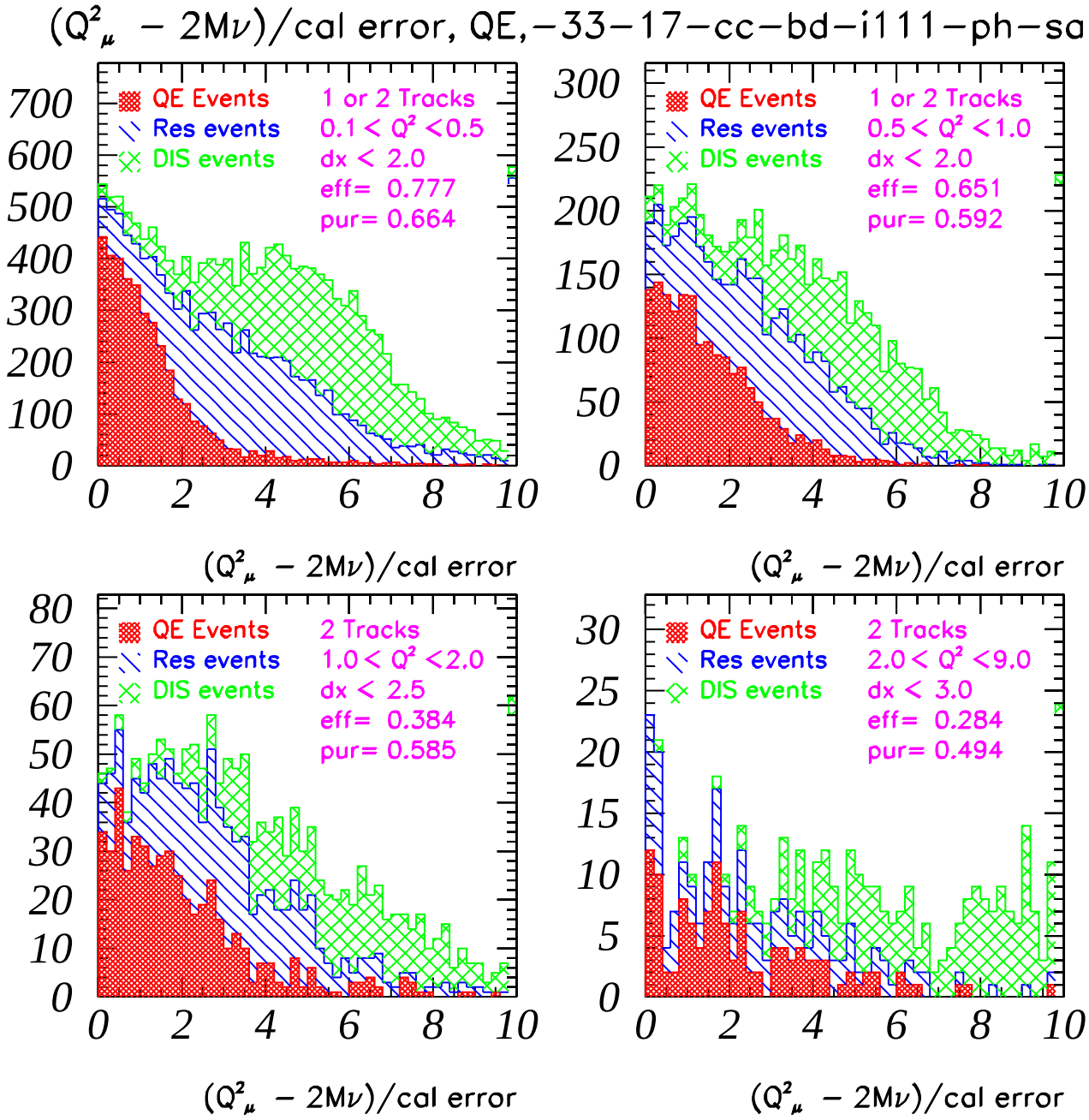

Figure 4: Significance of the difference between Q^2 from the quasi-elastic hypothesis and Q^2 from the final state energy, for quasielastic candidates. "cal error" on the plot is the expected error for $Q^2_\mu - 2M\nu$ from smearing of the kinematic quantities. The efficiency and purity are stated on the plots when the Q^2 difference is less than the amount given by dx. The purity and efficiency for $Q^2 < 1\ GeV$ require 1 or 2 found tracks. The purity and efficiency for $Q^2 > 1 GeV$ require 2 found tracks.

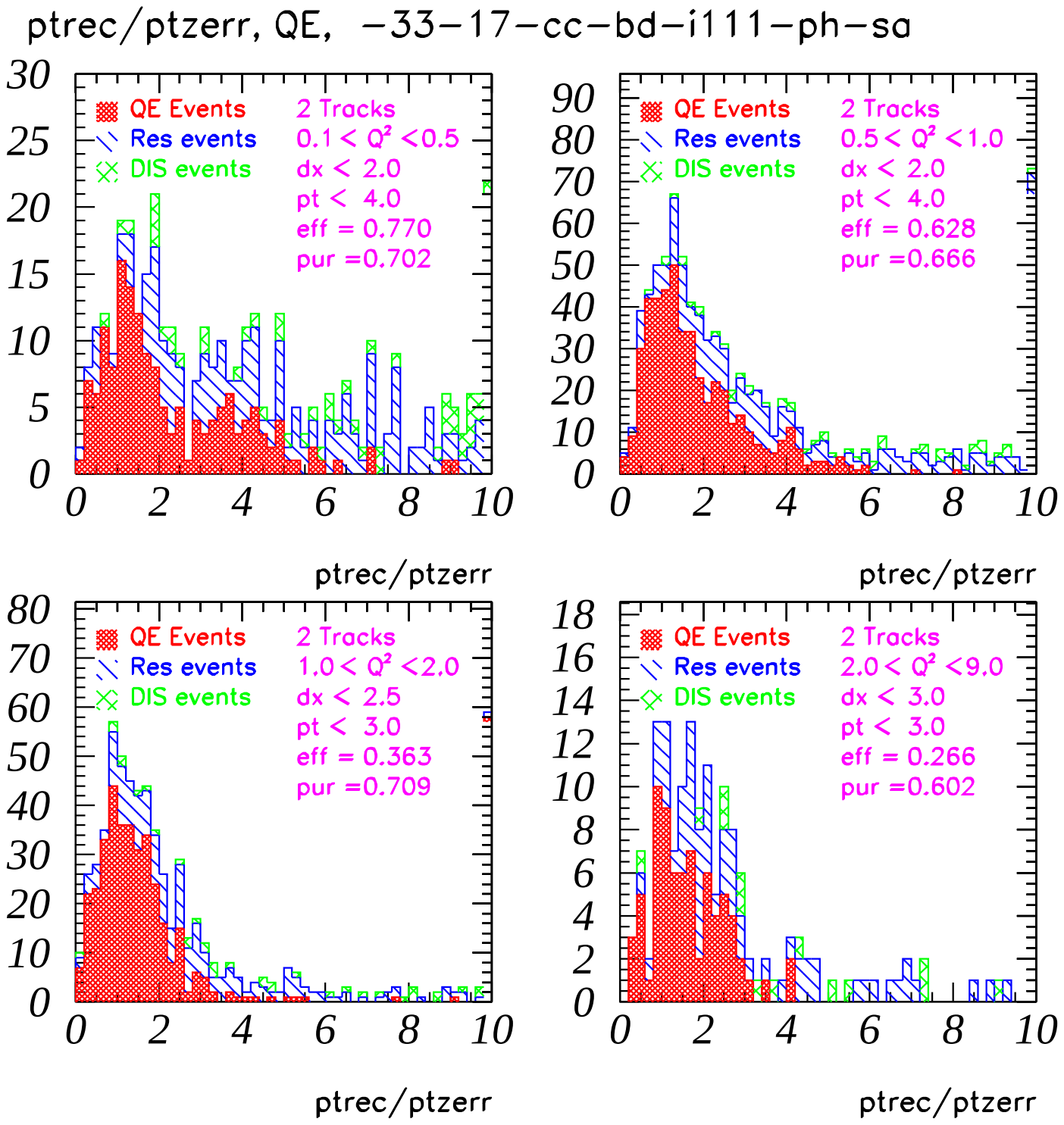

Figure 5: Significance of the difference between p_T from the quasi-elastic hypothesis for 2 track events. "ptzerr" is the expected error in p_T from smearing of the kinematic quantities. The efficiency and purity are stated on the plots when the Q^2 difference is less than the amount given by dx. and p_T is less than the amount given in the plot. The purity and efficiency for $Q^2 < 1\ GeV$ require 1 or 2 found tracks. The purity and efficiency for $Q^2 > 1\ GeV$ require 2 found tracks.

The pt

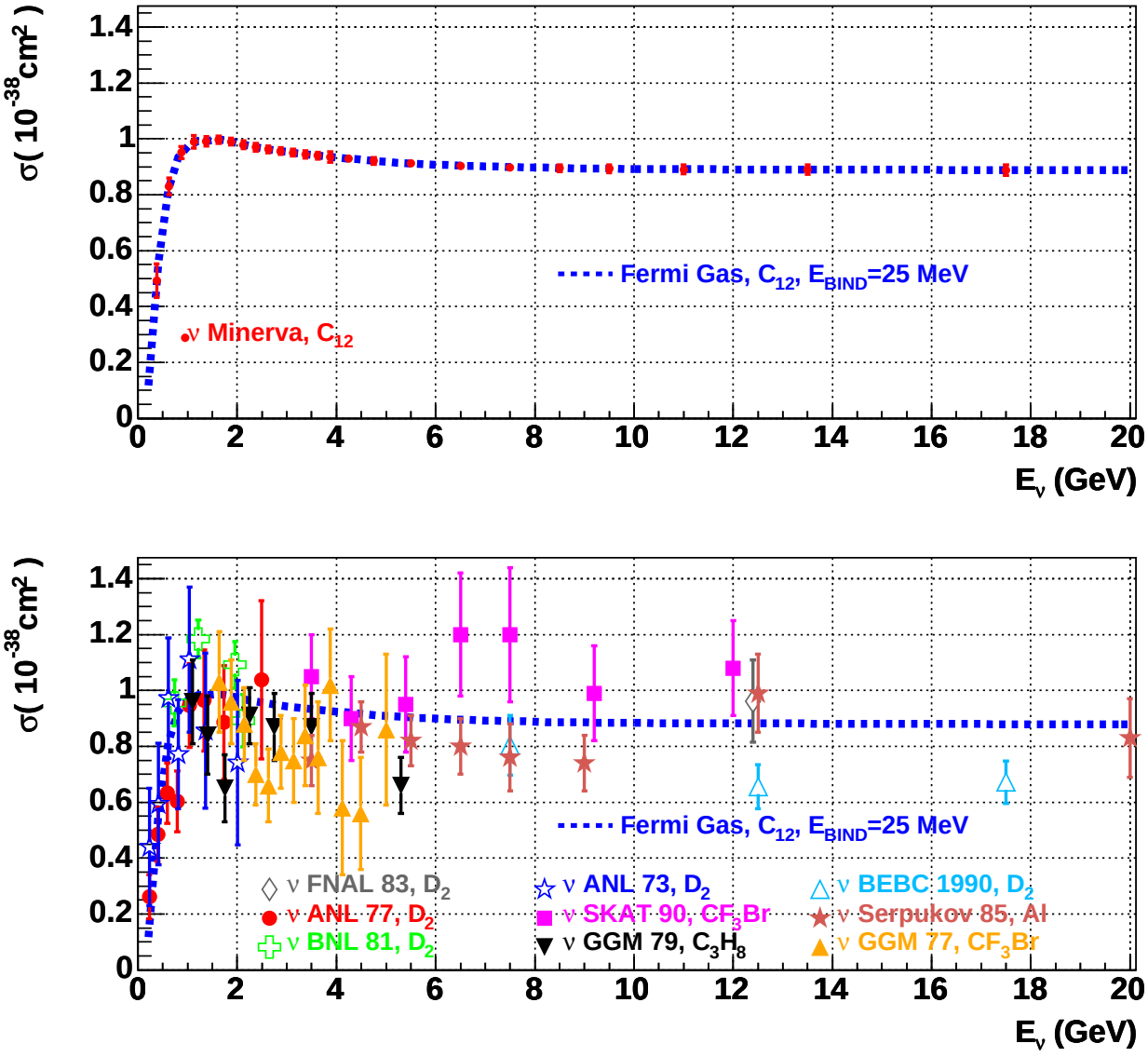

Figure 6: The quasi-elastic neutrino cross-section along with data from various experiments. Representative calculations are shown using BBBA-2006 form-factors with $M_A = 1.014$ GeV/c^2. The dashed curve [21] uses a Fermi gas model for carbon with 25 MeV binding energy and 220 MeV/c Fermi momentum. The predicted MINERνA points, with errors, are shown. The data shown in the bottom plot are from FNAL 1983 [23], ANL 1977 [25], BNL 1981 [26], ANL 1973 [27], SKAT 1990 [28], GGM 1979 [29], BEBC 1990 [30], Serpukov 1985 [31], and GGM 1977 [32]. The data have large errors and are only marginally consistent throughout the E_ν range.

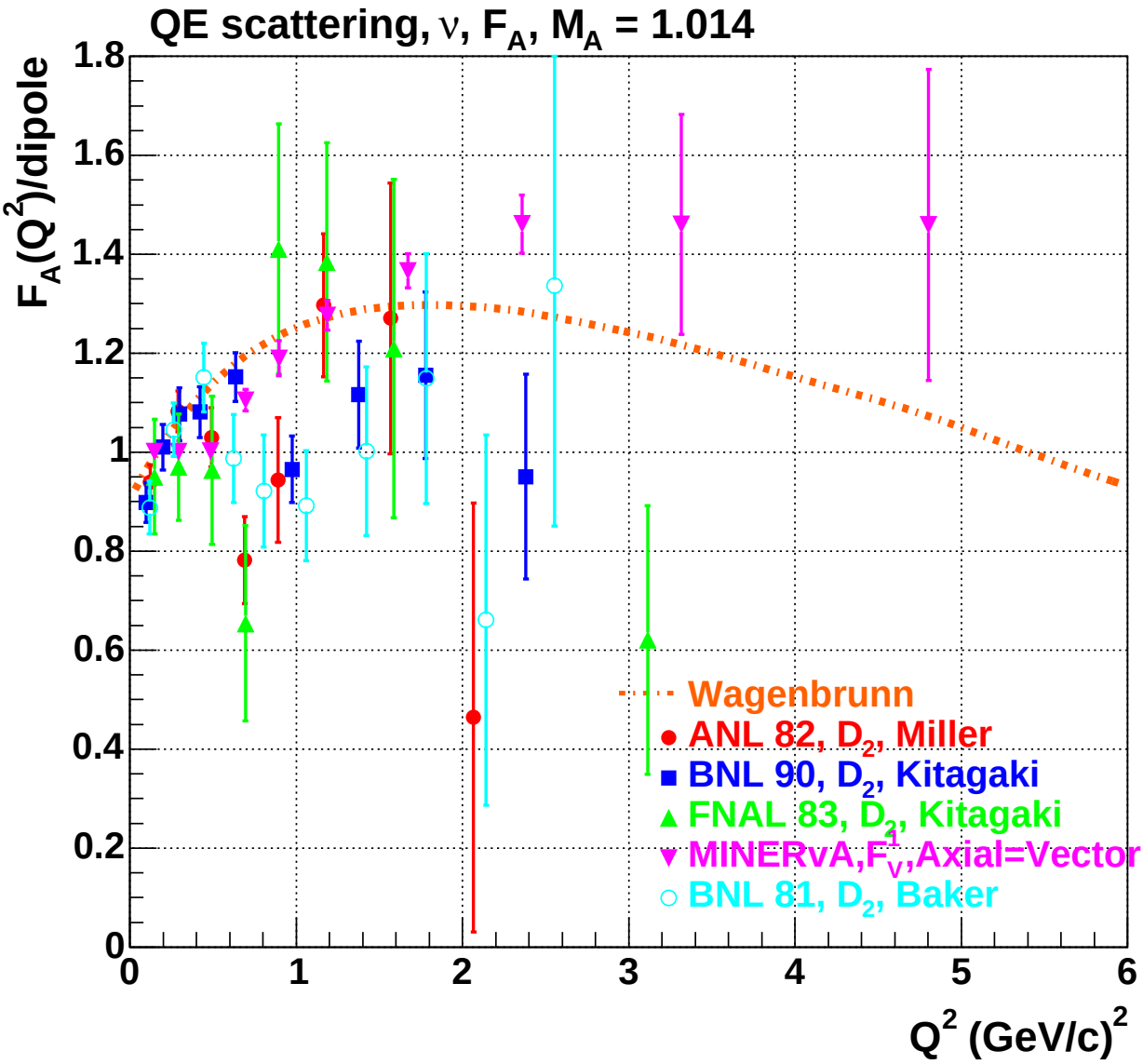

Figure 7: Estimation F_A/dipole for a four year MINERνA run using the quasielastic analysis described in the text. The MINERνA points are plotted assume the Model 3 axial form-factor. Also shown is F_A extracted from deuterium bubble chamber experiments using the $d\sigma/dq^2$ from the papers of FNAL 1983 [23], BNL 1990 [48], BNL 1981 [26], and ANL 1982 [33]. Also shown is the expectations from Model 2 for the axial form-factor.

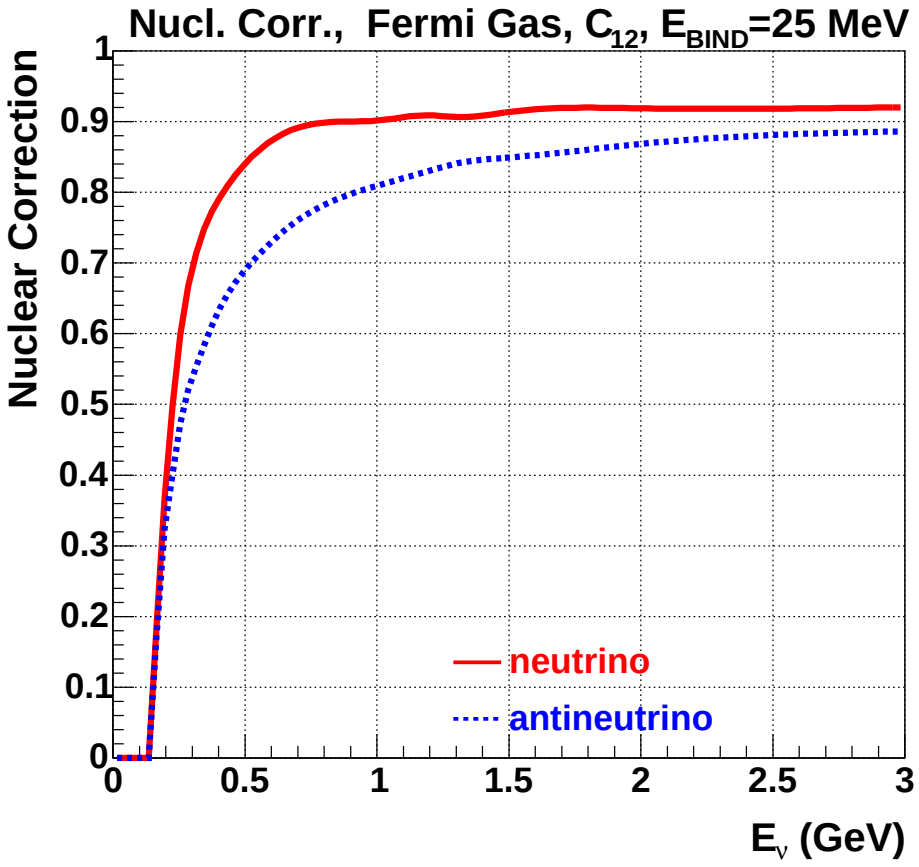

Figure 8: Pauli suppression in a Fermi gas model for carbon with binding energy $\epsilon = 25$ MeV and Fermi momentum $k_f = 220$ MeV/c. A similar suppression is expected for quasi-elastic reactions in MINERνA.

2.3 Resonant Pion Production

2.3.1 Introduction

The production and decay of nucleon resonances in neutrino interactions is a significant part of the total neutrino cross section in the few GeV region. These resonances have been explored using electron scattering experiments, but different form factors contribute in the neutrino case, and simulations rely on an early theoretical model by Rein and Sehgal [39]. Because the structure of the model is not as simple as either quasi-elastic or deep inelastic scattering, and because existing neutrino data does not provide significant constraint, there are large uncertainties on the contribution to the total cross section value and its shape.

Resonance production is the least certain part of the neutrino cross section picture, yet it may be the most important. Current and recent neutrino programs (K2K, MiniBooNE and MINOS) and upcoming experiments such as NOνA and T2K expect these interactions to be a large portion of the cross section in the energy region in which they are most interested. The use of similar near and far detectors serves to partially cancel detector systematic errors. However, since there are different incoming neutrino spectra at the near and far detectors and these mostly unknown resonance cross sections are energy dependent, the neutrino cross section errors do **not** cancel and there is a vital need for the systematic and detailed studies MINERνA can provide.

High statistics muon neutrino disappearance experiments are particularly sensitive to the hadronic final state, in particular the number, charge, and kinematics of the final state pions. The lack of knowledge of these final states contributes to an uncertainty in the total hadronic energy, and therefore to the estimate of the incident neutrino energy and the parameter Δm^2. For electron neutrino appearance experiments, constraints on the cross sections of neutral current and charged current single π^o production are needed. In the expected signal region, the former could enter as background from higher energy resonance and DIS interactions, while the latter would primarily be high $E_{\rm had}$ resonance events. In both cases, some kinematic combinations of the resulting decay photons could be indistinguishable from charged current electron neutrino interactions.

For MINERνA the combination of cross section, nuclear effects, and proton and pion final state interaction measurements will require the tracking and calorimetric abilities of a fully active, fine-grained detector.

2.3.2 Cross Section Models and Existing Data

Scattering of electrons and neutrinos off nucleons with hadronic invariant mass $W < 2$ GeV is dominated by resonance excitation. A complete description of the resonance region would require a map of all resonances and the non-resonant processes that contribute. About two dozen resonances are known and each has form factors. Even with much larger statistical accuracy, interpretations of electron scattering data have not reached this laudable goal. The lowest energy states are most easily separated; the most prominent resonance is the $P_{33}(1232)$ (often called the Delta), and most calculations also include the $S_{11}(1535)$, $P_{11}(1440)$, and $D_{13}(1520)$.

Using the Rein and Sehgal formalism, some simulation authors [40] include up to 18 resonances in neutrino simulations. In electro-production, the Delta is most important at low W and the the magnetic dipole term in the cross section dominates. This form factor has a particularly rapid Q^2

falloff (more steep than the nucleon dipole form factor) and emphasizes the C_3^V vector form factor. For neutrino induced resonances, the contribution of C_5^A (due to the axial form factors) is important and these two may be sufficient for a qualitative picture. The axial form factor is determined by the PCAC condition, and is also steeper than the dipole shape. The Delta has received a lot of attention in the medium energy community. Current wisdom is that the mesonic cloud surrounding the quark core dominates the low Q^2 response. That model has been extended to neutrino-nucleon excitation of $P_{33}(1232)$ by Sato, Uno, and Lee [41, 46]. Another model has been developed by Paschos, Sakuda, and Yu [42, 43] and applied to nuclei. Other work on form factors has been done by Lalakulich, Paschos, and collaborators [44, 45], but not yet applied to nuclei. Examples of both models are shown in Fig. 9 compared with data from the Brookhaven deuterium bubble-chamber experiment [47, 48]. In the plot on the left, the authors show the axial and vector contributions to the total cross section; the latter is well constrained by electron scattering experiments. These models describe existing data through most of the region shown, though that data has large uncertainties and does not provide much constraint. There are also large inconsistencies at very low $Q^2 < 0.2$ (GeV/c)^2. The lack of agreement at very low Q^2 has been seen in various interactions and has important consequences for the estimation of the coherent π^o background [49] for ν_e appearance experiments.

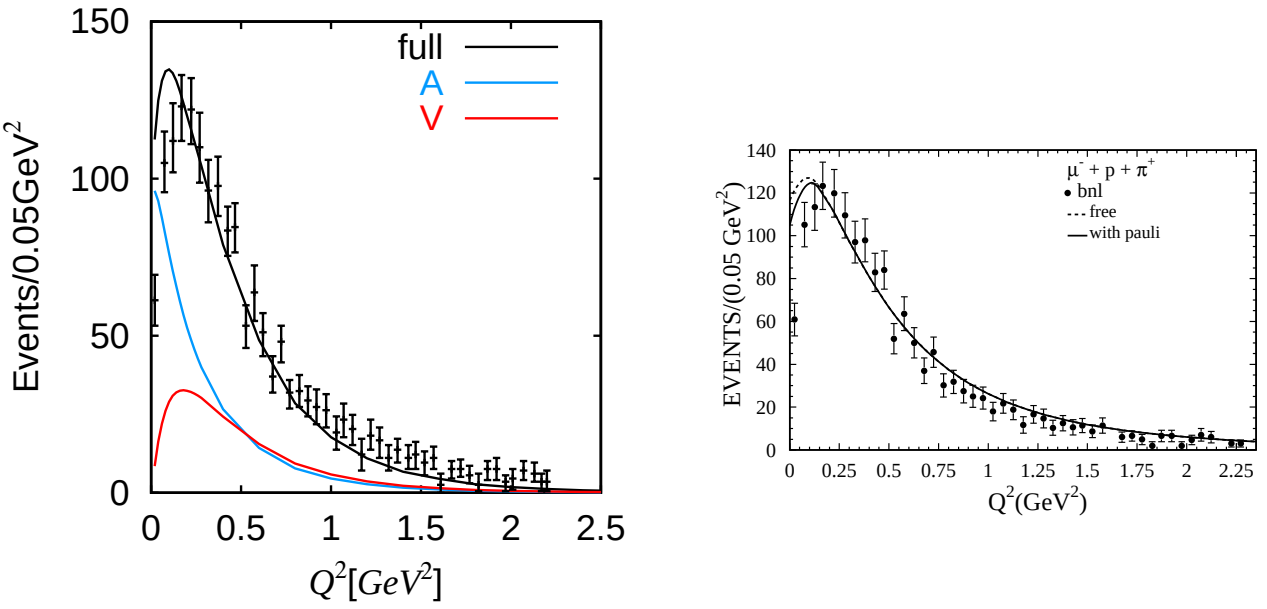

Figure 9: The cross-section $d\sigma/dQ^2$ from BNL compared with the work of Sato, et al. [46] on the left and shows their calculation and breaks down the Axial and Vector contributions to the cross section. A comparison to the same BNL data by Paschos, et al. [43] in the right plot. The full lines are for $M_A = 1.05$ GeV/c^2, the dashed line has no explicit Pauli blocking included.

The Q^2 dependence is determined by these form factors as well as nuclear effects, and in turn determines the outgoing angular distribution of the lepton as well as the hadronic final state particles.

One concern, for both resonance and quasi-elastic scattering off nuclei, are nuclear effects (especially Pauli blocking) which certainly play a large role at very low Q^2; this corresponds to more forward going final state leptons, a kinematic region which is difficult to access in electron beam experiments. This uncertain region accounts for a significant fraction of the total cross section. MINERνA with its variety of nuclear targets, can start to disentangle nuclear effects from form factors.

The poor understanding of the resonance cross section also impacts quasi-elastic cross section measurements. Experiments with relatively high thresholds for recoil nucleons and pions, such as Cerenkov detectors or coarse grained tracking detectors will frequently see only the outgoing lepton, and will tag it as a QE candidate. Any measurements of these interactions, or measurements which depend on the kinematic simplicity of a purified QE sample, will benefit from the improved measurement of the resonant background.

There are concerns, even when the outgoing pion can be seen, such as the π^o decay to two photons, or charged pions which are above detection threshold. The kinematics of these pions are often modified as they pass through the nucleus, sometimes even being completely absorbed. There will be a reduction of approximately 30% of pions with the same charge as the exchange current (π^+ for neutrino CC interactions) produced in a light target such as C or O. This is due to a combination of charge exchange (to π^o or π^-, for example) or absorption. These final state nuclear effects will change the visible energy, requiring corrections to estimate the true neutrino energy, the quasi-elastic cross section, or where π^o backgrounds are important such as ν_e searches. Again, MINERνA's integral nuclear targets and low tracking thresholds are designed to isolate exclusive single pion production and to disentangle these nuclear effects.

2.3.3 MINERνA performance

MINERνA will be able to improve the above situation with precision measurements of the total resonance cross sections, of the $d\sigma/dQ^2$ and $d\sigma/dW$ differential cross sections, and measure exclusive final states on a variety of nuclei to constrain the form factors and final state interaction models. One major goal is to provide a characterization of the final states and the energy dependence of the cross sections for the many contributing processes (pion production and nucleon knockout). With a fully active detector, MINERνA will be able to measure almost all final states. The angular distributions can be determined in most cases. The second goal is to study the details in special cases when individual resonances can be isolated. Building on experiences with electron scattering experiments, we will be able to isolate $P_{33}(1232)$ and $S_{11}(1535)$ by taking advantage of their decay processes.

Unlike inclusive charged lepton scattering (e,e'), measurements of neutrino inclusive scattering with wide-band neutrino beams can not rely solely on the outgoing lepton kinematics, since the incident neutrino's exact energy is not *a priori* known. Reconstruction of inclusive resonance production requires the measurement of W; for the dominant Delta resonance this will be at 1232 MeV. For charged current interactions this is accomplished by measuring the lepton energy and angle (which is easy for muons) and also either the hadronic energy or its angle. Measuring these also gives estimates for Q^2 and E_ν.

The hadronic energy can be estimated by tracking and identifying every particle emerging from an interaction vertex, or by summing up the dE/dx energy deposited by all the reaction products other than the muon. Both methods will be important for the study of resonances. Because the primary

vertex multiplicities for resonance production will usually be low, a single pion and recoil nucleon, tracking (momentum from range) will be a viable technique for low efficiency, high resolution samples. However, the pions have a significant probability to interact or decay before stopping, and MINERνA's calorimetric abilities will be required to get inclusive cross sections. The correlation between the reconstructed and true E_h is shown in Fig. 10.

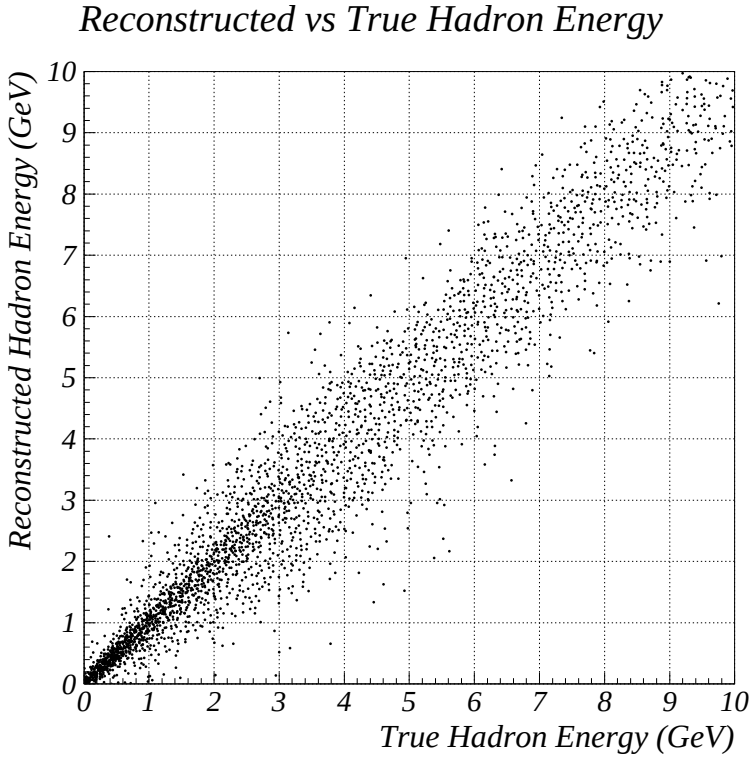

Figure 10: Correlation between true and reconstructed hadron energy.

When the kinematics of resonance events are reconstructed using E_h and an assumed muon momentum resolution $\delta P/P$ of 9%, we obtain the correlation of the reconstructed and true W and Q^2 shown in Fig 11. The W resolution is around 100 MeV in the region of the $\Delta(1232)$, and the Q^2 resolution is slightly better than 0.2 (GeV/c)^2. Even with this smearing, the Δ peak is still visible in the W spectrum in both Fig. 11 and also in the histogram in Fig. 12. Note, the smearing is largely due to detector effects, but there is a smaller, but still significant smearing due to nucleon Fermi motion for interactions taking place in carbon.

With the resolution on W described above, we will be able to make a simple selection to isolate a resonance enhanced sample. Isolating a sample with one muon and two visible hadrons, then choosing values of $1.1 < W < 1.5$ GeV yields a sample with enhanced $\Delta^{++}_{(1232)}$. With this selection, we estimate a 70% purity and 20% efficiency. There is a model dependence to the purity estimate coming from the DIS-Resonance transition region which will have to be settled by the data. In this case, we can reconstruct Q^2 assuming that a Δ was produced, which yields excellent resolution of

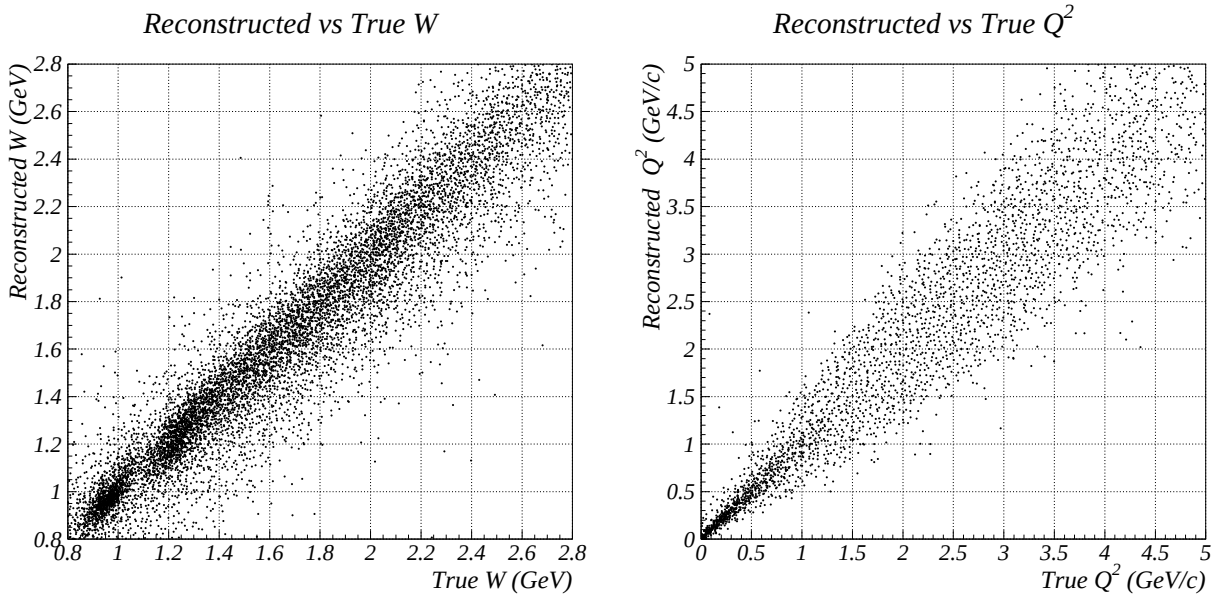

Figure 11: Correlation between true and reconstructed W (left) and Q^2 (right).

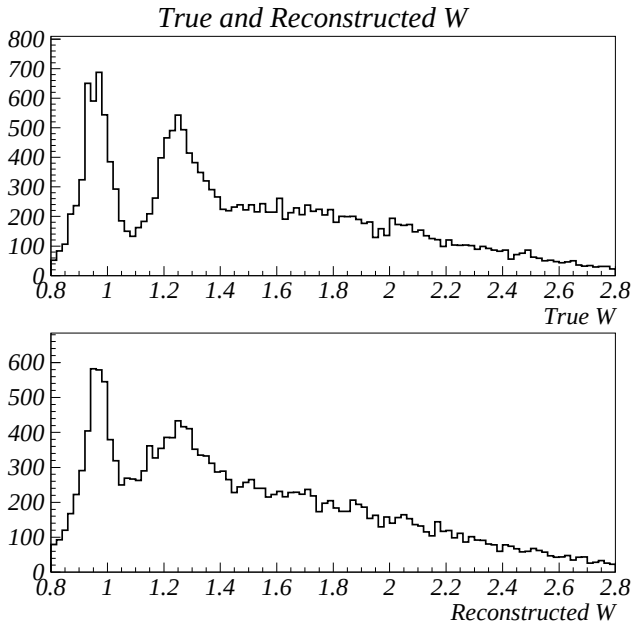

Figure 12: Top: true W distribution for resonant events with $Q^2 < 1$ (GeV/c)^2. Bottom: reconstructed W distribution for the same Q^2 range.

0.05 (GeV/c)^2 for the Δ signal. A sample of the resulting resonstructed Q^2 distribution, with no further selections is shown in Fig. 13. A substantial fraction of that efficiency (and access to lower

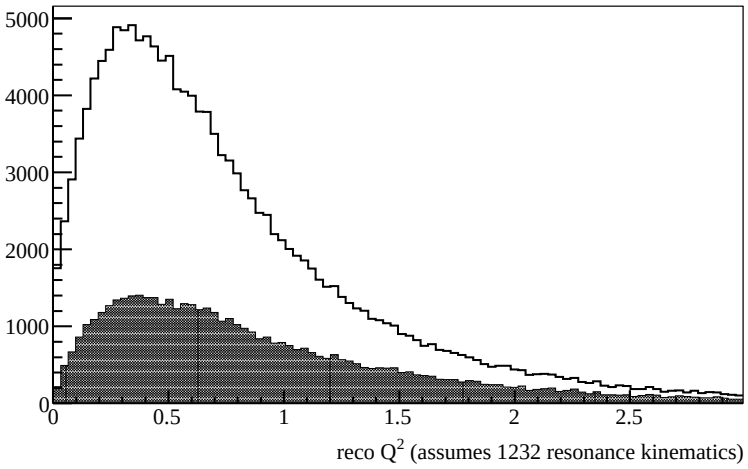

Figure 13: Estimate of the reconstructed Q^2 distribution for the two visible hadron enhanced Δ^{++} selection. The shaded region shows the expected background after this selection. This also shows the statistics for the estimated sample for three years running in the medium energy beam.

Q^2 events) can be regained by lowering the tracking thresholds and/or including events with only one reconstructed hadron track. For the estimate above, the tracking requirement was high: three XUXV layers. The purity may be improved by selecting events with little extra vertex activity.

2.3.4 Identifying specific final states

Previous neutrino studies have focused on charged particles because they are easier to track. However, the best physics interest in the resonance region might come from neutral particles such as π^0, η, and ω. That is because there is a preponderance of strongly excited baryon resonances close to their thresholds. The strong coupling of $\pi^0 p$ to the $\Delta(1232)$ resonance is well-known and the strong ηp coupling to S_{11}(1535) is now also very well established. There is also a resonance at the ωN threshold, P_{13}(1720), but its properties are not well-determined. Isolation of either of the higher mass states would be a major accomplishment. Then, it becomes possible for ν beams to add to the knowledge of these states.

Each of these mesons must be detected through decays. The π^0 decays almost solely to $\gamma\gamma$; that is also the largest decay branch for η. The signature would be clean: two photons of half the meson mass at large opening angle. The next largest decays for η are 3 pions, with charged ($\pi^+\pi^-\pi^0$) and neutral modes ($3\pi^0$) both prominent, but the latter will be difficult to reconstruct in MINERνA. The primary decay of ω is also to $\pi^+\pi^-\pi^0$. This mode should also be seen in the MINERνA detector because low energy particles will be contained very well. In each case, the invariant mass of a proton+meson pair could be constrained to be near the mass of the appropriate resonance as an additional way to suppress background. Studies of these modes are just beginning.

2.3.5 Error budget

The significant errors to some of the above analyses have been estimated; what is important depends on the measurement. For absolute cross section measurements, we expect a 5% absolute error for most parts of the energy spectrum when the MIPP hadron production results are incorporated into the NuMI beam flux. It is important to maintain access to the monitoring data and systematic studies that constrain errors due to beamline fluctuations, targeting, and alignment.

At this level, uncertainties in background subtraction and efficiency modeling will be comparable. This is certainly an improvement over the previous bubble chamber results where $> 20\%$ errors are reported (for a recent discussion see [50]). For relative cross sections, the relative flux error between neighboring energy bins will be 2%, and those measurements will be dominated by background, resolution, and calibration errors.

For the analysis of the shape of Q^2 or other distributions, such as in Fig. 9, the largest error will likely be from bias in the energy reconstruction. For example, a 2% uncorrectable bias in the muon momentum translates to an uncertainty in the shape of the Q^2 distribution that is about half as large as the apparent discrepancy in those plots, when you consider MINERνA's statistical error will be negligible for those distributions.

The extraction of pure nuclear effects from comparisons between the MINERνA nuclear targets, including the very low Q^2 region and the rescattering and absorption of final state pions, will probably be statistics limited. Because the detector surrounding the nuclear targets are the same, systematic uncertainties in the selection and backgrounds for the relative measurements will partially cancel. Thus, the limiting factor will be the maximum practical size for these targets.

2.3.6 Conclusion

MINERνA will significantly improve current measurements of resonance production of pions in neutrino interactions due to the large event samples, variety of nuclear targets, low detection thresholds, and excellent tracking and calorimetry. These measurements will be able to constrain the total cross section, relative cross sections, and the shape of the Q^2 distributions, and allow the first direct comparisons of neutrino interactions on different nuclei. These physics goals are consistent with the expected systematic and statistical errors. Better data on these processes will be of vital importance to current and future oscillation experiments as well as nucleon decay experiments. They will also lead to better understanding of the axial form factors of the nucleon and the effects of the nuclear medium.

2.4 Coherent Pion Production

MINERνA's high rates, range of nuclear targets, fine granularity, strong pattern recognition capabilities, and good electromagnetic calorimetry will make it possible to study charged- and neutral-current coherent neutrino-nucleus scattering with unprecedented precision. In this section we will briefly review the capabilities of the detector in this area focusing on the requirements placed on the detector design.

2.4.1 Introduction

Coherent neutrino-nucleus reactions, in which the neutrino scatters coherently from an entire nucleus with small energy transfer, leave a relatively clean experimental signature and have been studied in both charged-current ($\nu_\mu + A \rightarrow \mu^- + \pi^+$) and neutral-current ($\nu_\mu + A \rightarrow \nu + \pi^0$) interactions of neutrinos and anti-neutrinos. Although the coherent interaction rates are typically an order of magnitude or more lower than other single-pion production mechanisms, the distinct kinematic characteristics of these events allow them to be cleanly identified. Because the outgoing pion generally follows the incoming neutrino direction, this reaction is an important background to searches for $\nu_\mu \rightarrow \nu_e$ oscillation, as these events can easily mimic the oscillation signature of a single energetic electron shower.

A unique strength of the experiment is the ability to study both neutral and charged current channels from a variety of nuclear materials ranging from carbon to lead in the same experiment. Kinematic predictions from models can be explored in the charged current sample where the kinematics are fully reconstructed. The comparison of angular and energy distributions for produced pions in neutral and charged-current events will provide useful constraints on the various models, several of which predict CC/NC ratios differing by around 20% [51, 52]. A systematic comparison of charged- and neutral-current coherent production is currently a topic of considerable interest. While data on single π^0 production from the K2K and miniBoone experiments are in reasonable agreement with predictions [53, 54], a search for coherent CC production in the K2K experiment found only 7.6 ± 50.4 events where 470 were expected. This large difference between NC and CC production has been the subject of considerable theoretical work [55, 56, 57, 58] and could also account for the depletion at low Q^2 of inelastic events as compared with Monte Carlo predictions [59, 60].

2.4.2 Charged-current cross-section

The kinematics of coherent scattering are quite distinct compared to the more common deep-inelastic and resonant interactions. Because the coherence condition requires that the nucleus remain intact, low-energy transfers to the nuclear system, $|t|$, are needed. Events are generally defined as coherent by making cuts on the number of prongs emerging from the event vertex followed by an examination of the t distribution, where t is approximated by:

$$-|t| = -(q - p_\pi)^2 = (\Sigma_i (E_i - p_i^{||}))^2 - (\Sigma_i (p_i^{\perp}))^2 \quad (1)$$

With its excellent tracking capabilities, MINERνA's inner detector can measure this kinematic variable well.

To quantify MINERνA's ability to measure the charged-current coherent cross-section, a Monte Carlo study was carried out using the GEANT detector simulation described in Chapter 6. Analysis cuts were tuned on a sample of coherent interactions corresponding to a four-year run with the three-ton fiducial volume. Events were generated according to the appropriate mix of low and medium energy beams. This study used the Rein-Seghal [51] model of coherent production, as implemented in NEUGEN3. A low-energy beam sample containing all reaction channels was used for background determination. Based on published bubble chamber analyses, charged-current reactions should be the largest background contributor, in particular quasi-elastic and Δ-production reactions where the baryon is mis-identified as a pion or not observed. To isolate a sample of coherent interactions, a series of cuts are placed on event topology and kinematics. The detector response is parametrized based on measurement smearing of 0.5^o angular resolution for reconstruction of muon and pion tracks, $18\%/\sqrt{E_{had}}$ hadronic energy resolution, and 10% muon energy resolution.

Topological cuts An initial set of topological cuts are applied to isolate a sample of events which contain only a muon and charged pion. These cuts are based on the hit-level and truth information as provided by the GEANT simulation.

1. **2 Charged Tracks:** The event is required to have 2 visible charged tracks emerging from the event vertex. A track is assumed to be visible if it produces at least 8 hit strips in the fully active region of the detector which are due to this track alone.

2. **Track Identification:** The two tracks must be identified as a muon and pion. The muon track is taken to be the most energetic track in the event which does not undergo hadronic interactions. The pion track is identified by the presence of a hadronic interaction. The pion track is required not to have ionization characteristic of a stopping proton (which is assumed can be identified 95% of the time).

3. **π^0/neutron Energy:** Because MINERνA is nearly hermetic we also assume that neutral particles will produce visible activity which can be associated with the event and used to exclude it. Events with more than 500 MeV of neutral energy (π^0 or neutron) produced in the initial neutrino interaction are rejected.

4. **Track Separation:** To make good measurements of the two tracks, the interaction point of the pion must be more than 30 cm from the primary vertex, and at this interaction point, at least 4 must strips separate the two tracks in at least one view.

Kinematic cuts Because coherent and background processes have very different kinematics, cuts on kinematic variables are effective in isolating the final sample. Kinematic quantities are estimated from the smeared measurements of muon energy, pion energy, and muon angle measurement under the assumption that the event in question is CC-coherent. Kinematic cuts are as follows:

1. **$x_{Bj} < 0.2$:** Requiring Bjorken-x (as reconstructed from the observed pion and muon 4-momenta) less than 0.2 eliminates much of the background from quasi-elastic reactions with $x_{Bj} \sim 1$.

2. $t < 0.2$ **(GeV/c)^2:** The most powerful variable for the identification of coherent events is the square of the 4-momentum transfer to the nucleus. Equation 1 relating t to the observed particles in the event is used as the estimator of this quantity.

3. $p_\pi > 600$ **MeV:** Requiring $p_\pi > 0.6$ GeV effectively eliminates background from Δ excitation, which tends to produce lower energy pions.

Signal and background distributions for several of the important cut variables are shown in Figure 15. The relative normalizations of the two distributions in the initial plot is arbitrary; subsequent plots show the effect of the applied cuts.

Applying this set of cuts to our signal sample (85k events) we find that 25.5k signal events pass all cuts, which gives an overall efficiency of 30%. The expected purity of the sample is 67$\pm$3%, where the error bar is the statistical error on the Monte Carlo sample used for the study. We note that in this analysis other important variables for background rejection, related to associated activity around the vertex, were not used. Figure 15 shows the expected precision of the MINERνA measurement as a function of neutrino energy. Here we have only included the statistical error on the signal and assumed that the measured value is that predicted by Rein-Seghal. No attempt has been made to quantify the systematic errors on this measurement other than that resulting from the background subtraction. Previous measurements of the coherent cross-section were statistics limited. Of particular interest is the energy dependence of the cross section. Figure 16 compares the predictions of the Rein-Sehgal and Paschos-Kartavtsev models for charged current coherent scattering from carbon. Sizable differences are evident, particularly near threshold.

2.4.3 Detector requirements

Figure 17 shows the efficiency and purity of the CC-coherent selection as a function of the assumptions about the measurement resolution of the detector. This study indicates that to maintain high efficiency and purity for this analysis good hadronic energy resolution ($<$20% / $\sqrt{E_{had}}$) and angular resolution are required. In addition, good particle ID by dE/dx is crucial to distinguish protons which interact from pions.

2.4.4 Error Budget

The charged current cross section will be measured in bins of energy. In this section we perform a rough error analysis based on the assumption that the data will be divided into 20 energy bins with equal statistics. In each bin there will be around 1900 events of which 1275 are signal and 628 background. The statistical uncertainty on the cross section will therefore be 3.4%. We factorize the systematic errors into beam and analysis/detector related quantities. For the beam we find that the uncertainty in absolute cross section due to the flux uncertainty is 5%. The error on the background subtraction is 2.0% and is dominated by the statistical error on the subtraction. The error due to the uncertainty in the muon and pion energy scales, 2% and 3% respectively, is 1%. This value was determined by shifting the reconstructed energies by the stated amounts and determining the change in number of events accepted. The systematic uncertainty on the efficiency correction is hard to estimate without access to a variety of models as the correction is large and will be model

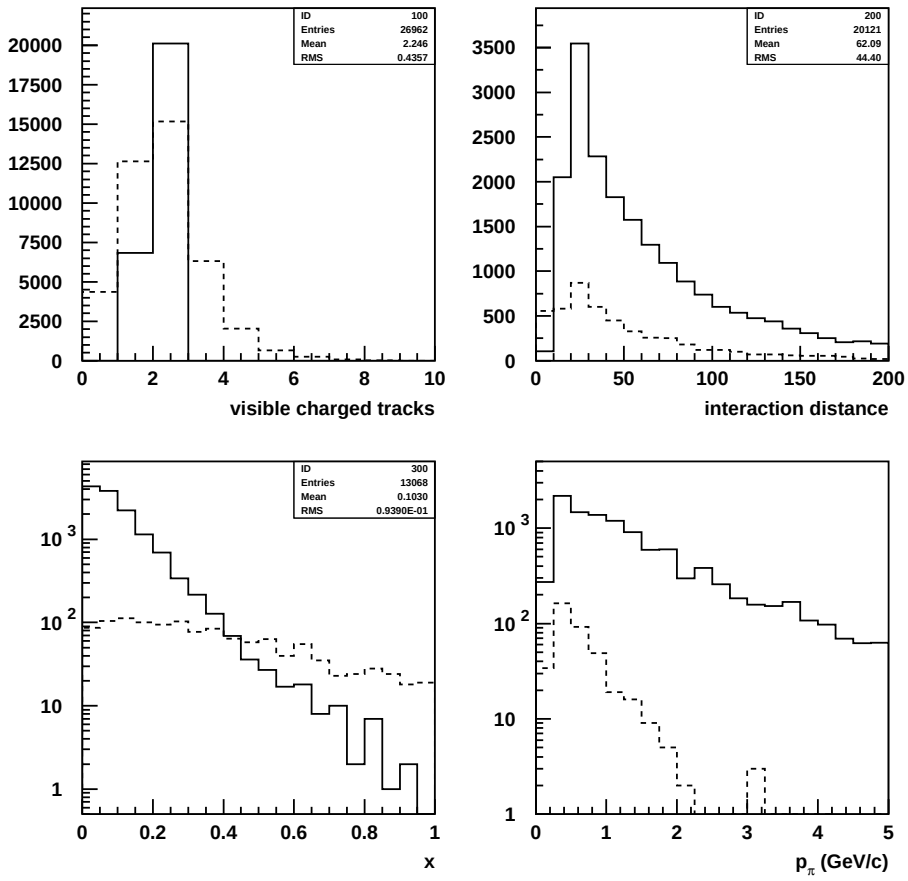

Figure 14: Topological and kinematic quantities for signal (solid) and background (dashed) processes. Top Left: Visible charged tracks. Top Right: Distance between the event vertex and the location of the pion interaction (in cm). Bottom Left: Bjorken-x. Bottom Right: Charged pion momentum.

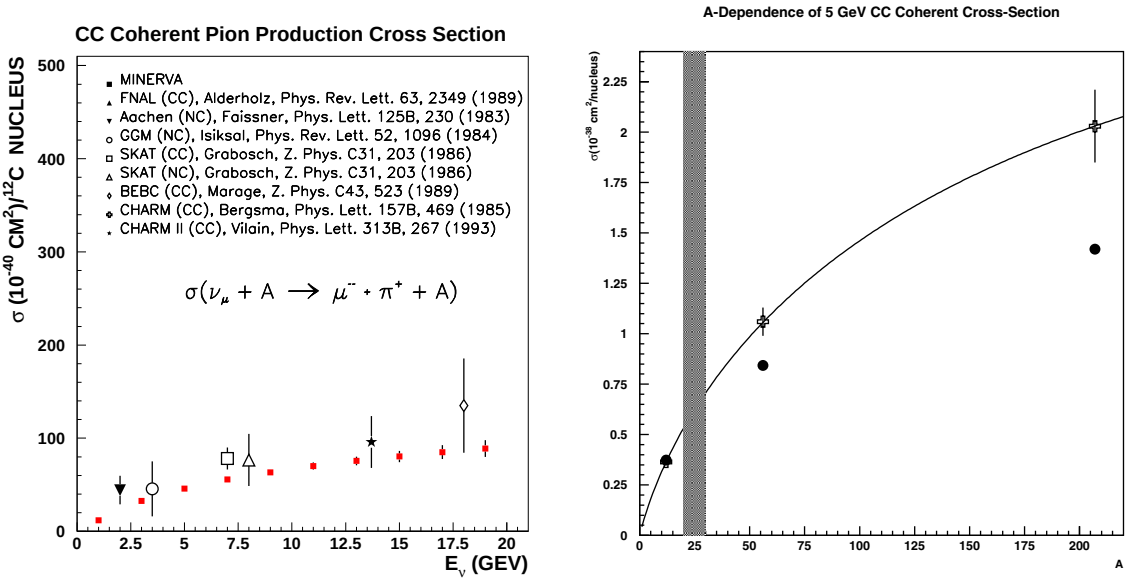

Figure 15: Left: Coherent cross-sections measured by MINERνA compared with existing published results. MINERνA errors here are statistical only. Right: Measurement of the coherent cross-section as a function of atomic number in MINERνAṪhe shaded band indicates the range of previous measurements. Error bars indicate the size of the experimental errors in a single 1-GeV bin. The curve shows the prediction from the Rein-Seghal model. Crosses are the prediction of the Rein-Seghal model for scattering from carbon, iron, and lead, circles are the predictions of the Paschos-Kartavtsev model.

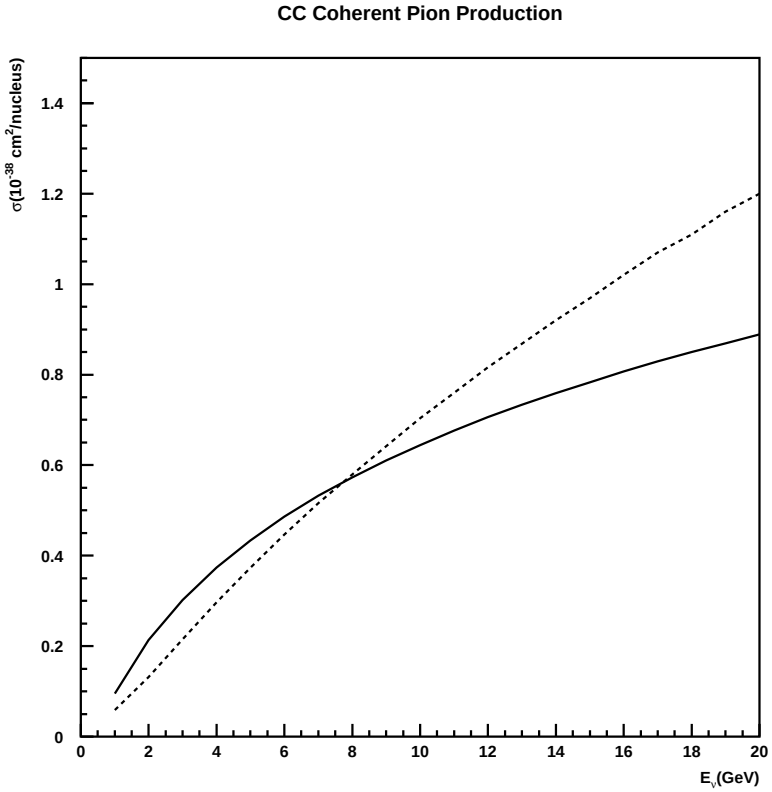

Figure 16: Predictions for charged current coherent production from carbon from the Rein-Sehgal model (solid) and the Paschos-Kartavtsev model (dashed).

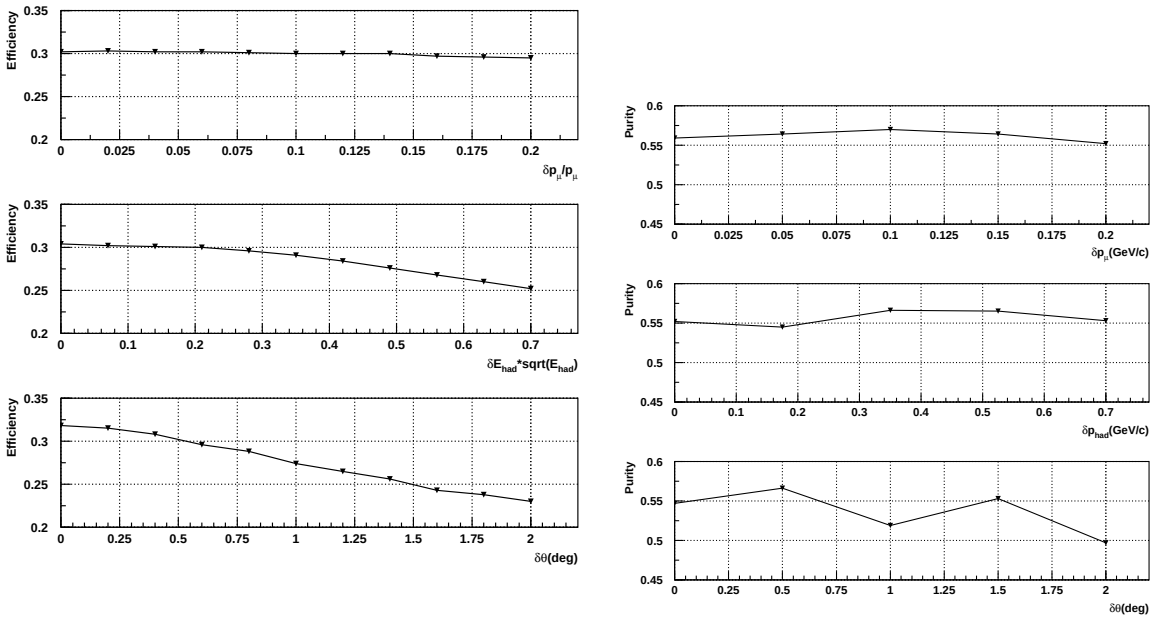

Figure 17: Left: Efficiency of CC coherent selection as a function of angular resolution, muon energy resolution, and hadronic energy resolution. Right: Purity of CC coherent selection as a function of the same variables. Note that in the hadronic energy resolution plots the x-axis is the coefficient of the $1/\sqrt{E_{had}}$ term.

dependent. We estimate this uncertainty to be 5% and will be data-driven to some extent since our sample will provide full kinematic distributions with which existing and future models must agree. Understanding the efficiency of the topological cuts will require good testbeam calibration over a range of charged pion and proton energies. In summary, the statistical error will be 3.4%, the systematic uncertainty (beam-related) is 5%, and the systematic uncertainty (analysis/detector-related) is 5.5%.

2.4.5 A-dependence of the coherent cross-section

Another task for MINERνA will be comparison of reaction rates for lead and carbon. The expected yield from the lead target (0.85 t) of MINERνA will be $\approx$ 2000 charged-current events in the analysis sample for a four-year run, assuming the same efficiency. The A-dependence of the cross-section depends mainly on the model assumed for the hadron–nucleus interaction, and serves as a crucial test for that component of the predictions. No experiment to date has been able to perform this comparison. For reference, the predicted ratio of carbon to lead neutral-current cross-sections at 10 GeV in the Rein-Sehgal and Paschos models are 0.223 and 0.259, respectively [56]. Figure 15 shows the predicted A-dependence according to the model of Rein and Sehgal.

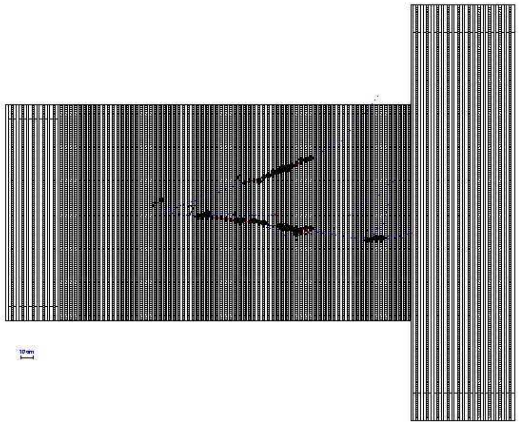

Figure 18: A simulated neutral-current coherent π^0 production event in MINERνA. The position of the π^0 decay vertex can be determined accurately by extrapolating the two photons backward. Notice that both photons pass through a number of planes before beginning to shower, distinguishing them from electrons.

2.4.6 Neutral-current cross-section

Neutral-current π^0 production can occur through a number of mechanisms - resonant production, coherent production, and deep-inelastic scattering. Figure 18 shows a striking example of MINERνA's response to coherent π^0 production.

By requiring two well-separated electromagnetic clusters that shower in the scintillator target, and extend at least 6 scintillator planes, about 30% of the coherent π^0 events produced in the detector are retained. Furthermore, by requiring the ratio of the energy in the two clusters to that of the total event energy to be above 90%, and requiring any extra energy to be less than 100 MeV, reduces both the ν_e (ν_μ) charged-current contamination to a few (less than one) events. Figure 19 shows these two last variables, where the coherent π^0 peak is clearly visible in the plot on the right. The resulting sample in this simple analysis (1000 events per year in 3 tons of fiducial mass) is roughly half resonant π^0 production and half coherent π^0 events, which can be separated by studying the angular and energy distribution of the events, as well as the presence or absence of additional particles at the production vertex identified by the two photon showers.

Neutral pions from resonance excitation are neither as energetic nor as collinear as those produced coherently. Resonant π^0 are particularly susceptible to final-state nuclear interaction and rescattering, which will be studied in detail by MINERνA using charged-current reactions.

As a proof-of-concept, a sample of neutral-current single-π^0 events has been selected using simple cuts. For events with two well-separated electromagnetic clusters ($E_\pi \equiv E_1 + E_2$), each passing through at least six planes of the fully-active region, requiring $E_\pi/E_{tot} > 90\%$ and $E_{tot} - E_\pi < 100$ MeV efficiently isolates a neutral-current π^0 sample, as shown in Figure 20. After these cuts, the contamination of ν_e and ν_μ charged-current interactions (combined) is less than 1%.

Coherent and resonant interactions can be cleanly separated by cutting on the π^0 angle to the beam direction, as shown in Figure 21, which also highlights MINERνA's excellent π^0 angular resolution. The overall efficiency for selecting coherent neutral-current π^0 is about 40%. With this efficiency we expect around 17k NC coherent events in the analysis sample from the four-year run.

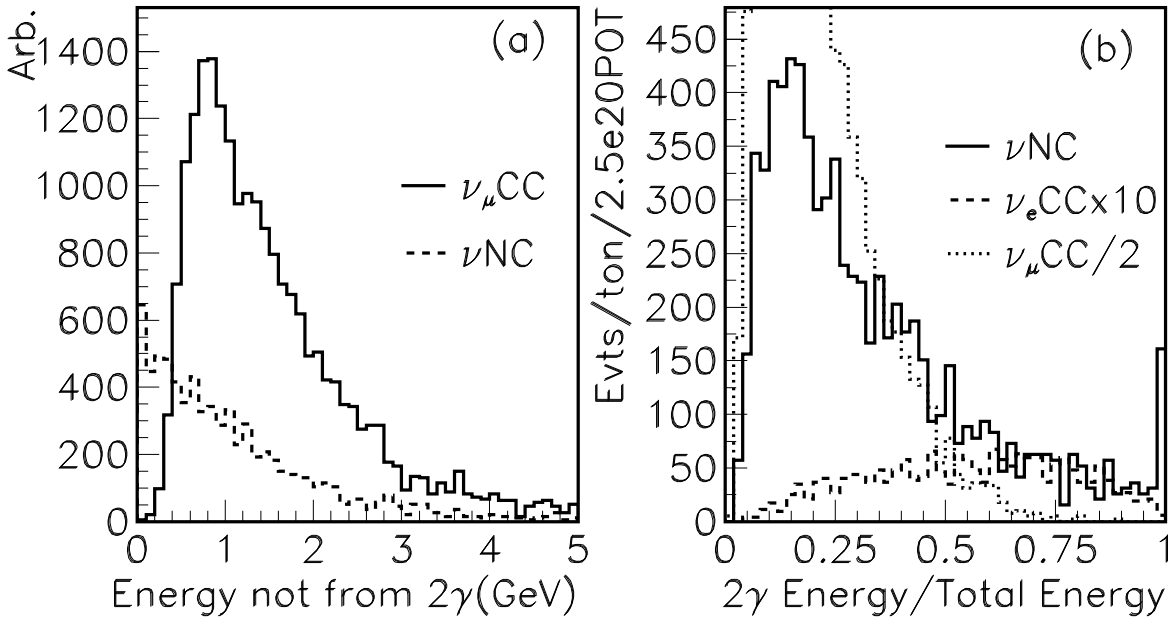

Figure 19: Variables that reject backgrounds to coherent π^0 measurements: (a) Other energy in the event for ν_μ charged- and neutral-current events, and (b) Ratio of two photon energy to total event energy for ν_μ charged-current sample (reduced by factor of 2), ν_e charged-current (increased by a factor of 10) and the neutral-current sample (normalized per ton per year, acceptance calculated for 3 tons fiducial volume)

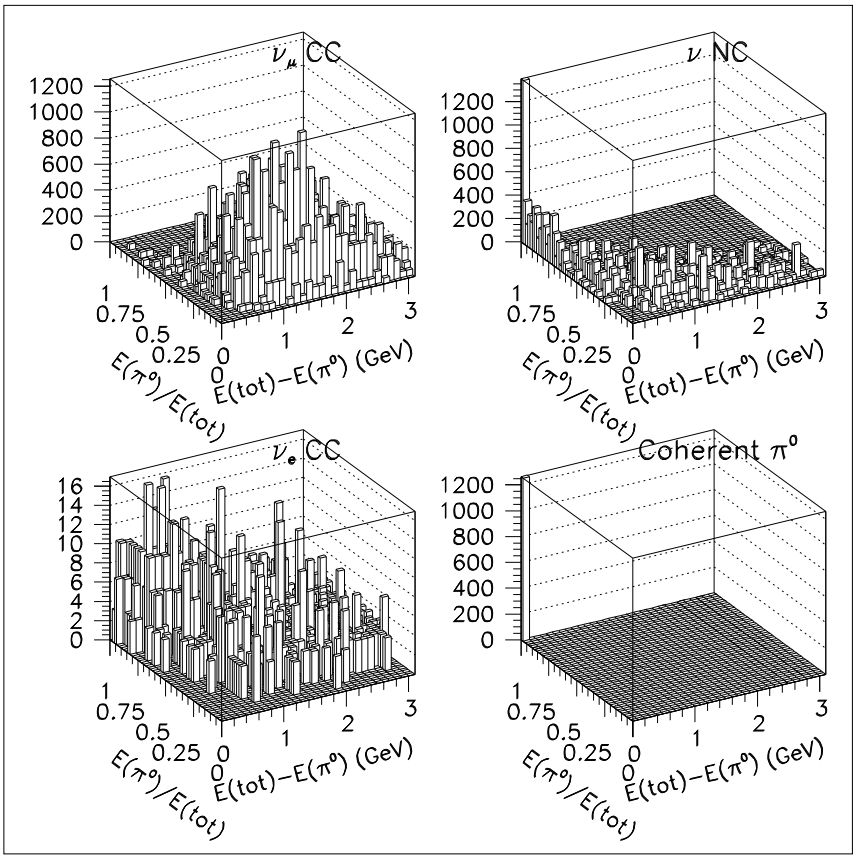

Figure 20: Selection of neutral-current single-π^0 production. The variables plotted are the fraction of visible energy carried by the π^0 candidate (E_π/E_{tot}) and the residual energy $E_{tot} - E_\pi$. The left-hand plots show backgrounds from ν_μ(top) and ν_e(bottom). The plot at top right shows the same distribution for true neutral-current π^0 production, and the lower right shows the subset from coherent scattering. In the neutral-current plots, notice the dramatic concentration of the coherent π^0 signal in a single bin, in the left-most corner of the graph. All samples shown are normalized to a 3 ton-yr exposure of MINERνA.

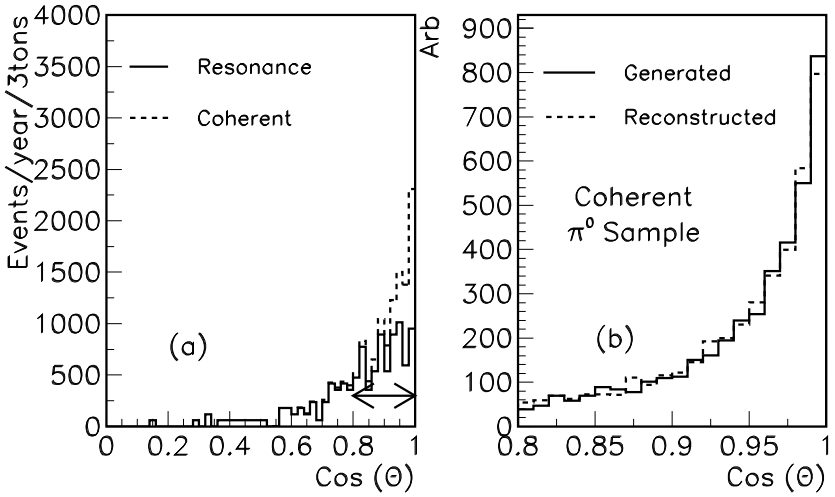

Figure 21: Angular distribution of neutral-current single-π^0 sample. The plot at left shows all events passing the cuts on E_π/E_{tot} and $E_{tot} - E_\pi$ described in the text, broken down into coherent and resonant reactions. The coherent sample is strongly forward-peaked. The plot at right is a close-up of the forward region comparing the true and reconstructed π^0 angular distributions from the beam direction. The distributions are nearly identical, highlighting the MINERνA's excellent angular resolution.

2.5 Strange and Charm Particle Production

High-statistics studies of exclusive strange-particle production by neutrinos will be possible for the first time in MINERνA. Sample sizes for several channels accessible to MINERνA in a four-year ν_μ run are summarized in Table 2.5.3. Cross section measurements afforded by these samples will impact other areas of particle physics, for example in estimation of atmospheric neutrino ΔS backgrounds to nucleon-decay searches. MINERνA's physics program will also include searches for new processes, *e.g.* strangeness-changing neutral-current reactions and unusual baryon resonances. Extended running of the NuMI beam with $\bar{\nu}$ exposures will provide valuable data for many neutrino topics. Anti-neutrino exposure will facilitate study of $\Delta S = 1$ single-hyperon production (Λ, Σ, Y^*), and would permit a novel measurement of CKM matrix elements. Selected topics and their motivations are summarized below.

2.5.1 Backgrounds to Nucleon Decay

Current lifetime limits for nucleon decay ($\tau/\beta \geq 10^{33}$ years) have not diminished hopes for the eventual success of supersymmetric grand unification (SUSY GUTs). Indeed, there is strong motivation to proceed with more ambitious experimental searches. For the near future, improved searches will be carried out by Super–Kamiokande. Eventually these will be taken up by a next generation of underground detectors. Continued progress, either by improving limits to 10^{34} year lifetimes or discovering nucleon decay, hinges upon improved knowledge of certain neutrino interactions which, when initiated by atmospheric neutrinos, can imitate nucleon-decay signals. The most problematic of background reactions to SUSY GUT modes arise with neutral-current associated production of strangeness at threshold energies.

2.5.2 Measurement of $\sigma(\nu\Lambda K^+)$

/minerva/ will measure the exclusive $\Delta S = 0$ neutral-current channel

$$\frac{d\sigma}{dE_\nu}(\nu_\mu p \to \nu_\mu K^+ \Lambda), \tag{2}$$

from its threshold at ≈ 1 GeV through its rise and plateau at E_ν between 10-15 GeV. For purposes of comparison and as a valuable check on systematics[61], we will simultaneously measure the the $\Delta S = 0$ companion charged-current reaction

$$\frac{d\sigma}{dE_\nu}(\nu_\mu n \to \mu^- K^+ \Lambda). \tag{3}$$

2.5.3 Strangeness-changing Neutral Currents

Strangeness-changing neutral-current reactions have never been observed. Their occurrence at rates accessible in NuMI would imply new physics beyond the Standard Model. Existing limits on NC $\Delta S = 1$ processes are based upon searches for rare K decays. Although there are experimental difficulties with unambiguous identification of such processes in neutrino reactions, there is nevertheless

Reaction Type	Exclusive Channel	No. Events (≥ 0 constraint)
$\Delta S = 0$ CC	$\nu_\mu n \rightarrow \mu^- K^+ \Lambda^0$	23,100
	$\nu_\mu n \rightarrow \mu^- \pi^0 K^+ \Lambda^0$	20,400
	$\nu_\mu n \rightarrow \mu^- \pi^+ K^0 \Lambda^0$	13,800
	$\nu_\mu n \rightarrow \mu^- K^- K^+ p$	11,200
	$\nu_\mu p \rightarrow \mu^- K^0 K^+ \pi^0 p$	3,300
$\Delta S = 1$ CC	$\nu_\mu p \rightarrow \mu^- K^+ p$	34,900
	$\nu_\mu n \rightarrow \mu^- K^0 p$	5,200
	$\nu_\mu n \rightarrow \mu^- \pi^+ K^0$	4,600
$\Delta S = 0$ NC	$\nu_\mu p \rightarrow \nu K^+ \Lambda^0$	7,900
	$\nu_\mu n \rightarrow \nu K^0 \Lambda^0$	2,400
	$\nu_\mu n \rightarrow \nu K^0 \Lambda^0$	6,100

Table 2: Event samples for kinematically constrainable exclusive strangeness production reactions, in a four-year exposure of MINERνA's three-ton inner fiducial volume.

an opportunity for a search in the neutrino sector. A search for strangeness-changing neutral-current neutrino interactions can usefully clarify the extent to which new physics parameters may be missing from the analysis of weak radiative hyperon decays. It is plausible that neutrino reactions, in contrast to hyperon weak decays, may provide cleaner signals for a new weak current, since multi-loop quark-gluon diagrams which complicate hyperon decay analysis would be absent.

2.5.4 Hyperon Beta-decay and Exotic Quark States

Hyperon beta-decay $A \rightarrow B\ e^-\ \bar{\nu}_e$ provides a window onto weak hadronic current form-factors and their underlying structure. Recent high-statistics measurements of these form-factors using KTeV Ξ^0 hyperon beta-decays have been reported[62]; the results show that the level of SU(3) breaking is very small compared to expectations of modern theories[63]. These new results have been used to extract the CKM matrix elements V_{us}[64] [65]. Similar studies are possible using anti-neutrino interactions that produce hyperons. The hyperon decays have the added feature of a self-analyzing power of the polarization vector. In hyperon production via anti-neutrinos,the fundamental form-factors and CKM matrix elements will be accessible without the hindrance (encountered in hyperon beta-decay) of double solutions due to the missing neutrino energy.

Searches for $\Delta S = 1$ production of pentaquark states such as those reported[66], could be greatly extended in MINERνA. In neutrino-nucleus interactions wherein hyperons and mesons are produced together, a wealth of combinations can be examined to search for the full spectrum of the pentaquark family[67] of particles and for other exotic quark combinations such as di-baryons as well.

2.5.5 Charm Production

Charm production in MINERνA is suppressed by the relatively low energy of its beams, hence the reach will be limited. Nevertheless, the cross-section turn-on just above threshold is very sensitive to

the bare charm quark mass and MINERνA can still make a valuable contribution. With the proposed beam running schedule for MINERνA we expect $\sim 23,000$ of inclusive charm production events in the fiducial volume in the standard four year run.

2.6 The Perturbative and Non-Perturbative Interface

2.6.1 Quark Distributions at Large x

One of the most fundamental properties of the nucleon is the structure of its valence quark distributions. Valence quarks are the irreducible kernel of each hadron, responsible for its charge, baryon number and other macroscopic properties. Sea quarks, which at high Q^2 are largely generated through gluon bremsstrahlung and subsequent splitting into quark-antiquark pairs, represent one source of the nonperturbative dressing of the valence quarks at low Q^2. At higher x values these quark / anti-quark contributions drop away, and the physics of the valence quarks is cleanly exposed. Although a large body of structure function data exists over a wide range of x and Q^2, the region $x > 0.6$ is not well explored.

Knowledge of the valence quark distributions of the nucleon at large x is vital for several reasons. Measurements of structure functions at large x will bring insights into the mechanisms responsible for spin-flavor symmetry breaking. In addition, quark distributions at large x are a crucial input for estimating backgrounds in searches for new physics beyond the Standard Model at high energy colliders [68].

The uncertainties in the current nucleon parton distribution functions at high x are of two predominant types: the ratio of the light quark pdf's, $d(x)/u(x)$, as $x \to 1$ and the role of leading power corrections (higher twist) in the extraction of the high x behavior of the quarks. The measurement of quark densities at high-x_{Bj} is closely related to the question of the leading power corrections known as "higher twist effects". The n^{th} order higher twist effects are proportional to $1/Q^{2n}$ and reflect the fact that quarks have transverse momentum within the nucleon and that the probe becomes larger as Q^2 decreases, thus increasing the probability of multi-quark participation in an interaction. Different analyses of higher twist corrections in current data leave some unresolved issues that would benefit from new experimental information.

The only actual measurements of a higher-twist term in neutrino experiments have been two low-statistics bubble chamber experiments: in Gargamelle [69] with freon and in BEBC [70] with NeH_2. Both bubble chamber analyses are complicated by nuclear corrections at high-x. However, both analyses found a twist-4 contribution that is smaller in magnitude than the charged leptoproduction analysis and, most significantly, is preferentially negative.

Higher twist components of the structure functions may be obtained from deviations of measured data from the calculable expectations from perturbative QCD. As indicated in Figure 22, showing one of the dominant systematic errors, the expected uncertainties in the structure functions obtained in the MINERνA experiment will be such that this type of higher twist analysis may be performed precisely for the first time with neutrino measurements. In this case, it is crucial also to understand the effects arising from nuclear medium modifications to the nucleon structure functions, which will also be measured by MINERνA.

2.6.2 Quark-Hadron Duality

The description of hadrons in terms of their fundamental quark and gluon constituents is one of the major challenges in nuclear physics today. While at present we cannot describe the structure and interactions of hadrons directly utilizing the quark and gluon degrees of freedom of QCD, we know

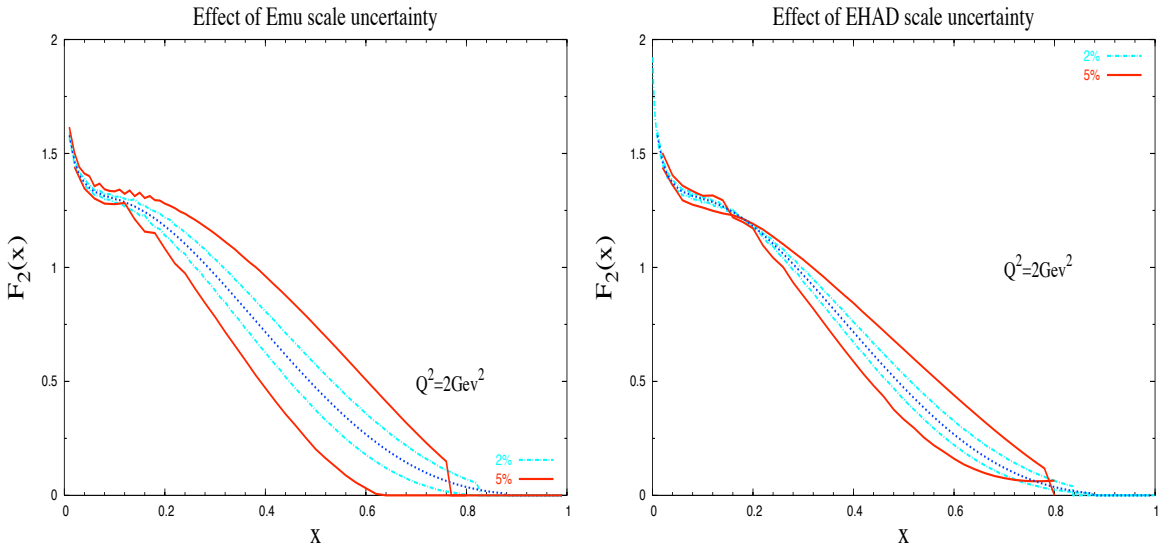

Figure 22: The effect of the (dominant) energy scale uncertainties, muon on left and hadron on right, on the x dependence of the F_2 structure function is shown for the transition region at at $Q^2 = 2$ GeV^2. Here, for instance, x = 0.7 corresponds to $W^2 = 1.7$ GeV^2 in the resonance region.

that in principle it should just be a matter of convenience in choosing to describe a process in terms of quark-gluon or hadronic degrees of freedom. This fact is referred to as *quark-hadron duality*, and means that one can use either set of complete basis states to describe physical phenomena. At high energies, where the interactions between quarks and gluons become weak and quarks can be considered asymptotically free, an efficient description of phenomena is afforded in terms of quarks; at low energies, where the effects of confinement make strongly-coupled QCD highly non-perturbative and the final state is guaranteed to be made of hadrons, it is more efficient to work in terms of collective degrees of freedom, the physical mesons and baryons. The duality between quark and hadron descriptions reflects the relationship between confinement and asymptotic freedom, and is intimately related to the nature of the transition from non-perturbative to perturbative QCD. It has been said that (short of the full solution of QCD) understanding and controlling the accuracy of the quark-hadron duality is one of the most important and challenging problems for QCD practitioners today [71].

Although the duality between quark and hadron descriptions is formally exact in principle, how this reveals itself specifically in different physical processes and under different kinematical conditions is a key to understanding the consequences of QCD for hadronic structure. The phenomenon of duality is in fact quite general in nature and can be studied in a variety of processes, such as $e^+e^- \rightarrow$ hadrons, or semi-leptonic decays of heavy quarks. Duality in lepton–nucleon scattering, historically called Bloom-Gilman duality, links the physics of resonance production to the physics of deep inelastic scaling. Duality is manifested here in the observation that the hadronic (resonance) and quark (scaling) strengths are, on average, equivalent. Moreover, this is true for all Q^2 observed above $Q^2 \approx 1$ GeV^2, and thus a perturbative behavior apparently describes the average Q^2 dependence of

the hadronic, non-perturbative, resonance enhancement region.

The MINERνA experiment is uniquely poised to provide a wealth of data to answer where duality works, in what structure functions, in what reactions, and at what kinematics. Duality has been well-verified [73] for the proton F_2 structure function [74], observed recently in the separated longitudinal and transverse unpolarized structure functions [75], on nucleons and in nuclei [76], and in polarized structure functions [77]. While it's fundamental cause remains a mystery, duality appears experimentally to be a non-trivial property of nucleon structure. It is, therefore, crucial to test it in a variety of reactions – including neutrino-nucleon and nucleus scattering and the structure function xF_3.To accomplish such a study, high precision structure function data are needed in both the deep inelastic and in the resonance regimes. As can be seen in Figure 23, MINERνA will have high statistics in both of these regions.

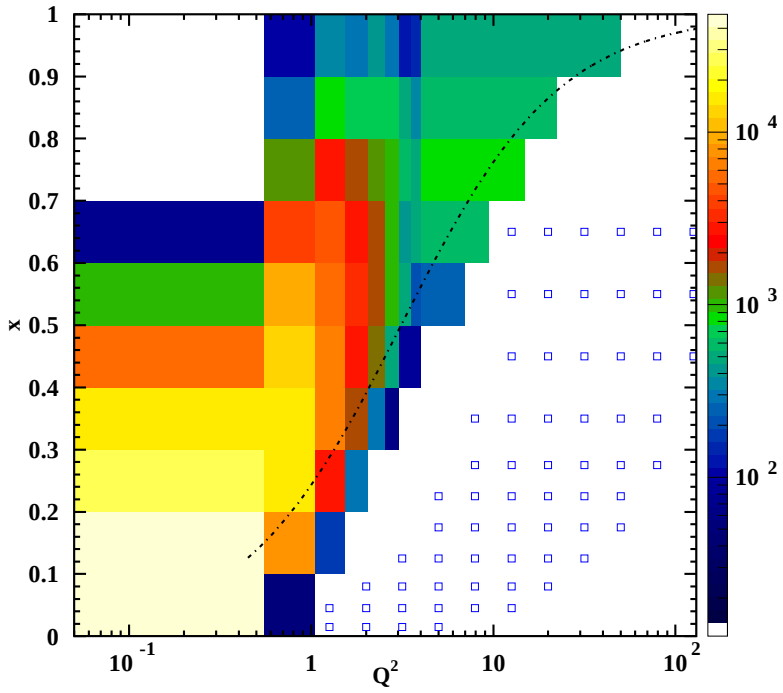

Figure 23: Available xF_3 data (open symbols) and the anticipated (resonance region) MINERνA data (colored distributions in x and Q^2. The curve indicates the commonly-utilized $W^2 = 4$ GeV^2 boundary between the deep inelastic and resonance regimes. The color key to the right indicates anticipated MINERνA statistics.

Duality studies of electron-deuteron scattering at low Q^2 reported a resemblance to deep inelastic neutrino-nucleus scattering at much higher Q^2, indicating a potential sensitivity of duality to the valence quarks [78]. The proposed experiment will allow this observation to be verified and tested for the first time, as data from like kinematic regimes but differing in probe and interaction (from MINERνA and Jefferson Lab) may be compared directly. As shown in Figure 24 in Section 2.6, the kinematic regimes of these facilities are quite complementary.

2.6.3 QCD Moments

Figure 24 from Section 2.6 depicts the substantial kinematic range enhancement in both x and Q^2 made possible by the MINERνA experiment. This broad range of the data will allow for accurate moments of the structure functions to be obtained. To obtain a structure function moment, it is necessary to integrate over the full range in x at a fixed value of Q^2. These moments are fundamental quantities, calculable in QCD and recently calculated in lattice QCD at $Q^2 = 4$ GeV^2 for valence distributions [80]. If duality is shown to hold, the proposed data may provide one of the few available quantities which can be directly compared to lattice QCD calculations – that is, a valence–only structure function moment.

At $Q^2 = 4$ GeV^2, MINERνA will measure the range $0.1 < x < 1$. These data combined with existing world data will allow for moments of structure functions to be obtained with about a 5% precision. It is important to note two things in this case – first, nuclear effects are not expected to play a role in the integrated moments, as it has been shown that the momentum sum rule is preserved in nuclei [81]. Next, uncertainties in kinematics play only a reduced role in moment extractions, which are integrated in x, or in W^2.

Large x (resonance region) data become increasingly important for higher order moments. At n=6, for example, the resonance and large x region above $x = 0.7$ make up 70% of the Cornwall-Norton moment of F_2 at $Q^2 = 10$ (GeV/c)^2. The contribution is larger at $Q^2 = 4$ GeV^2, where lattice calculations are available. As noted above and clear in Figure 23, there currently exist little to no neutrino cross section data in the resonance region or at larger x, while such data will be easily obtainable with MINERνA.

2.7 Deep Inelastic Scattering and QCD

Neutrino scattering plays a crucial role in extraction of fundamental parton distribution functions (PDFs). These PDFs describe parton constituents of protons and other hadrons, and (in the $\overline{MS}$ convention) are precisely defined in terms of operator matrix elements. The necessity of neutrino measurements is obvious, because only neutrinos can resolve the flavor of the nucleon's constituents: ν interacts with d, s, $\overline{u}$ and $\overline{c}$ while the $\overline{\nu}$ interacts with u, c, $\overline{d}$ and $\overline{s}$. The weak current's unique ability to "taste" only particular quark flavors significantly enhances the study of parton distribution functions. MINERνA's high-statistics measurement of the nucleon's partonic structure, using neutrinos, will complement on-going studies with electromagnetic probes at other laboratories.

With the addition of large samples of nub, and dedicated effort to minimizing beam-related systematics, MINERνA will be able to independently isolate all the structure functions $F_1^{\nu N}(x,Q^2)$, $F_1^{\bar{\nu} N}(x,Q^2)$, $F_2^{\nu N}(x,Q^2)$, $F_2^{\bar{\nu} N}(x,Q^2)$, $xF_3^{\nu N}(x,Q^2)$ and $xF_3^{\bar{\nu} N}(x,Q^2)$ for the first time. By taking differences and sums of these structure functions, specific parton distribution functions in a given (x,Q^2) bin can in turn be determined. With the manageable systematic uncertainties expected, this experiment will dramatically improve the isolation of individual PDFs by measuring the full set of ν and $\bar{\nu}$ structure functions.

Extracting this full set of structure functions will rely on the y-variation of the structure function coefficients in the expression for the cross-section. In the helicity representation, for example:

$$\begin{aligned}\frac{d^2\sigma^\nu}{dxdQ^2} &= \frac{G_F^2}{2\pi x}\Big[\frac{1}{2}\left(F_2^\nu(x,Q^2)+xF_3^\nu(x,Q^2)\right)+ \\ &\quad \frac{(1-y)^2}{2}\left(F_2^\nu(x,Q^2)-xF_3^\nu(x,Q^2)\right)- \\ &\quad 2y^2F_L^\nu x,Q^2)\Big]. \end{aligned} \tag{4}$$

By analyzing the data as a function of $(1-y)^2$ in a given (x,Q^2) bin, all six structure functions can be extracted.[3]

MINERνA has the important feature to allow measurement of the neutrino cross section and structure function from a variety of nuclear targets. This will be important both to connect with previous measurements which will overlap the MINERνA result on the high Q^2 end and to allow, for the first time, a precision determination of nuclear effects in neutrino scattering.

2.7.1 Structure Functions

The structure function F_2 has been precisely measured over a large range of Q^2 using charged-lepton probes. Figure 24 illustrates the kinematic coverage for measurements of F_2 using charged-lepton and neutrino probes. Neutrino measurements have been limited so far to moderate Q^2's. MINERνA will provide complimentary information from neutrinos in the high-x low-Q^2 regime which overlaps precise measurements using charged-lepton probes.

[3]Note that for this type of parton distribution function study, anti-neutrino running will be essential.

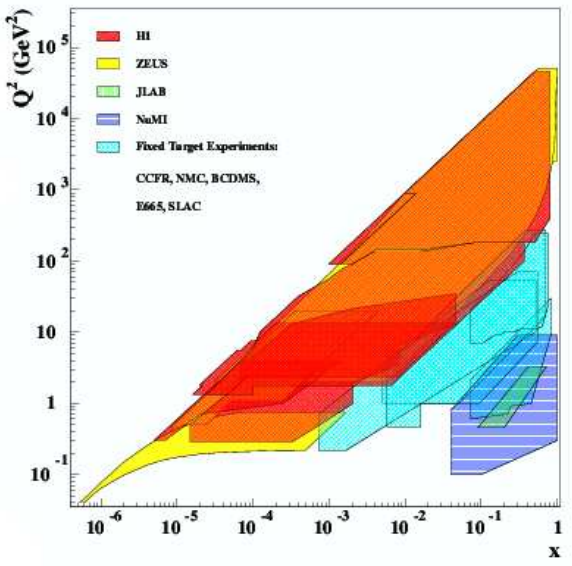

Figure 24: Kinematic coverage of structure function measurements.

While the structure function F_2 is precisely measured with charged-lepton probes, the parity-violating structure function xF_3 can best be determined using a weak-interaction probe. Neutrino measurement have been limited to moderate x and Q^2. As Figure 25 illustrated MINERνA will provide new kinematic coverage for the structure function xF_3.

2.7.2 Physics Driven Detector Requirements: Structure Function Measurement

There are several components of the MINERνA detector design that impact DIS physics. In a deeply inelastic event, the probing particle breaks apart the nucleus and a hadronic shower is present in the final state. The detector must have sufficient mass to contain the shower and measure the energy at the hadronic vertex. In MINERνA the calorimeters serve the function of stopping hadrons and measuring their energy. The design of the calorimeters was optimized to provide adequate hadronic shower energy resolution and good hadron containment.

The measurement of the neutrino differential cross section and structure functions relies on accurate determination of the event kinematic variables. Figure 26 shows the effect of hadron energy resolution on the measured kinematic variable distributions, x, y, and Q^2, for the nominal resolution of $22\%/\sqrt{E_H}$. The hadronic energy resolution has a large impact on the measured y distribution. Figure 27 shows how the smearing changes as the hadron energy resolution is varied from $11\%/\sqrt{E}$ (half the nominal value) up to $44\%/\sqrt{E}$ (twice nominal). Clearly a resolution of twice nominal significantly degrades the measured y distribution, which decreases significantly the ability of MINERνA to precisely measure the y dependence of the differential cross section.

To fully determine the kinematics of a charged-current neutrino scattering event, the momentum of the outgoing muon track must be measured. This adds a requirement that the calorimeters be thick enough to identify tracks exiting the inner detector and to track them into the minos near detector

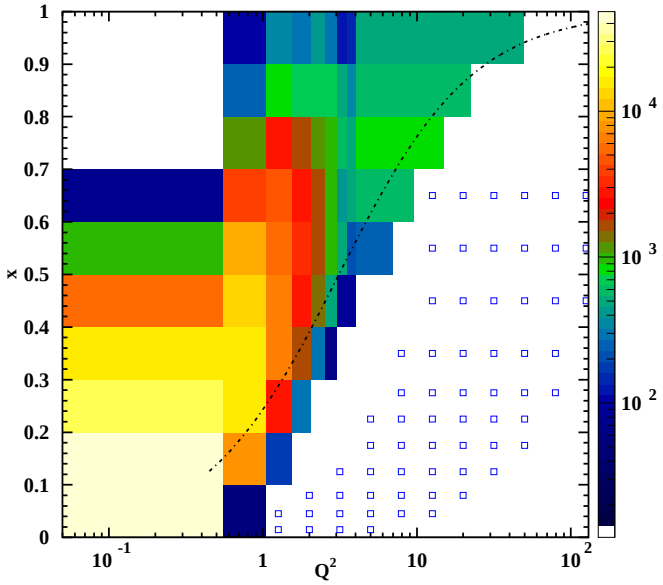

Figure 25: Available xF_3 data (open symbols) and the anticipated (resonant region) MINERνA data (colored distributions) in x_{Bj} vs. Q^2. The curve indicates the commonly-accepted W^2 = 4 GeV^2 boundary between the resonant and deep-inelastic regimes. The color key to the right shows the corresponding, expected MINERνA statistics.

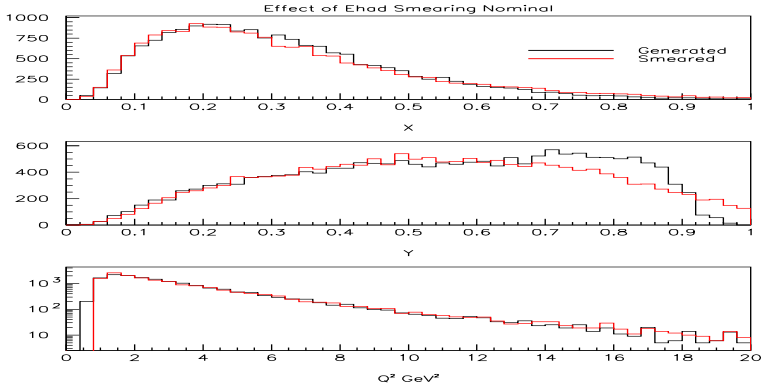

Figure 26: Effect of hadron energy resolution on the measured kinematic variable distributions (x, y, and Q^2) for the nominal resolution of 22%/$\sqrt{E_H}$.

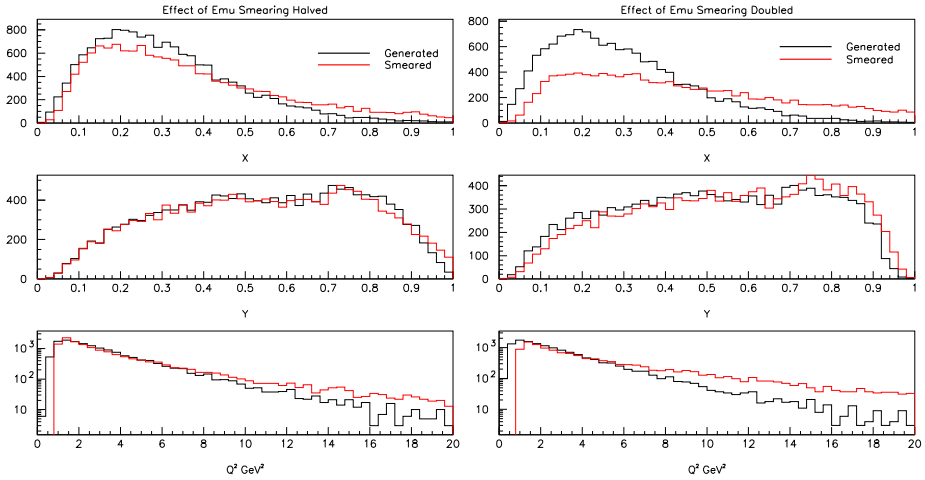

Figure 27: Effect of hadron energy resolution on the measured kinematic variable distributions (x, y, and Q^2) for the resolution of 11%/$\sqrt{E}$ (left) and 44%/$\sqrt{E}$ (right).

where their momentum is measured. The MINERνA design, which uses the minos near detector as a muon spectrometer, has adequate acceptance and momentum resolution for muons. Figure 28 shows the effect of muon momentum resolution on the measured kinematic variable distributions for the nominal muon momentum resolution of 12% for the minos near detector. Figure 29 shows how

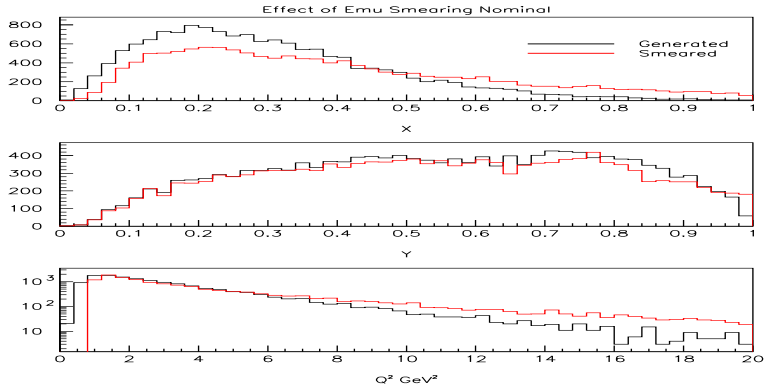

Figure 28: Effect of muon momentum resolution on the measured kinematic variable distributions (x, y, and Q^2) for the nominal muon momentum resolution of 12% for the minos near detector.

the smearing changes as the muon momentum resolution is varied from 6% (half the nominal value) up to 24% twice nominal. Clearly the resolution of 24% has significantly degraded the measured x and Q^2 distributions, which decreases significantly the ability of MINERνA to measure structure functions.

Accurate measurement of the structure functions also requires precise control of systematic uncertainties. The largest systematic uncertainties arise from knowledge of the experiement's absolute

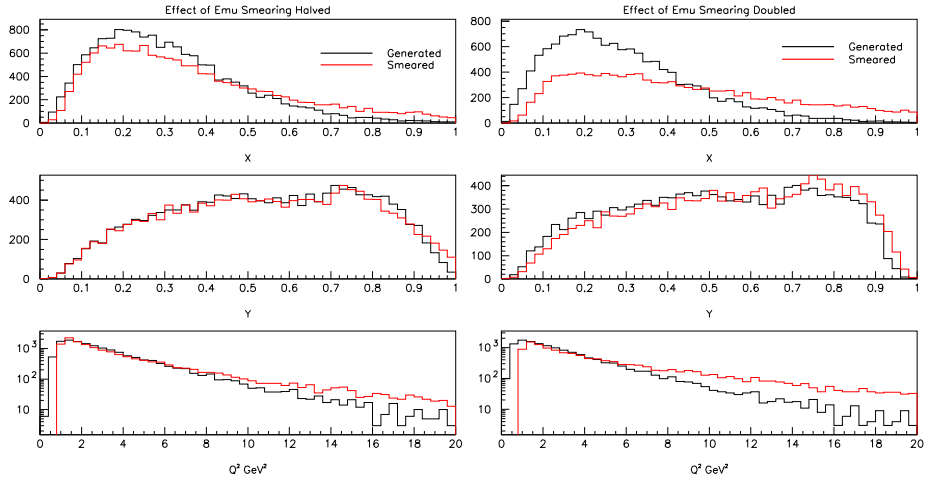

Figure 29: Effect of muon momentum resolution on the measured kinematic variable distributions (x, y, and Q^2) for the muon momentum resolution of 6% (left) and 24% (right).

energy scale. This affects measurement of the kinematic variables and limits how well the Q^2 dependence of the structure functions can be determined. Figure 30 shows the effect of two values of energy scale uncertainty on measurement of the structure function F_2.

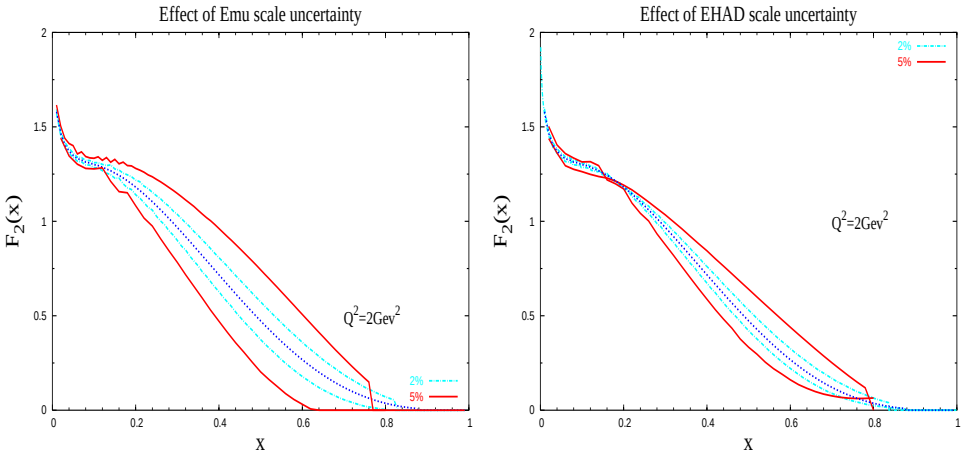

Figure 30: Effect of energy scale uncertainties on x-dependence of F_2 at Q^2=2GeV^2. Uncertainty due to muon energy scale is shown on the left for 2%(blue) and 5% (red) scale uncertainties. The same curves for hadron energy scale are shown on the left.

2.8 Generalized Parton Distributions

One of the main goals of subatomic physics is to understand the structure of hadrons, and in particular the structure of the nucleon. The primary approach to this problem has been measurement of the nucleon form-factors, with (quasi-)elastic scattering (for Q^2 up to a few (GeV/c)^2), parton densities, through inclusive deep-inelastic scattering (DIS), and distribution amplitudes, through exclusive processes. However, the usual parton densities extracted from DIS are only sensitive to the longitudinal component of the parton distributions and do not give information on the transverse component, or other contributions to the nucleon angular momentum.

2.8.1 The Nucleon Spin Puzzle and GPDs

In the late 1980's, results from polarized DIS showed that a relatively small fraction, about 20%, of the nucleon spin is carried by the valence quarks. The obvious candidates for the missing spin were the quark and gluon orbital momentum and gluon helicity. However, information on those quantities cannot be extracted from DIS.

In 1997, Ji [82, 83] showed that a new class of nucleon observables, which he called "off-forward parton distributions", could be used to determine the spin structure of the nucleon. This work, along with developments by others, especially Radyuskin [84, 85] and Collins [86] showed that these distributions, now called generalized parton distributions (GPDs), had the potential to give a full three-dimensional picture of the nucleon structure. This exciting development has led to an immense amount of theoretical work in the last few years. Short reviews can be found in [87, 88] and a comprehensive review can be found in [89].

Ji showed that in leading twist there are four GPDs, which he called H, $\tilde{H}$, E, and $\tilde{E}$, for each quark flavor. H and $\tilde{H}$ are nucleon helicity-conserving amplitudes and E and $\tilde{E}$ are helicity-flipping amplitudes. The GPDs are functions of x, ξ (a factor determining the "off-forwardness" of the reaction), and the total momentum-transfer squared, t. The GPDs can be accessed experimentally through reactions proceeding via the "handbag" diagram shown in Figure 31.

2.8.2 Deeply-virtual Compton Scattering

The most promising reaction to measure GPDs identified so far is deeply-virtual Compton scattering (DVCS). The DVCS reaction is shown in Figure 32a. An interesting feature of DVCS is that it can interfere with the Bethe-Heitler process, Figure 32b, which is completely calculable in terms of the nucleon elastic form-factors. This interference causes an asymmetry in the azimuthal distribution of the scattered proton allowing some quantities to be determined that would otherwise require a polarized target. However, DVCS involves a combination of the four GPD amplitudes, which cannot be separated using DVCS alone. Some complementary information can also be obtained from nucleon form-factor measurements and deep exclusive meson electroproduction.

Neutrino scattering provides a very similar reaction to DVCS. In this case, the virtual mediator is a $W^{\pm}$ with the production of an energetic photon, a $\mu^{\pm}$, with either a recoiling nucleon or nucleon resonance, as shown in Fig. 33. This "weak DVCS" reaction is very promising theoretically because it provides access to different GPDs than DVCS. It will help resolve the individual flavors, e.g. d

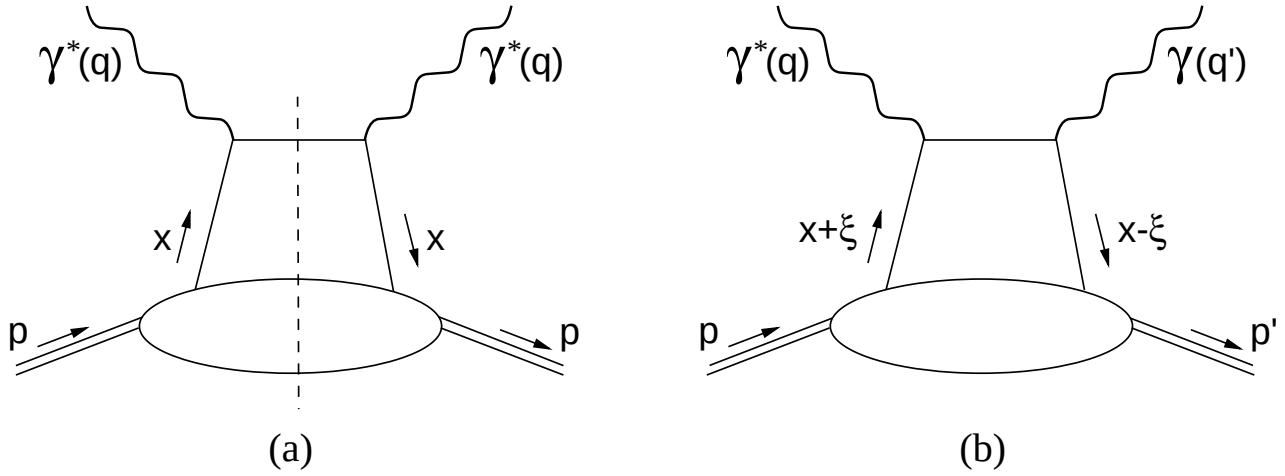

Figure 31: (a) Forward virtual Compton amplitude which describes the DIS *cross-section* via the optical theorem ($x_B = x$); (b) Handbag diagram occurring in the DVCS *amplitude*.

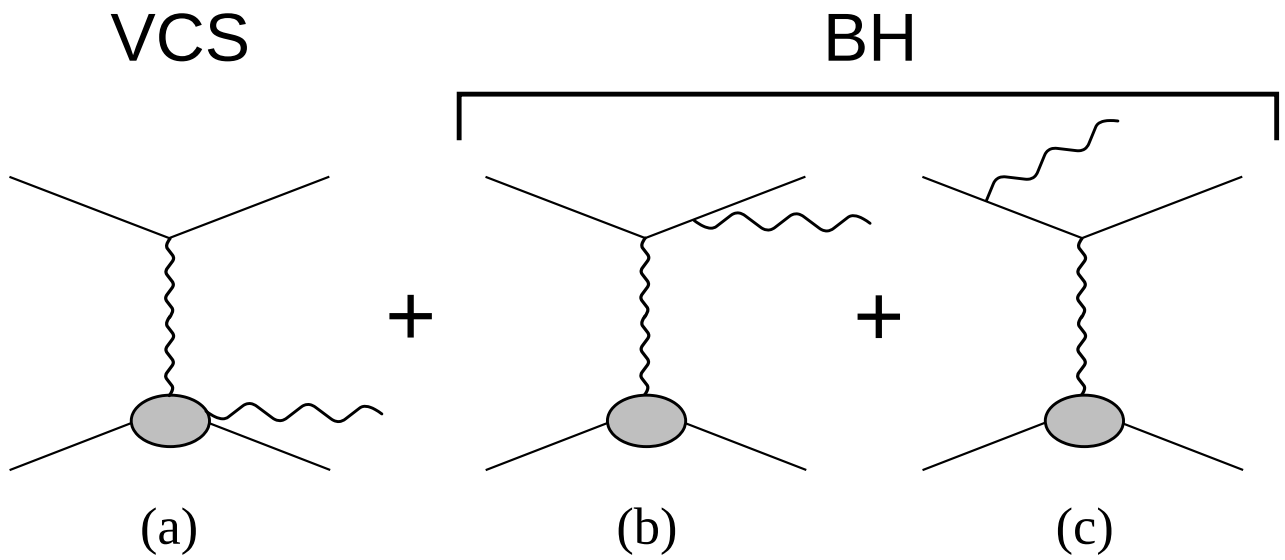

Figure 32: The DVCS process (a) along with the interfering Bethe-Heitler diagrams (b) and (c).

in neutrino scattering and u in anti-neutrino scattering, and the interference of the V and A currents will give access to C-odd combinations of GPDs.

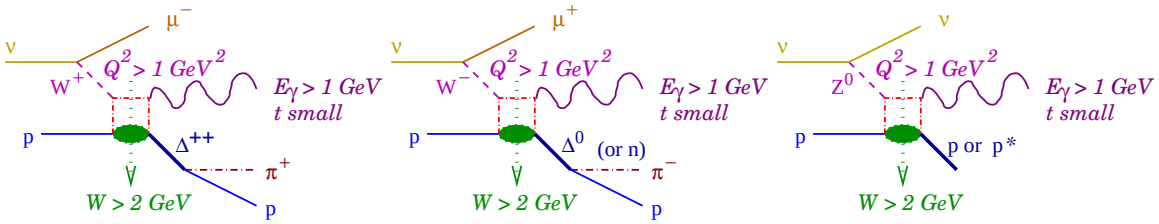

Figure 33: Reactions sensitive to GPDs in neutrino scattering.

2.8.3 Measurement of GPDs in MINERνA

Measurement of the GPDs requires measurement of exclusive processes. In addition, certain kinematic limits must be imposed to allow reliable calculations. In particular, the reaction should be above the resonance region ($W^2 > 4$ GeV^2), the momentum transfer should be small ($t < 0.2$ (GeV/c)^2), and Q^2 should be large ($Q^2 > 2$ (GeV/c)^2), which implies a high-energy photon and low-energy nucleon in the final state. Although this does present certain experimental difficulties, it should be possible to detect these for charged currents in MINERνA. A. Psaker, a student of A. Radyuskin, has made detailed calculations of the weak DVCS process for neutrinos in the 5-20 GeV range with the above kinematic constraints. He finds a cross-section of about 10^{-41} cm^2/neutron for CC reactions, with a relatively small energy dependence (the useful cross section increases slightly from 5 to 20 GeV). The cross section for protons (giving a $\Delta^{++} \rightarrow p\pi^+$ in the final state would be about half the neutron cross section. This would yield $\approx$ 10,000 events for the full four-year run with a 3 ton active target.

Additionally, recent work at JLab studying GPD's using DVCS have given promising results [90] for the prospects of measuring GPD's with few GeV neutrinos. The JLab results show a clear signal for GPD's measured at modest Q^2 - 1.5-2.3 GeV^2 - with a 5.75 GeV electron beam, in rough agreement with theoretical expectations. Detailed calculations for neutrino scattering are currently being done W. Melnitchouk and A. Psaker [91] which will give more precise predictions for expectations of measuring GPD's with MINERνA.

Background studies have not yet been performed, but the most significant background should be events with a photon radiated by the out-going muon. It should be pointed out that these will be primarily for reactions on neutrons in carbon, not free nucleons. We are still studying this reaction to assess the effect of extracting GPDs from a bound nucleon.

2.9 Nuclear Effects in Neutrino Interactions

2.9.1 Introduction

Most neutrino experiments, including neutrino oscillation experiments, require massive nuclear targets/detectors to obtain useful reaction rates. Analysis of neutrino reactions with nuclear media requires understanding the nuclear environment's effect on the process [92]. There are two general categories of such nuclear effects:

- The neutrino interaction probability on nuclei is modified relative to free nucleons. Nuclear effects of this type have been extensively studied using muon and electron beams, but have not been explored with neutrinos. Depending on the kinematic region, these nuclear effects can be quite different for neutrinos [93], and are important for neutrino energies typical of oscillation experiments.

- Hadrons produced in a nuclear target may undergo final-state interactions (FSI), including re-scattering and absorption. These effects may significantly alter the observed final-state configuration and measured energy [94, 95], and are sizable at neutrino energies typical of current and planned neutrino oscillation experiments [136].

The hadron shower observed in neutrino experiments is actually the *convolution* of these two effects. FSI effects are dependent on the specific final states that, even for free protons, differ for neutrino and charged-lepton reactions. The suppression or enhancement of particular final states by nuclear effects also differs for neutrino and charged lepton reactions. For these reasons, measurements of nuclear effects with charged leptons cannot be applied to neutrino-nucleus interactions without considerable care.

In addition to the above effects, there is strong evidence that hadron properties are modified in the nuclear medium [124]. Extraction of any nucleon properties from nuclear targets, even as light as ^{4}He, requires understanding such modification.

To study these questions in MINERνA, carbon, iron and lead targets will be installed upstream of the pure scintillator active detector, with tracking detectors surrounding them, and a liquid ^{4}He target will be installed upstream of the main detector. To measure the overall effect of the nucleus, the observed interaction rate, hadron spectrum and multiplicity will be measured for all four targets.

2.9.2 Modified Interaction Probabilities

Pronounced nuclear effects have been measured in *charged-lepton* scattering from a number of nuclear targets. The experimental situation is discussed in review papers [97, 98].

The mechanisms of nuclear scattering have also been studied theoretically. These mechanisms appear to be different for small and large Bjorken x as viewed from the laboratory system. Bjorken x is defined as $x = Q^2/2M\nu$, where ν and $\boldsymbol{q}$ are energy and three-momentum transfer to the target and $Q^2 = \boldsymbol{q}^2 - \nu^2$. The physical quantity discriminating between large and small x regions is a characteristic scattering time, which is also known as Ioffe time (or length) $\tau_I = \nu/Q^2$ [99]. If τ_I is smaller than the average nuclear separation between nucleons, the process can be viewed as incoherent scattering off bound nucleons. This occurs for larger $x(> 0.2)$.

At small Bjorken x the space-time picture is different. The underlying physical mechanism in the laboratory reference frame can be sketched as a two-stage process. In the first stage, the virtual photon γ^* (or W^* or Z^* for neutrino interactions) fluctuates into a quark-antiquark (or hadronic) state. This hadronic state then interacts with the target. The uncertainty principle allows an estimate of the average lifetime of such a fluctuation as

$$\tau = 2\nu/(m^2 + Q^2), \tag{5}$$

where m is the invariant mass of the hadrons into which the virtual boson converts. The same scale τ also determines the characteristic longitudinal distances involved in the process. At small x, τ exceeds the average distance between bound nucleons and coherent multiple interactions of this hadronic fluctuation in a nucleus are important. It is well known that the nuclear shadowing effect for structure functions results from coherent nuclear interactions by hadronic fluctuations of virtual intermediate bosons (for a recent review of nuclear shadowing see, e.g., [98]).

2.9.3 Nuclear effects in the incoherent regime at large x

If x is large enough to neglect coherent nuclear shadowing, lepton scattering off a nucleus can be approximated as incoherent scattering from bound protons and neutrons. The most pronounced nuclear effects in this region are due to Fermi-motion, nuclear binding [100, 101, 102, 103, 104, 105, 106], and off-shell modification of nucleon structure functions [105, 106, 107, 108, 111].

A widely used approximation in description of nuclear structure functions is to neglect the final state interactions of resulting hadrons with the recoiling nucleus. In this approximation the nuclear structure functions can be written as the bound nucleon structure function averaged (convoluted) with the nuclear spectral function (for derivation and more details see [102, 105, 111]). Since bound nucleons are off-shell particles their quark distributions generally depend on nucleon virtuality k^2 as an additional variable. Off-shell effects in structure functions can be viewed as a way to describe in-medium modification of structure functions. This effect was discussed in terms of different approaches in the literature [104, 108, 105, 107, 110, 111].

Predictions of the convolution approach are compared to data on charged-lepton deep-inelastic scattering in Figure 34. Model calculations of nuclear structure functions use realistic nuclear spectral functions. Data seem to indicate that some off-shell modification of bound nucleon structure function is necessary [111]. The right panel of Figure 34 displays the ratio of lead and carbon structure functions calculated within the same approach. It appears nuclear effects at large x are practically saturated in carbon. Similar effects are predicted for neutrino structure functions F_2 and xF_3. MINERνA will provide valuable information on nuclear effects in this region.

2.9.4 Nuclear effects at small x

Nuclear shadowing effects have been discussed extensively in the literature. A recent paper [98] reviews both experimental data and theoretical models of nuclear shadowing for charged-lepton scattering. This effect is interpreted as the coherent interaction of a hadronic component of the virtual photons with the target nucleus. The structure functions at small x can be represented as a superposition of contributions from different hadronic states.

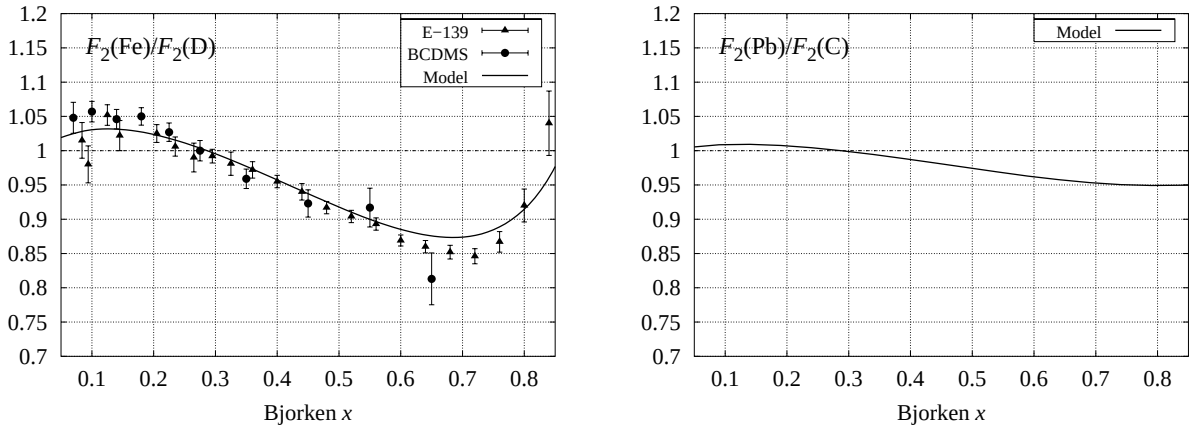

Figure 34: The ratio of iron to deuterium structure functions as measured by SLAC E-139 and CERN BCDMS collaborations in experiments with electron and muon beams (left panel). Also shown are the results of model calculation at fixed $Q^2 = 10\,\mathrm{GeV}^2$ which account for binding, Fermi-motion and off-shell effects in nuclear deep-inelastic scattering [111]. The ratio of lead and carbon structure functions calculated at fixed $Q^2 = 10\,\mathrm{GeV}^2$ within the same approach is presented in the right panel.

In fixed-target experiments events with small Bjorken x are correlated with low four-momentum transfer (Q^2). At low Q^2 the vector meson dominance model (VMD) appears to be a good tool to study nuclear corrections to structure functions [98, 112]. In VMD the structure functions are saturated by contributions from a few low-mass vector meson states. For the interactions driven by the electromagnetic current usually only the isovector ρ and the isoscalar ω and ϕ mesons are important at low $Q^2 < 1\,\mathrm{GeV}^2$ [112]. The structure functions in this model have strong Q^2 dependence. In the generalized versions of VMD, higher-mass states including the continuum have also been considered, making the model applicable at higher Q^2 [98, 112].

The VMD approach has also been applied to weak interactions [113]. The vector current, in close analogy with the electromagnetic current, is assumed to be saturated by ρ meson contribution at low Q^2. The axial-vector channel requires inclusion of contributions from the axial-vector meson a_1. There are still a number of interesting physics questions related to the analysis of the axial-vector channel for neutrino interactions.

It should be emphasized that neutrino scattering at low Q^2 is dominated by the axial current. Indeed, contributions to the structure functions (and cross-sections) from the vector current vanish as $Q^2 \to 0$ due to vector-current conservation. The axial current is not conserved and for this reason the longitudinal structure function F_L does not vanish at low Q^2. It was observed long ago by Adler that neutrino cross-sections at low Q^2 are dominated by the contribution from the divergence of the axial current [114]. The latter, because of PCAC, is saturated by the pion contribution, so low Q^2 neutrino cross-sections and structure functions are determined by pion cross-sections. For the longitudinal structure function at low Q^2 the Adler relation is

$$2x F_L^{\mathrm{PCAC}} = \frac{f_\pi^2}{\pi}\sigma_\pi(s, Q^2), \tag{6}$$

where $f_\pi = 0.93 m_\pi$ is the pion decay constant (m_π is the pion mass) and $\sigma_\pi(s, Q^2)$ the total pion cross-section at the center-of-mass energy $s = Q^2(1/x - 1) + M^2$ for an off-shell pion with mass $\sqrt{Q^2}$. Equation (6) determines the dominant contribution to F_2 and neutrino cross-sections at small Q^2 for nucleon and nuclear targets.

It is important to realize that Eq. (6) is not a consequence of the pion dominance of the axial current, i.e. fluctuation of the axial current to a pion which interacts with the target [117]. Indeed, the single-pion fluctuation of the axial current gives a vanishing contribution to the neutrino cross-section. Instead, the axial current in neutrino interactions can produce heavy states such as the a_1 meson and $\rho\pi$ pair, which interact with the target. The overall contribution of all such states is described by the PCAC relation. The detailed mechanism of this phenomenon is not fully understood and MINERνA can provide new insights on physics driven by the axial current in neutrino interactions.

The strength of nuclear shadowing is controlled by mesonic cross-sections σ_v for the vector current. In the axial-vector channel the relevant quantity is the pion cross-section. To quantitatively understand nuclear effects, the multiple scattering effect on the cross-section is calculated using Glauber–Gribov multiple scattering theory [115, 116, 112, 117]. If l_f is small compared with the nuclear radius, as is the case for heavy nuclei, then multiple scattering effects are important. It should be emphasized that the multiple scattering correction is negative because destructive interference of the forward scattering amplitudes on the upstream nucleons causes *shadowing* of virtual hadron interactions on the back-face nucleons.

The onset of coherent nuclear effects can be estimated by comparing the coherence length of hadronic fluctuation L_c with the average distance between bound nucleons in the nucleus d. For hadronic fluctuation of the vector current L_c is similar to the fluctuation time τ from Eq. (5), where m is the mass of hadronic state in question. Coherent nuclear effects occur if the fluctuation time is large enough $\tau > d$. This condition requires high energy transfer ν and, as is clear from Eq. (5), the coherent region begins at lower energy for smaller masses m. Since $\tau < 2\nu/Q^2$ for any intermediate state, the region of coherent nuclear effects is limited to small x for any Q^2, $x < 1/Md$. Nuclear shadowing saturates if $L_c \gg R$, which happens at small x, and the condition $L_c \sim R$ defines the transition region with strong x dependence of the ratio $\delta\sigma_A/\sigma_N$.

For the axial-vector current, the fluctuation time τ is also given by Eq. (5). However, as argued in [117], the fluctuation and coherence lengths are not the same in this case. In particular, the coherence length is determined by the pion mass m_π in Eq. (5) because of the dominance of off-diagonal transitions like $a_1 N \to \pi N$ in nuclear interactions. Since the pion mass is much smaller than typical masses of intermediate hadronic states for the vector current ($m_\rho,\ m_\omega$, etc.), the coherence length L_c of intermediate states of the axial current at low Q^2 will be much larger than L_c for the vector current. A direct consequence of this observation is early onset of nuclear shadowing in neutrino scattering at lower energy and Q^2 compared to charged-lepton scattering.

Figure 35 shows the calculated ratios of iron to nucleon and lead to carbon structure functions at two different Q^2 values as a function of x. We also compare the nuclear shadowing effect for muon and neutrino scattering. The basic reason for the earlier onset of nuclear shadowing in neutrino scattering and different behavior in the transition region is the difference in correlation lengths of hadronic fluctuations between the vector and axial-vector currents. This is also illustrated by the

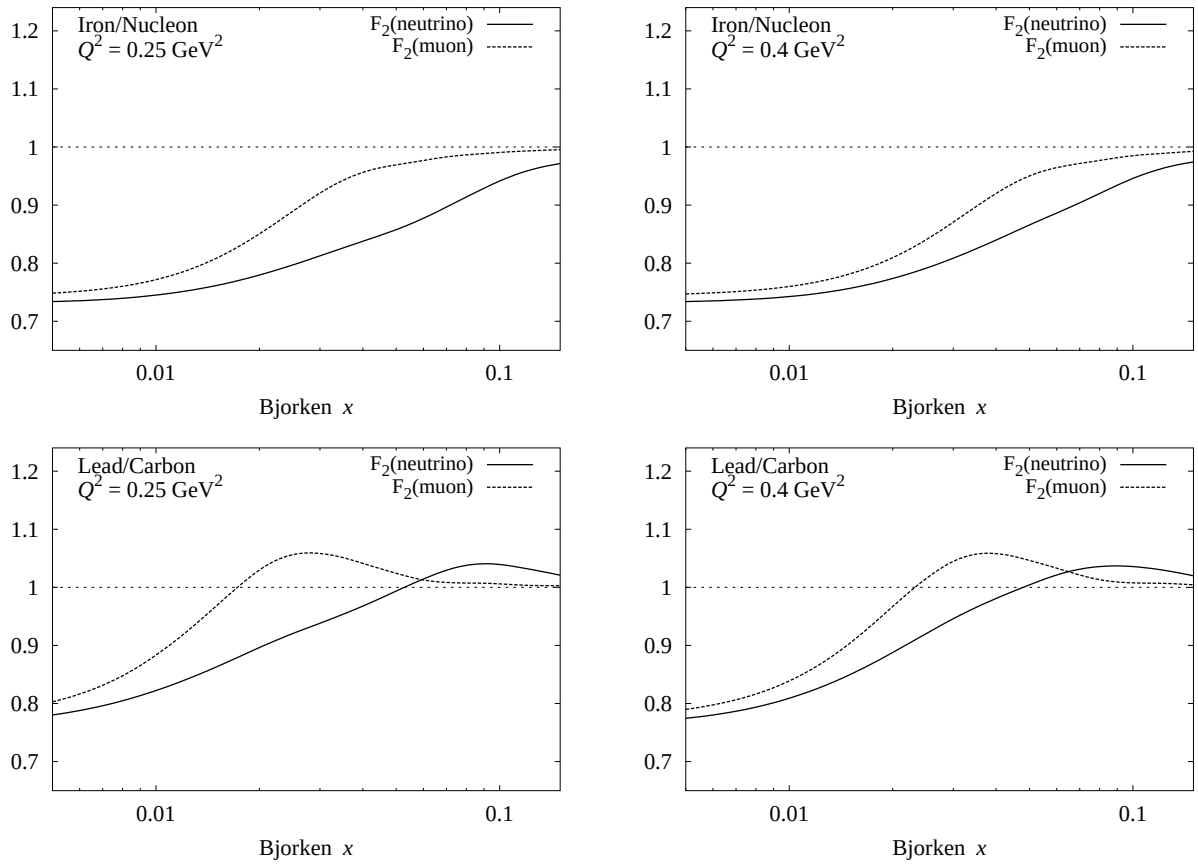

Figure 35: The ratio of iron to nucleon (upper row) and lead to carbon neutrino CC structure functions F_2^ν calculated at two different Q^2 within an approach based on PCAC and VMD (solid line). The dashed line shows similar ratios for the muon structure function F_2^μ.

observation that for a given Q^2 the cross-section suppression due to shadowing occurs for much lower energy transfer (ν) in neutrino interactions than for charged leptons.

The relative nuclear shadowing effect for the structure function xF_3 should be substantially different than that of F_2 [118]. This is because xF_3 describes the correlation between the vector and the axial-vector current in neutrino scattering. In terms of helicity cross-sections, xF_3 is given by the cross-section asymmetry between the left- and right-polarized states of the virtual W boson. It is known that such a difference of cross-sections is strongly affected by Glauber multiple scattering corrections in nuclei. This leads to enhanced nuclear shadowing of xF_3.

The resulting ratio of lead and carbon structure functions are shown in Figure 36. Unlike nuclear effects at large Bjorken x (Figure 34), there are substantial, structure-function dependent nuclear effects at small x. MINERνA can provide a unique tool to study these effects.

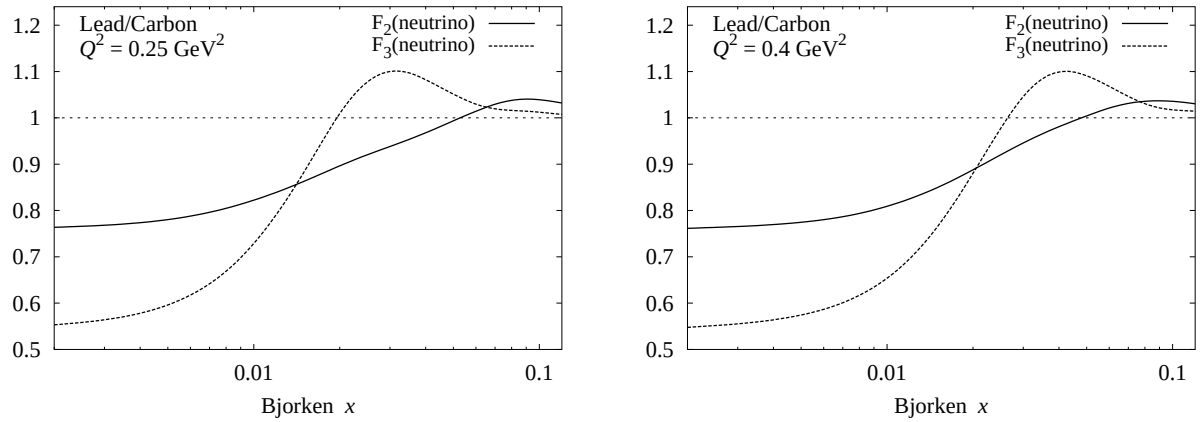

Figure 36: The ratio of lead to carbon neutrino charged-current structure functions F_2 calculated in an approach based on PCAC and VMD at two different Q^2 (solid line). The corresponding ratio for xF_3 is shown by the dashed curve.

2.9.5 Determination of $\sin^2\theta_W$

The rates of neutral-current (anti-)neutrino scattering are directly determined by $\sin^2\theta_W$. Therefore the measurement of NC/CC ratios of neutrino cross-sections provides a valuable tool for determination of $\sin^2\theta_W$. For an isoscalar target (e.g. the isoscalar combination of proton and neutron, or for deuterium) a relation between neutrino–antineutrino asymmetries in the NC and CC DIS cross-sections was derived by Paschos and Wolfenstein [119]

$$R^- = \frac{\sigma^\nu_{\rm NC} - \sigma^{\bar\nu}_{\rm NC}}{\sigma^\nu_{\rm CC} - \sigma^{\bar\nu}_{\rm CC}} = \frac{1}{2} - \sin^2\theta_W, \tag{7}$$

where θ_W is the weak mixing angle. A similar relation also holds for the NC/CC ratio of structure functions

$$F_3^{\rm NC}(x,Q^2)/F_3^{\rm CC}(x,Q^2) = 1 - 2\sin^2\theta_W, \tag{8}$$

where $F_3^{\rm CC}$ is the neutrino and antineutrino averaged structure function, $F_3^{\rm CC} = (F_3^\nu + F_3^{\bar\nu})$.

If only the contributions of light quarks are taken into account, the PW relationship is a direct result of isospin symmetry. This ensures that various strong interaction effects, including nuclear effects, cancel out in R^- for an isoscalar target, making Eq. (7) a powerful tool for measurement of the mixing angle in neutrino scattering.

The targets used in neutrino experiments are usually heavy nuclei, such as iron in the NuTeV experiment [120]. Heavy nuclei typically have an excess of neutrons over protons and therefore are not isoscalar targets. For a non-isoscalar target the relations (7) and (8) are violated by contributions from isovector components of nuclear parton distribution functions. Nuclear corrections to relations (7) and (8) were recently studied in [121, 122, 123], which showed that nuclear effects enter through non-isoscalar effects in the target. These studies suggest that nuclear corrections should be greatly

reduced for isoscalar targets like carbon. MINERνA, with its lead, iron, and carbon targets, can directly measure the NC/CC ratio for several nuclear targets to explore these effects experimentally.

2.9.6 Modification of the nucleon form factors

The question of whether the structure of a bound nucleon differs from the structure of a free nucleon has long been of interest. The change in nuclear structure functions are known to be modified (the EMC effect) [125], the axial vector coupling constant is quenched in nuclear β decay [126], and studies of the electromagnetic form factors in ^{4}He at Jefferson Lab indicate that the ratio of the electric to magnetic form factor is about 10% smaller in ^{4}He than for the free proton [127].

Recent calculations by Tsushima *et al.* based on the quark-meson coupling model predict over a 10% reduction in the axial form factor in nuclei compared to the free nucleon [124], for Q^2 below 1.5 GeV^2, where the model is expected to be valid. The average density of nuclei increases quickly, so the effect is substantial even in a nucleus as light as ^{4}He. Because the axial form factor will be extracted from measurements on nuclei, it is essential that the any nuclear effect be determined.

Since we will not have a hydrogen or deuterium target in our initial run, it is not possible to make a direct study of nuclear effects on the form factors. Fortunately, the work of Tsushima has shown that the ratio of the form factors in lead to carbon, as shown in Fig. 37, is about 5% lower than unity for the axial form factor.

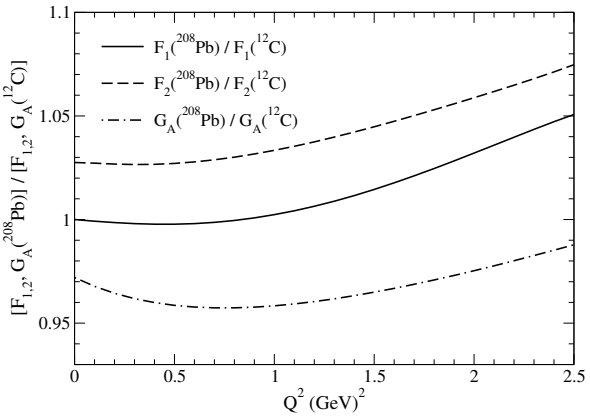

Figure 37: Predicted ratio of the axial form factor as measured in Pb to C, from Ref. [124].

The statistical uncertainties on this measurements will be small. In the Q^2 range of 0.75-1.25 GeV2, where the effect is largest, we expect about 330,000 events in Pb, 1.1 million events in C, and about 100,000 events in He. About 80,000 events will be in the pure C target, which will allow a comparison with comparable systematics to both iron and lead. The comparison with He will be extremely valuable in this case because of the ability to compare with the high precision JLab measurements of experiment E03-104 [128], which is measuring the ratio of the electric to magnetic form factor of the proton in ^{4}He near a Q^2 of 1 GeV2. The protons produced at Q^2 near

1 GeV2 will have an energy of about 500 MeV and are produced at an angle of about 45°, which will allow coincident detection with the muon. In addition, complicating factors such as final state interactions are much smaller in helium than heavier nuclei, which will facilitate the comparison with measurements on hydrogen and deuterium when those do take place.

2.9.7 Final-state Interactions

Overview - Pion Absorption Interactions of few-GeV neutrinos with nuclei often produce resonances which decay to pions. Any attempt to reconstruct the incident neutrino energy based on the total observed energy must account for pion interactions within the target nucleus. Existing neutrino interaction Monte Carlos (such as INTRANUKE [19]) handle intra-nuclear pion interactions crudely and have generally not incorporated the latest knowledge of pion interactions.

The concern is mainly with pions in the 100–500 MeV range, where the interaction cross-sections are highest. In this range the pion/nucleon cross-section is dominated by the strong $\Delta(1232)$ resonance. The Δ is a fairly narrow (about 100 MeV) resonance, and the pion-nucleon cross-section reflects this, with a peak near 200 MeV pion energy which drops quickly above and below this. The pion/nucleus cross-section exhibits a similar behavior, with a less pronounced drop-off at higher energy. The charged-pion/nucleus cross-section has four important components in the intermediate energy range: elastic scattering (nucleus left in the ground state), inelastic scattering (nucleus left in an excited state or nucleon knocked out), true absorption (no pion in the final state), and single charge exchange (neutral pion in the final state).

Neutrino detectors are mainly iron (absorber), oxygen (water) and carbon (scintillator). The total pion–carbon cross-section is 600 mb, with elastic and inelastic cross-sections about 200 mb each, and absorption about 160 mb. The total pion-iron cross-section is about 1700 mb, with elastic and absorption about 600 mb each, and inelastic about 400 mb. Cross-sections for positive and negative pions are nearly the same because nuclei contain about the same number of protons and neutrons. These very large cross-sections mean that many pions will undergo some nuclear reaction within the target nucleus. In elastic and most inelastic reactions the scattered pion will not, because of its small mass, lose much energy. However, absorbed pions will lose all of their kinetic and mass energy. Of the four components of this intra-nuclear cross-section, the absorption probability within the interaction nucleus is roughly 30%. Figure 38 [137] shows absorption cross-sections for various nuclei as a function of pion energy.

Pion absorption cannot occur on a single nucleon due to energy and momentum conservation. The simplest absorption mechanism is on two nucleons. Because absorption appears to proceed mainly through $N - \Delta$ intermediate states, an isospin zero (np) pair is the primary candidate. Such an absorption for a positive pion would give two energetic protons whose kinetic energy nearly equaled the total pion energy. However, early studies of pion absorption found this was not the most probable mechanism.

In the 1990's two large solid angle detectors, the LAMPF BGO Ball and the PSI LADS detector, were built to study pion absorption. The somewhat surprising result from both experiments was that pion absorption is dominated by three body absorption [129]. For positive pions, the absorption on a pnn triplet (leading to a ppn final state) was the most common. This was observed even in ^{4}He. The absorption in heavier nuclei also appears to proceed mainly through a three-body mech-

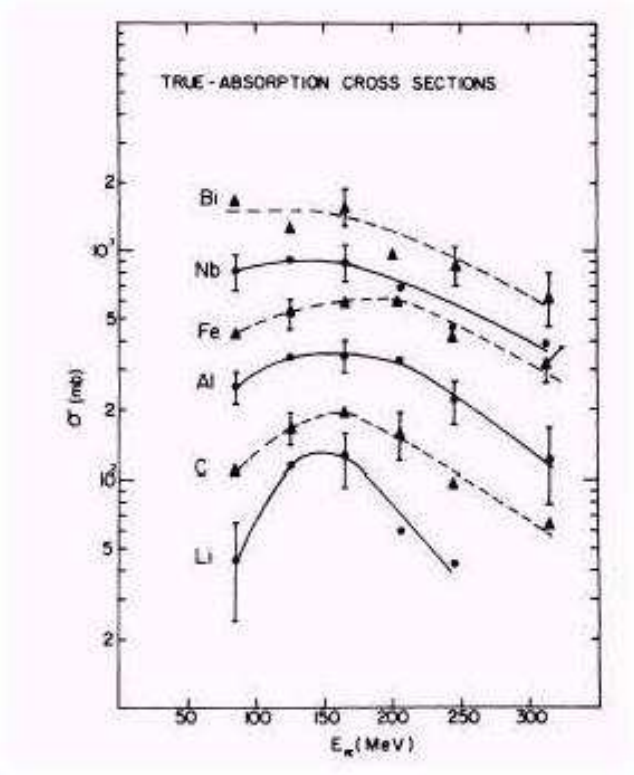

Figure 38: The absorption cross-sections for various nuclei as a function of pion energy.

anism, although increased initial state interactions (pion re-scattering) and final-state interactions (nucleon re-scattering) result in four to five nucleons being emitted. Typically the final-state contains more neutrons than protons. The absorption process, which is still not well understood theoretically, largely fills the available phase space thus giving a wide range of nucleon energies with little angular dependence. Because much of the energy is in neutrons, the visible energy is well below the total pion energy. Even in carbon more than half the energy is lost to unobserved particles, a fraction which increases with pion energy and with A [130].

The situation is worse for negative pions. Charge symmetry would indicate that the primary absorption should be on a ppn triplet leading to a pnn final state. In this case, most of the pion energy would be in neutrons, and hence effectively invisible. However, if the interaction vertex and one proton energy is known, and the angles of the outgoing neutrons are known, the total energy of the three nucleons can be estimated. Monte Carlo studies with realistic absorption models will be needed to determine the accuracies of such estimates.

Although neutral pions escaping the nucleus will decay, usually to two photons, the mean distance traveled before decay is a few nanometers, much greater than the size of the nucleus. Thus the absorption of neutral pions in the interaction nucleus must also be accounted for in any study of resonance production.

For MINERνA, studies with INTRANUKE have begun to explore the sensitivity to the prob-

ability of pion absorption in the interaction nucleus. Monte Carlo routines are being modified to treat pion absorption more realistically. Unfortunately there are essentially no measurements of pion absorption above 500 MeV. The fine spatial resolution and 4π acceptance of MINERνA will allow study of these interactions, especially in carbon.

Nuclear transparency A second nuclear interaction process which affects the observed energy is final state interaction of a nucleon in the struck nucleus. An outgoing nucleon has a substantial probability of interacting in the nucleus. These probabilities have been measured, most recently at Jefferson Lab, with some precision. The experiments used $(e, e'p)$ coincidence reactions, and the cross-section for finding the scattered electron in the quasi-elastic peak was compared to the cross-section for finding the coincident proton.

Unlike pion absorption, there is little available information on what happens to the scattered nucleon. Of course, most either scatter from a single nucleon quasi-elastically or produce a pion (for protons above 600 MeV). Improving Monte Carlo routines to model this interaction should allow us to better estimate the total final state energy. As for pion absorption, the good resolution, neutron detection capability, and full solid angle coverage of MINERνA should allow measurement of the actual final states and help constrain the Monte Carlo models.

2.9.8 Nuclear Effects in MINERνA

To study nuclear effects in MINERνA, helium, carbon, iron and lead targets will be installed upstream of the pure scintillator active detector. The planned configuration involves a total of 5 planes, with planes being mixtures of the various solid targets, as will be described in Section 3.3, and the ^{4}He target upstream. For the standard four-year run described in the proposal, MINERνA would collect about 2 million events on Fe and Pb, 500 thousand events in He, and 1 million events on C as well as 8.4 M events on the scintillator in the fiducial volume.

2.9.9 Measuring modified interaction probabilities

To measure this nuclear effect, the cross-section and resulting structure functions $F_2(x,Q^2)$ and $xF_3(x,Q^2)$ will be measured for the four target nuclei of He, C, Fe and Pb. For an A-dependent comparison in the DIS region ($W \geq 2$ GeV and $Q^2 \geq 1$ (GeV/c)^2) we would expect abour 450 K events in the Pb and Fe targets, 100 K events in He, and 220 K events from the pure carbon target. About 4% of the events are expected to be in the shadowing region ($x \leq 0.1$) and 7% of the events in the high-x region $(x \geq 0.5)$.

To study the axial-vector nuclear shadowing effects expected at low Q^2 (non-DIS events) and high ν we need to compare lead to carbon to get a statistically significant result. The expected number of events with Q^2 less than 0.5 GeV^2 in lead is listed in Table 3, along with the statistical uncertainty on the ratio. The number of events in carbon will be much greater than in lead, because the carbon in the fiducial volume can be used. With these samples, MINERνA can measure the expected difference in lead to carbon shadowing for charged leptons compared to neutrinos to under three standard deviations (statistical).

Table 3: Estimated uncertainty on shadowing ratio for Pb to C.

ν GeV	Events in Pb	Uncertainty on Ratio
6-7	1700	2.7%
7-8	940	3.6%
8-9	720	4.1%
9-10	400	5.4%
10-12	560	4.7%
12-14	410	5.4%
14-20	320	6.1%

2.9.10 Measuring final state interactions

The NEUGEN Monte Carlo has been used to study MINERνA's sensitivity to nuclear effects. Nuclear effects in NEUGEN are controlled by the INTRANUKE processor. This processor incorporates a probability for pion absorption based on earlier electroproduction absorption studies and lower-statistics Ne/H_2 neutrino bubble chamber data. The observed phenomenon of hadron formation length, which increases the transparency and reduces final-state interactions, is incorporated. The particular model used for pion absorption, which is currently being improved and updated, assumes that absorption eliminates a pion and the resulting nucleons are themselves either absorbed in the nucleus or are too low in energy to be observed.

To determine MINERνA's sensitivity to the predictions of this model, the assumed probability for pion absorption in INTRANUKE has been increased by three standard deviations and then decreased by the same amount, which essentially turns off pion absorption completely. The multiplicity and a simple, crude estimate of the visible hadron energy have been examined under these extreme conditions. Other nuclear effects such as intra-nuclear scattering and hadron formation length have not been altered from their nominal values. Figure 39 shows both the true and reconstructed multiplicity distributions for carbon. Unfortunately, the available tracking software fails to reconstruct many of the tracks. We expect this problem to be resolved when full pattern recognition and a more robust tracker become available. For the present study, we will use the true multiplicities.

The next series of figures show the predicted "asymmetry" of the true multiplicity and visible hadron energy. The asymmetry is defined as the percentage change under these extreme assumptions. That is, the bin contents at plus three standard deviations minus the bin contents at minus three standard deviations, divided by bin contents at minus three standard deviations. Figure 40 shows the asymmetry of the true multiplicity for carbon and iron. There is a dramatic effect for carbon, as the high absorption value increases the number of 0-track events by over a factor of six compared to the no-absorption case. This is because the other nuclear effects, being unchanged, are minimal for carbon. Since intra-nuclear rescattering increases as $A^{1/3}$ and the suppression due to hadron formation length decreases as $A^{1/3}$, non-absorption nuclear effects are minimal for carbon and already sizable for lead. If this model is realistic, the carbon multiplicity distribution should be quite sensitive to the probability of absorption.

Final determination of the visible hadronic energy will be an involved process for this experiment.

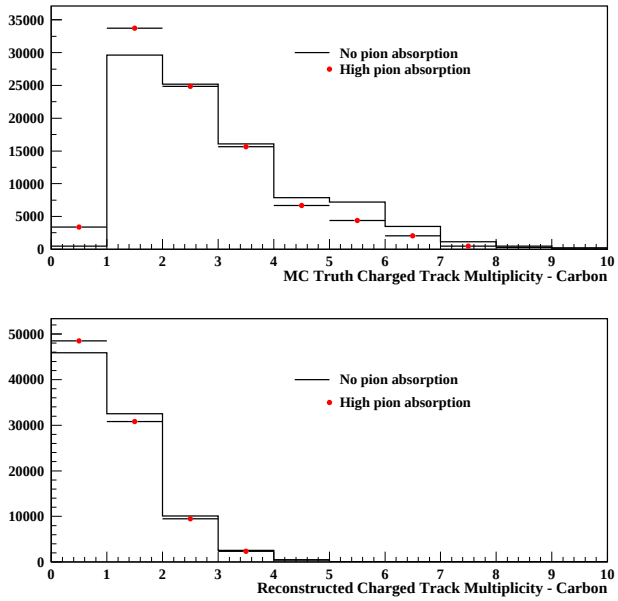

Figure 39: The shift in the true and reconstructed multiplicity distributions between the two values assumed for pion absorption on carbon described in the text.

For now, we use the most primitive estimate of this quantity, an uncorrected version derived from the total light output of the hadron shower. In the real data analysis this can be refined through measurements of stopping/decaying particles. With this crude estimate, the change in hadron energy for iron and lead are shown in Figure 41. There is a significant increase in the number of events with E_H less than 3 GeV and a corresponding decrease in the number of events with higher E_H, as one would expect. MINERνA will collect several times these statistics and should be able to measure this effect at even higher hadron energy.

Since the incoming neutrino energy is not known *a priori*, the measured **muon** kinematics will be tested as a basis for comparing the visible hadron shower across nuclear targets to determine whether a nuclear correction-factor can be parameterized as a function of the observed muon angle and energy. The muon is relatively free from nuclear dependent effects and serves well as an A-independent normalization. For example, the quantity:

$$Q' = E_\mu \sin^2(\theta/2) \tag{9}$$

is representative of the 4-momentum transfer to the nucleon or quark (divided by E_ν) and reflects the energy-momentum transferred to the hadronic vertex. The distribution of events in this quantity is peaked toward low Q'. with half the events below $Q' = 1.0$ GeV.

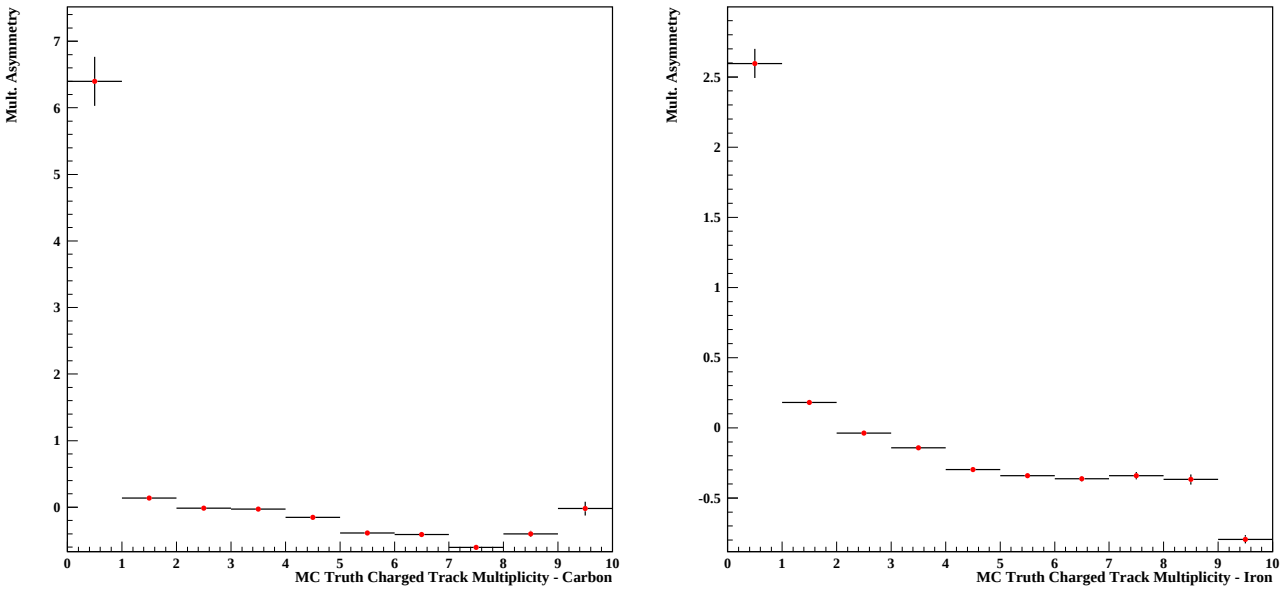

Figure 40: The fractional change in true multiplicity distributions between the two values assumed for pion absorption on carbon (left) and iron (right), as described in the text.

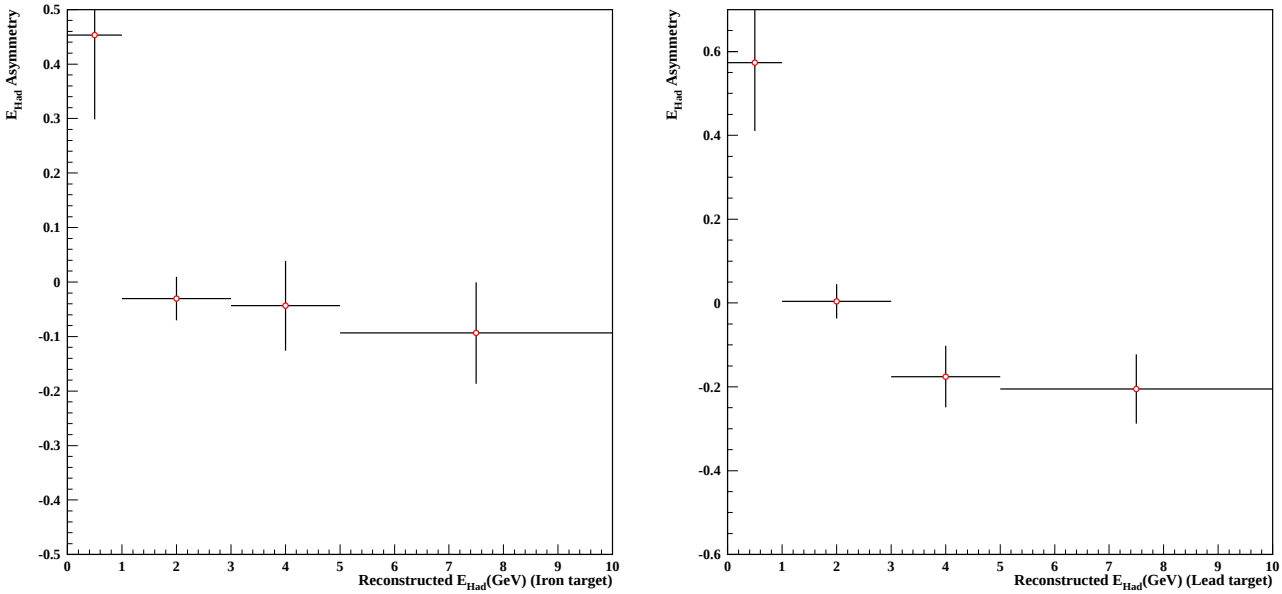

Figure 41: The fractional change in the visible hadron energy distributions between the two values of pion absorption on iron (left) and lead (right), as discussed in the text.

2.10 Neutrino Scattering and Long-Baseline Oscillation Experiments

The field of oscillation physics is about to make an enormous leap forward in statistical precision: first with MINOS in the coming year, and later in T2K and the proposed NOνA experiment. Unfortunately, our relatively poor understanding of neutrino interaction physics in the relevant energy range of these experiments gives rise to systematic uncertainties that could be as large as, or even larger than, their corresponding statistical uncertainties. We have studied the origin of some of these systematic effects, and how MINERνA's measurements can reduce them to well below the statistical level.

2.10.1 Introduction

Over the past five years the field of neutrino oscillations has moved from seeing decades-old anomalies in cosmic ray [142] and solar [143] neutrino data to powerful cross checks of these anomalies (SNO data [144] and angular distributions in atmospheric neutrino data [145]), and most recently to terrestrial confirmation of the oscillation hypothesis (Kamland [146] and K2K [147]). The next steps in this field are to move to precision measurement of the mass splittings and mixing angles already observed, and search for other non-zero off-diagonal elements in the neutrino mixing matrix.

New, extremely-intense beams have been or are being built to greatly increase the statistical reach and ultimate measurement precision for oscillation parameters. With these tremendous improvements in statistical accuracy, however, come new concerns about systematic uncertainties that until now have been a secondary concern. In particular, uncertainties in neutrino cross-sections and nuclear effects lead to systematic uncertainty in the extraction of mixing parameters. Although near detectors are a critical part of precision long-baseline oscillation measurements, they are often ill-suited to make the needed cross-section measurements because they tend to be similar to the coarse and massive far detectors. A near detector can at best constrain the convolution of the near flux, cross-section and detection efficiency. Uncertainties on all of these quantities must be incorporated into the analysis. The cross-section uncertainties we consider are only a subset of the whole, but when flux and efficiency are also taken into account, near-detector performance must be worse than we estimate here.

This chapter is divided into two sections. The first addresses uncertainties relevant for ν_μ disappearance experiments, whose aim is to precisely measure the mass splitting Δm^2_{23}, and the mixing angle which has already been determined to be large, θ_{23}. To achieve these goals the experiments must measure oscillation probabilities as a function of neutrino energy. Two important concerns here are uncertainties in charged-current inelastic processes, and the scale of nuclear effects. Both inelastic channels and the nuclear environment alter the relationship between the true and measured neutrino energies. The second section discusses searches for ν_e appearance, which if observed at accelerator energies would indicate a non-zero value of θ_{13} or more exotic new physics. Because the size of the signal is unknown, the final sample may be dominated by signal (charged-current) cross-sections, and/or background (neutral- and charged-current) processes. In both cases, the experiments of the past are inadequate to precisely predict the far detector event samples.

2.10.2 ν_μ Disappearance

Precision measurement of the mass splitting between two neutrino eigenstates requires analysis of the oscillation probability as a function of neutrino energy (E_ν) divided by baseline (L). The muon neutrino disappearance probability (in the standard 3-generation oscillation parameterization [148]) is

$$P(\nu_\mu \to \nu_\mu) = 1 - \cos^4\theta_{13}\sin^2 2\theta_{23}\sin^2\left(\frac{1.27\Delta m^2_{23}(eV^2)L(km)}{E_\nu(GeV)}\right) - ... \qquad (10)$$

where the additional terms are $\mathcal{O}(\sin^2 2\theta_{13})$ or smaller. Currently Δm^2_{23} is known to within a factor of two and $\cos^4\theta_{13}\sin^2 2\theta_{23}$ must be larger than 0.9, at 90% confidence level [149]. Since $\sin^2 2\theta_{13}$ has been constrained below 0.1 by the CHOOZ reactor experiment[150], this means $\sin^2 2\theta_{23}$ itself is very close to 1. The fact that θ_{23} is close to 45° has been cited as a hint of the underlying symmetry that generates neutrino mass and mixing. Precise measurement of this angle is important because the level at which the mixing deviates from maximal may again give hints about the mechanisms responsible for the breaking that symmetry [151].

More precise measurements of Δm^2_{23} are required to extract mixing angles from eventual ν_e appearance experiments. The challenge of Δm^2_{23} lies in measuring the true neutrino energy in both near and far detectors. Even if the two detectors have an identical design, any uncertainty in the "neutrino energy scale" of the ν_μ charged-current signal translates directly into an uncertainty in the extracted value of Δm^2_{23}.

There are two different ways of measuring neutrino energies: kinematic or calorimetric reconstruction. We discuss both techniques here, and then explain how uncertainties in neutrino interactions lead to energy scale uncertainties and ultimately Δm^2_{23} uncertainties.

The first experiment to provide a precision measurement of Δm^2_{23} will be MINOS [152], which has finished its first year of beam data and presented preliminary results. MINOS uses both far and near detectors, which are magnetized steel-scintillator calorimeters with approximately 6 cm total longitudinal segmentation. The transverse segmentation of the 1 cm thick scintillator planes is 4 cm. MINOS uses Fermilab's NuMI beam, with a baseline of 735 km, which can provide a variety of broad-band neutrino spectra. MINOS does most of its running in the lowest-energy configuration where the peak neutrino energy is about 3.5 GeV, but a long tail extends into tens of GeV.

T2K will use Super-Kamiokande, a water Cherenkov detector, and focus on single-ring muon-like events, for which the neutrino energy is reconstructed kinematically under the hypothesis of two-body scattering. T2K will use a narrow band off-axis neutrino beam from J-PARC in Tokai, whose peak flux is close to 700 MeV, and which originates some 295 km away [154]. The design of the near detectors has not been finalized, but should include a fine-grained tracker and a water Cherenkov detector.

The proposed NOνA experiment will use a calorimetric detector to improve measurement of Δm^2_{23}. Because NOνA is optimized for ν_e appearance rather than ν_μ disappearance, it will use near and far calorimeters made of scintillator planes interspersed with particle board or other scintillator planes. The longitudinal segmentation should be about 1/3 to 1/6 of a radiation length, and the transverse segmentation of the scintillator will be about 4 cm[153]. NOνA will also use the NuMI

beam, but will place its detectors 12–14 mrad off the beam axis, to receive a narrow-band neutrino spectrum. NOνA with a baseline of 810 km, will run with a peak neutrino energy of about 2 GeV.

Kinematic neutrino energy recontruction

Kinematic reconstruction assumes that a given event was produced by a particular process (for example, quasi-elastic scattering) and determines the neutrino energy based on a sufficiently constraining subset of the final-state particles under that hypothesis.

This technique is well-suited to water Cherenkov detectors, which perform best for single-ring topologies. In Super-Kamiokande detector, for example, the ν_μ charged-current signal consists of single-ring, muon-like events, which are primarily quasi-elastic interactions. The energy of the incoming neutrino in that case can be determined using only the outgoing muon momentum (p_μ) and direction (θ_μ):

$$E_\nu = \frac{m_N E\mu - m_\mu^2/2}{m_N - E_\mu + p_\mu \cos\theta_\mu} \tag{11}$$

Since the absolute energy scale for muons can be fixed to within 2–3% by a variety of calibration techniques [131], and the reconstruction algorithms measure ring directions extremely well, it seems plausible that the neutrino energy scale could be determined with comparable precision. However, not all events producing a single muon-like ring are quasi-elastic interactions. Resonant excitation, and even deep-inelastic scattering, where pions are absorbed in the oxygen nucleus or emerge below Cherenkov threshold can lead to the same topology. Such events will have a reconstructed energy well below the true neutrino energy, because the recoiling hadronic mass is larger than assumed. The effect of this inelastic background could be corrected, if the energy-dependent ratio of quasi-elastic and resonant cross-sections were perfectly known, but since it is not, an uncertainty in the effective neutrino energy scale of the detector results.

Because the ν_μ disappearance probability is nearly 100% for T2K, the relative abundance of quasi-elastic and inelastic events will be very different at Super–K than for the unoscillated beam sampled by a near detector.

Precision measurement of the differential cross-sections for single- and multi-pion production, as a function of neutrino energy, will reduce uncertainties in the subtraction of inelastic background, improving T2K's neutrino energy resolution, and ultimately the precision of its oscillation measurements. Since the event samples are so different between near and far detectors, and because water Cherenkov technology cannot entirely eliminate the inelastic background, additional measurements with fine-grained detectors are required. Ideally, these measurements would include not only exclusive inelastic reactions, but also quasi-elastic scattering, with a well-modeled efficiency relative to the inelastic channels. Because the reconstructed energy for inelastic background is lower than the true neutrino energy (the background "feeds down"), it is essential to measure these cross-sections both at and above the T2K beam energy. Chapters 2.2 and 2.3 discuss MINERνA's measurements of quasi-elastic and resonant cross-sections.

Calorimetric neutrino energy reconstruction

At neutrino energies above 1 GeV, calorimetric energy reconstruction is more efficient than kinematic reconstruction. In a low-threshold calorimetric device, the reconstructed or visible neutrino energy is simply the sum of all observed secondary particles' energies. For a ν_μ charged-current interaction, the muon energy can be determined by measuring its momentum by either range or curvature (if the calorimeter is magnetized), and the remaining activity can be summed to estimate the hadron energy. Scintillating calorimeters have a lower charged-pion detection threshold than Cherenkov detectors, so more of the total kinetic energy is visible for multi-pion interactions, which dominate the cross-section above a few GeV. As a result, neutrino energy reconstruction is less susceptible to bias from inelastic reactions than Cherenkov detectors.

For MINOS, the absolute energy scale for muons is fixed by knowledge of the steek plate thickness and muon energy loss processes. The thickness of each plate has been measured to better than 0.1% and they vary with an RMS of 0.4% [132]. In a muon test beam at CERN a 2% absolute scale calibration was achieved [133]. The hadronic and electromagnetic energy scales have been calibrated with test beams on a prototype detector at CERN, and have been measured relative to the muon scale within better than 5% [134, 135]. It is still necessary to translate from the raw response to pions and muons to the energy of interacting neutrinos, however.

At neutrino energies of a few GeV and below, three effects become significant in translation between visible and and neutrino energies. Uncertainties in these effects must be understood and included in any precise measurement of Δm^2_{23}. One effect, independent of the target nucleus, is the rest masses of the secondary charged pions. Since MINOS lacks the granularity to measure the multiplicity of final state particles, a hadron-energy dependent multiplicity distribution must be assumed. The second and third effects are due to secondary particle scattering or complete absorption in the nucleus. All three effects reduce the visible hadronic energy, which in turn lowers the reconstructed neutrino energy. Importance of these effects grows larger as the parent neutrino energy decreases,[96] due to strong enhancement of the pion–nucleon cross-section near the $\Delta(1232)$ resonace [137].

To quantify the magnitude of nuclear effects on measurement of Δm^2_{23} in a MINOS-like detector, a simple detector simulation was combined with the NEUGEN event generator [138] and NuMI fluxes at 735 km [139]. In this simulation the visible energy is simply defined as the sum of kinetic energies for all charged final-state particles, plus the total energy for the neutral pions, and photons, which are assumed to deposit all their energy as electromagnetic showers.

Figure 42 shows the variation of the ratio of visible to total neutrino energy for changes in nuclear absorption and scattering separately. In the plot on the left the target is assumed to be steel, and the parameter controlling pion absorption is set to zero or doubled. In the plot on the right all pion absorption is turned off, and the differences that remain are due to rescattering effects in steel, carbon, and lead. These rescattering effects have not been measured with neutrinos on high Z nuclei, so the rescattering variation can be considered as an error on extrapolation from the low-Z measurements that do exist. Because the ν_μ disappearance probability should be large, the far and near detector energy spectra will be very different, and these effects will only partially cancel in a ratio between near and far detectors. The extent to which they do not cancel represents a systematic error on Δm^2_{23}.

If these pion absorption Z extrapolation effects are treated as the total systematic uncertainty due to nuclear effects, we can compare it to the expected MINOS statistical error. In this more complete

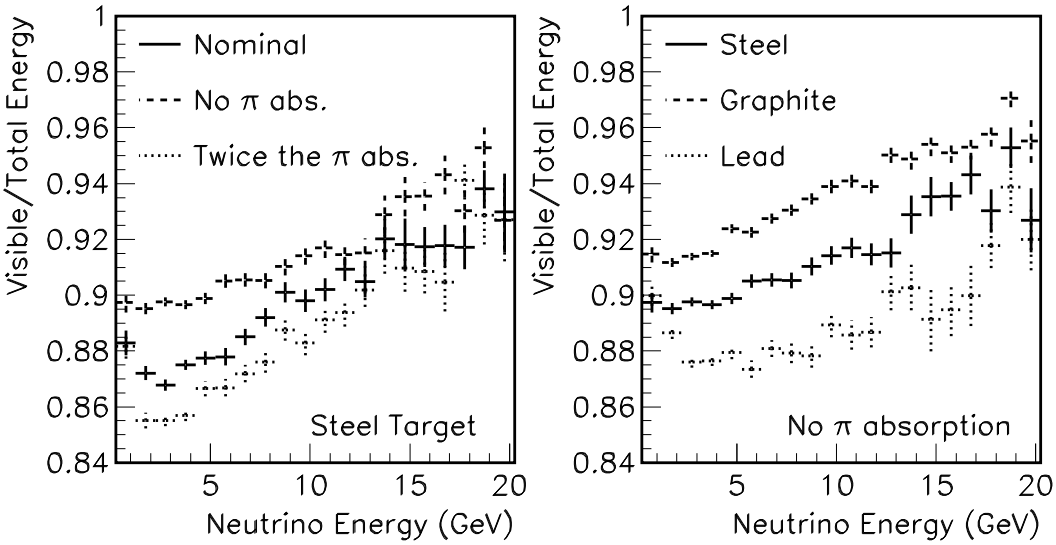

Figure 42: Ratio of visible (reconstructed) to true neutrino energy for several different models of nuclear effects. The left plot shows the ratio for steel (solid) with the nominal pion absorption, as well as the same ratio for the pion absorption turned off or doubled from what is expected. The right plot shows the differences the ratio for three different target nuclei, where pion absorption is turned off to isolate the effects of pion rescattering.

analysis, the detector acceptance must also be taken into account. One cut which could reduce the error due to nuclear effects significantly would be to require a minimum muon energy. The less visible energy attributable to hadrons, the smaller the relative effect of nuclear uncertainties on the total neutrino energy measurement. Requiring the muon to take up most of the energy in an event lowers efficiency, of course, and reduces the statistical power of the far-detector data sample. Here a minimum muon energy of 0.5 GeV was required, in an attempt to approximate the acceptance of a real analysis.

If the uncertainties from nuclear effects correspond to the differences in Figure 42, then for a 0.5 GeV muon momentum cut they induce a Δm^2_{23} error only slightly smaller than the statistical error expected by MINOS with 9×10^{20} protons on target (POT) (see Figure 43). This figure includes an estimate for the total systematic error that was made before the current MINOS result, where they report an additional large systematic due to the neutral current background [155]. We are currently reviewing how the NC error profile might be reduced with additional effort by MINOS and/or input from MINERνA.

MINERνA's contribution to reducing the rescattering errors would be very significant if the other large NC systematic error is reduced. It would have the same effect on the total error as obtaining 40% more protons on target. This is illustrated in the bottom plot in Figure 43, which shows the increased *effective* protons on target as a function of the true value for Δm^2. For a mass splitting near the MINOS best fit value of 2.7×10^{-3} eV^2, this is nearly 4×10^{20} POT, roughly an extra year of beam operation.

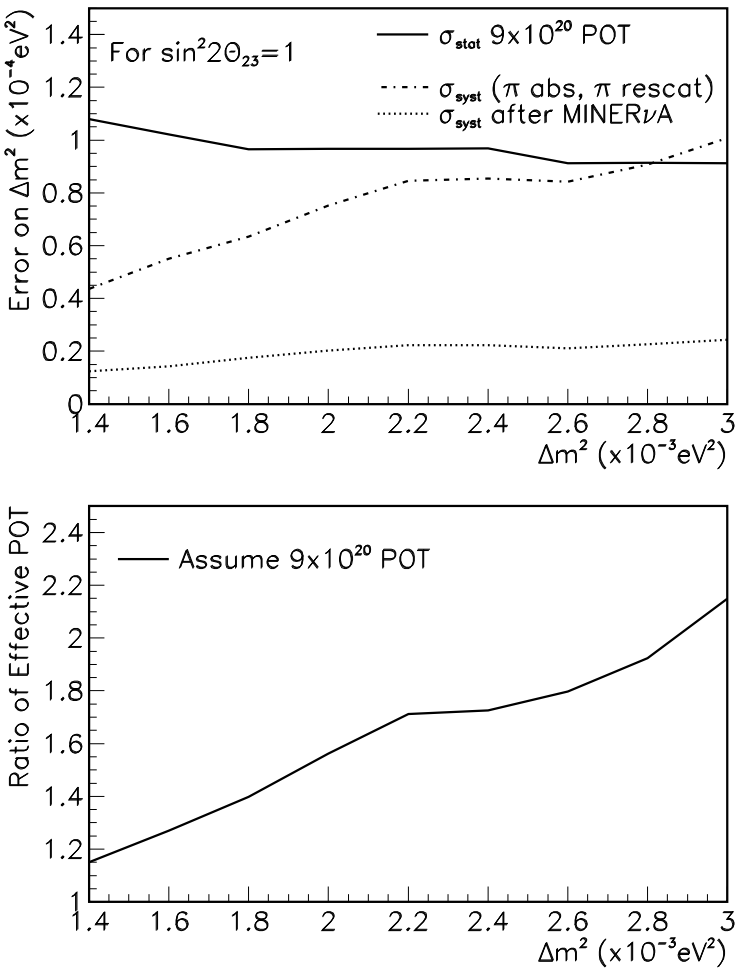

Figure 43: Top plot: projected size of errors on Δm^2 when MINOS has 9×10^{20} POT. Solid line is the expected statistical error. The other lines are estimates for the total systematic error before and after the reduction of the pion rescattering and absorption errors. Bottom plot, for the range of mass splittings near the MINOS value of 2.7×10^{-3} eV^2, this has the same effect on the total error as 40% more protons on target. These estimates were made before the current MINOS result, which reports an additional large systematic due to the neutral current background.

As described in Chapter 2.9, MINERνA will measure neutrino interactions on steel, carbon, and lead and collect between 400k and 2.5M events on each target (in addition to events on plastic CH) over a four year run. This represents an enormous improvement in both the statistics and the range of target nuclei over previous experiments, and would improve our level of understanding of nuclear effects dramatically. This is true with only a single year of operation, which would be the one relevant for the result from the full MINOS data. With sufficient data on several different nuclei, the error on Z extrapolation would be reduced since the nuclear models would be better constrained. The remaining

uncertainties on the detector energy scale are likely due to uncertainties in pion rescattering in steel. Systematic uncertainty in Δm^2_{23} with this new data in hand would be small compared to the statistical error.

2.10.3 ν_e Appearance

Signal and backgrounds

The goal of the next generation of neutrino oscillation experiments is to determine whether the last unmeasured neutrino mixing matrix element, (called $|U_{e3}|$ or $\sin\theta_{13}$) is non-zero. If θ_{13} is in fact non-zero future experiments could measure the neutrino mass hierarchy search for CP violation in the lepton sector. T2K and NOνAwill probe this matrix element by measuring the $\nu_\mu \rightarrow \nu_e$ oscillation probability at a "frequency" corresponding to Δm^2_{23}. The oscillation probability for $\nu_\mu \rightarrow \nu_e$ in vacuum can be expressed [148]

$$P(\nu_\mu \rightarrow \nu_e) = \sin^2\theta_{23}\sin^2 2\theta_{13}\sin^2\left(\frac{1.27\Delta m^2_{23}(eV^2)L(km)}{E_\nu(GeV)}\right) + ... \qquad (12)$$

where the additional terms not shown are due to small effects from the solar mass splitting, Δm^2_{12}.

Identifying ν_e appearance in a ν_μ beam is quite challenging for several reasons. From the CHOOZ reactor neutrino limit on $\sin^2 2\theta_{13}$ [150] the appearance probability must be less than about 5% at 90% confidence level. Also, the beams contain an intrinsic ν_e contamination as large as a few per cent. Finally, neutral-current and high-y charged-current ν_μ interactions can produce energetic π^0, leading to electromagnetic showers that may resemble a ν_e charged-current event.

T2K and NOνA will reduce some of these backgrounds significantly below the level in current long baseline experiments by using detectors optimized for electron appearance, and by placing those detectors off the beam axis. In two-body decay of the charged pion, the neutrino energy spectrum at small angles from the beam axis are narrower than the on-axis spectrum. Also, at these small angles the peak energy itself is reduced. The narrowest neutrino energy spectrum occurs when the far detector is placed at an angle corresponding to 90° in the pion center of mass. In this configuration, the ν_e flux comes from the three-body muon decays, so the intrinsic ν_e flux at lower energies does not increase at higher angles like the ν_μ flux does. Also, the neutral-current background is always a steeply falling function of visible energy because the outgoing neutrino always takes some fraction of the incoming neutrino's energy.

With this "off-axis" strategy, T2K and NOνA still expect some background after all analysis cuts, even in the absence of $\nu_\mu \rightarrow \nu_e$ oscillation. Measurement of the $\nu_\mu \rightarrow \nu_e$ probability requires accurate knowledge of this remaining background, and the cross-section and detection efficiencies for the ν_e signal.

Cross-section uncertainties with a near detector

Both T2K and NOνA will use near-detector measurements to predict the expected backgrounds at the far detector. In T2K, an on-axis near detector 280 m from the proton target will measure the spectrum and transverse beam profile, and at least one other off-axis detector will be focused on

cross-section measurements. There are also plans to build a water Cherenkov detector 2 km from the proton target, but even then near- and far-detector efficiencies may not be identical. For NOνA, the near detector will be very similar in design to the far detector, and can be placed in a wide range of angles with respect to the beam. By making the near detector similar, NOνA hopes to minimize uncertainties in the detector response and efficiency. However, because the near detector will be as coarse as the far, it is not optimized for cross-section measurements.

To see how any uncertainties (cross-section, detector acceptance, or flux) will arise in the far detector prediction based on the near detector data, it is useful to think about how the event samples are likely to change between near and far. At a near detector, the flux of muon neutrinos will have a very strong peak at a particular energy, while at the far detector that peak will (by design) have oscillated to mostly ν_τ. At these energies, ν_τ cannot produce charged-current interactions, only neutral-current. Neutral-current samples are likely to be similar from near to far, provided the near detector is at a similar off-axis angle. Electron neutrino events at the peak are primarily from muon decays in the beam, which occur on average substantially farther downstream than the pion decays. Therefore, the extrapolation from the near to far detector tends to be different for all three event samples. If the relative population of the background sample among different categories cannot be predicted accurately (due to cross-section, detector or flux uncertainties), the far detector extrapolation will be wrong.

The MINOS and NOνA near detectors will both provide important constraints on neutrinos coming from NuMI. However, neither will be able to measure the charged- and neutral-current near detector backgrounds precisely. A finer-grained detector with improved timing resolution will be extremely useful to distinguish these two contributions which change so dramatically between near and far detectors.

A quantitative case study of how cross-section uncertainties may not completely cancel between near and far detectors, was performed using the simulation for an early design [140] of NOνA. Although NOνA's final design will be different, the fundamental arguments remain unchanged: the mixture of contributing cross-sections at the far detector cannot, even in principle, be identical to the mixture at the near detector.

		QE	RES	COH	DIS
		cross-section Uncertainty			
		20%	40%	100%	20%
Process	Statistics	Composition after all cuts in far detector			
Signal ν_e	175 ($\sin^2 2\theta_{13} = 0.1$)	55%	35%	n/I	10%
NC	15.4	0	50%	20%	30%
$\nu_\mu CC$	3.6	0	65%	n/I	35%
Beam ν_e	19.1	50%	40%	n/I	10%

Table 4: Rate of signal and background processes in an earlier 50 kton NOνA far detector design, assuming $\Delta m^2_{23} = 2.5 \times 10^{-3}$ eV^2. Also listed are the present cross-section uncertainties for those processes. Charged-current coherent production was not included since it is should be unimportant compared to other charged-current processes.

The signal and background samples for the nominal 5 year run are listed in Table 4 along with the fractional contribution of each process to events of a given type passing all cuts, and the relative cross-section uncertainties [141]. Without a near detector, the total error on the background prediction from cross-section uncertainties, in the absence of ν_μ oscillation, is 16%, which is equal to the statistical error. For oscillation at the level indicated in the table, the statistical error on the probability would be 8%, while the errors from cross-section uncertainties alone are 31% .

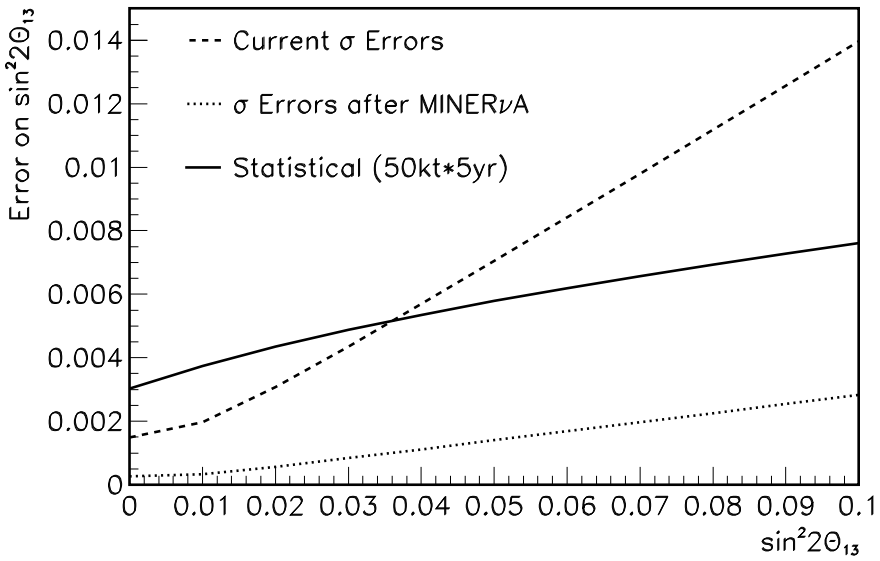

Figure 44: Statistical error, present cross-section systematic error, and post-MINERνA cross-section systematic error in NOνA measurement of $\sin^2 2\theta_{13}$, as a function of $\sin^2 2\theta_{13}$.

Figure 44 shows the projected error on $\sin^2 2\theta_{13}$ as a function of $\sin^2 2\theta_{13}$ itself, for present cross-section uncertainties. Should NOνA find a large signal, even in its first phase the measurement will be systematics limited with existing knowledge of relevant cross-sections. Chapters 2.2, 2.3 and 2.5 explain how different channels will be isolated, and give the size of the expected samples. MINERνA should be able to reduce cross-section uncertainties for NOνA to about 5% for all charged- and neutral-current deep-inelastic scattering processes, 10% for neutral-current resonant processes, and 20% for neutral-current coherent π^0 processes. If these uncertainties were achieved, then systematic errors due to cross-section uncertainties would be well below the statistical errors, as shown in Figure 44.

2.10.4 Conclusions

It is clear from even these preliminary studies that MINERνA will play an important and potentially decisive role in helping current and future precision oscillation experiments reach their ultimate sensitivity. To get the most precise values of Δm^2_{23} (which is eventually necessary to extract mixing angles and the CP-violating phase) our field must better understand and quantify the processes that

occur between interaction of an incoming neutrino and measurement of the outgoing particles in a detector. Although the issues are different depending on whether the detector is a water Cherenkov or calorimetric devices, in both cases more information is needed. Extracting mixing parameters like θ_{13} and ultimately the neutrino mass hierarchy and CP-violation requires much better understanding of resonant cross-sections. Even setting limits on these parameters will require better measurements of neutral-current processes. The cost of curing our present ignorance pales in comparison to the possibility that an entire generation of oscillation experiments might miss out on an exciting discovery or end in a morass of inconclusive, ambiguous, contradictory or even wrong results because we have failed to invest the effort needed to understand the most basic interactions of the particle whose exotic behavior they were built to study. Precision measurement of exclusive cross-sections and nuclear effects will finally put a field making tremendous strides in luminosity and statistical power on a sound systematic foundation.

Part I
Bibliography

References

[1] MINOS Collaboration, “MINOS Technical Design Report“, NuMI-NOTE-GEN-0337 (1998).

[2] N. V. Mokhov, “The MARS Monte Carlo”, FERMILAB FN-628 (1995); N. V. Mokhov and O. E. Krivosheev, “MARS Code Status”, FERMILAB-Conf-00/181 (20 00); http://www-ap.fnal.gov/MARS/.

[3] N. Mokhov and A. Van Ginneken, J. Nucl. Sci. Tech. **S1**, 172 (2000).

[4] M. Messier (private communication)

[5] Y. Hayato, To be published in *Proceedings of the Second Workshop on Neutrino-Nucleus Interactions in the Few-GeV Region (NUINT02)*, Irvine, California (2002).

[6] G. Ambrosini *et al.* [NA56/SPY Collaboration], Eur. Phys. J. C **10**, 605 (1999).

[7] P-907: Proposal to Measure Particle Production in the Meson Area Using Main Injector Primary and Secondary Beams, May 2000

(http://ppd.fnal.gov/experiments/e907/Proposal/E907_Propsal.html)

[8] NuMI Technical Design Handbook

(http://www-numi.fnal.gov/numiwork/tdh/tdh_index.html)

[9] K. Kodama *et al.,* Nucl. Phys. Proc. Suppl **98**, 43-47 (2001)

[10] M. Hasegawa *et al.* [K2K Collaboration], Phys. Rev. Lett. **95**, 252301 (2005) [arXiv:hep-ex/0506008].

[11] S. Kopp, Z. Pavlovic, and D. Indurthy, “Systematic Uncertainties in the NuMI Beam Flux” MINOS-doc-1283, (2006)

[12] C.H. Llewellyn Smith, Phys. Rep. 3C (1972).

[13] J. Arrington, nucl-ex[0305009].

[14] M. K. Jones *et al.*, Phys. Rev. Lett, 84, (2000) 1398 ; O. Gayou *et al.*, Phys. Rev. Lett, 88 (2002) 092301.

[15] J.J. Kelly, Phys. Rev. C70 (2004) 068202.

[16] R. Bradford, et al., hep[ex0602017].

[17] H. Budd, A. Bodek and J. Arrington, hep-ex[0308005].

[18] R. F. Wagenbrunn *et al.*, hep-ph[0212190].

[19] R. C. Merenyi *et al.*, Phys. Rev. D 45, 743 (1992)

[20] V. Bernard, L. Elouadrhiri, U.G. Meissner, J.Phys.G28 (2002), hep-ph[0107088].

[21] G. Zeller, private communication.

[22] K. Tsushima, Hungchong Kim, K. Saito, hep-ph[0307013].

[23] T. Kitagaki *et al.*, Phys. Rev. D26 (1983) 436.

[24] T. Kitagaki *et al.*, Phys. Rev. D42 (1990) 1331.

[25] S.J. Barish *et al.*, Phys. Rev. D16 (1977) 3103.
BNL D2

[26] N.J. Baker *et al.*, Phys. Rev. D23 (1981) 2499.

[27] W.A. Mann *et al.*, Phys. Rev. Lett. 31 (1973) 844.

[28] J. Brunner *et al.*, Z. Phys. C45 (1990) 551.

[29] M. Pohl *et al.*, Lett. Nuovo Cimento 26 (1979) 332.

[30] D. Allasia *et al.* Nucl. Phys. B **343** (1990) 285

[31] S.V. Belikov *et al.*, Z. Phys. A320 (1985) 625.

[32] S. Bonetti *et al.*, Nuovo Cimento 38 (1977) 260.

[33] K.L. Miller *et al.*, Phys. Rev. D26 (1982) 537.

[34] Glen Cowan, Statistical Data Analysis, Oxford Clarendon Press (1 998)

[35] H. Budd, A. Bodek and J. Arrington, hep-ex[0410055].

[36] D. Casper, Nucl. Phys. Proc. Suppl. 112 (2002) 161.

[37] R.A. Smith and E.J. Moniz, Nucl. Phys. B43 (1972) 605.

[38] Ghent Theory group in Belgium, Jan Ryckebusch (jan@inwpent5.UGent.be).

[39] D. Rein and L. M. Sehgal, Annals Phys. **133**, 79 (1981).

[40] M.H. Ahn, et al. (K2K), Submitted to PRD, hep-ex/0606032.

[41] T. Sato, D. Uno, and T.-S.H. Lee, Phys. Rev. C**67** 065201 (2003).

[42] E. Paschos, M. Sakuda, J.-Y. Yu, Phys. Rev. D**69** 014013 (2004).

[43] E. Paschos, et al., Proc. NuInt04 (L'Aquila), hep-ph/0408185.

[44] O. Lalakulich and E. Paschos, Phys. Rev. D**71** 074003 (2005).

[45] O. Lalakulich, E. Paschos, G. Piranishvili, Phys. Rev. D**74** 014009 (2006).

[46] T. Sato, et al., Proc. NuInt05 (Okayama),nucl-th/0601069.

[47] T. Kitagaki, et al., Phys. Rev. D**34** 2554 (1986).

[48] T. Kitagaki, et al., Phys. Rev. D**42** 1331 (1990).

[49] M. Hasegawa, et al. (K2K), Phys. Rev. Lett. **95** 252301 (2005).

[50] M. Wascko (MiniBoone), Proc. NuInt05 (Okayama), hep-ex/060 2050.

[51] D. Rein and L. M. Sehgal, Nucl. Phys. **B223**, 29 (1983).

[52] E. A. Paschos and A. V. Kartavtsev, (2003), hep-ph/0309148.

[53] Super-Kamiokande and K2K, C. Mauger, Nucl. Phys. Proc. Suppl. **112**, 146 (2002).

[54] BooNE, J. L. Raaf, Nucl. Phys. Proc. Suppl. **139**, 47 (2005), hep-ex/0408015.

[55] B. Z. Kopeliovich, Nucl. Phys. Proc. Suppl. **139**, 219 (2005), hep-ph/0409079.

[56] E. A. Paschos, A. Kartavtsev, and G. J. Gounaris, (2005), hep-ph/0512139.

[57] D. Rein and L. M. Sehgal, (2006), hep-ph/0606185.

[58] S. K. Singh, M. Sajjad Athar, and S. Ahmad, (2006), nucl-th/0601045.

[59] MiniBooNE, J. Monroe, Nucl. Phys. Proc. Suppl. **139**, 59 (2005), hep-ex/0408019.

[60] K2K, T. Ishida, Prepared for 1st Workshop on Neutrino - Nucleus Interactions in the Few GeV Region (NuInt01), Tsukuba, Japan, 13-16 Dec 2001.

[61] N.J. Baker *et al.*, Phys. Rev. D **24**, 2779 (1981).

[62] A. Alavi-Harati *et al.*, Phys. Rev. **87** 132001 (2001).

[63] P.G. Ratcliffe, Phys. Rev. **D59**, 014038 (1999).

[64] N. Cabibbo *et al.*, Semileptonic Hyperon Decay and CKM Unitarity, [arXiv:hep-ph/0307214] (July 2003).

[65] T. Alexopoulos *et al.* (KTeV Collaboration), Phys. Rev. Lett. **93**, 181802 (2004).

[66] T. Nakano *et al.*, [arXiv:hep-ex/0301020]; V.V. Barmin
em et al., [arXiv:hep-ex0304040]; S. Stepanyan [arXiv:hep-ex/0307018].

[67] R. Jaffe and F. Wilczek, Di-quarks and Exotic Spectroscopy, [arXiv:hep-ph/0307341] (July 2003).

[68] S. Kuhlmann *et al.*, Phys. Lett. B **476**, 291 (2000).

[69] H. Deden and et al., [Gargamelle Neutrino Collaboration], "Experimental Study Of Structure Functions And Sum Rules In Charge Changing Interactions Of Neutrinos And Anti-Neutrinos On Nucleons," Nucl. Phys. **B85**, 269 (1975).

[70] K. Varvell *et al.* [BEBC WA59 Collaboration], Z. Phys. C **36**, 1 (1987)

[71] M. Shifman, Handbook of QCD, Volume 3, 1451, World Scientific (2001)

[72] F. E. Close and N. Isgur, Phys. Lett. B **509**, 81 (2001)

[73] W. Melnitchouk, R. Ent and C. Keppel, Phys. Rept. **406**, 127 (2005) [arXiv:hep-ph/0501217].

[74] I. Niculescu *et al.*, Phys. Rev. Lett. **85**, 1186 (2000)

[75] C. E. Keppel, *Prepared for Exclusive Processes at High Momentum Transfer, Newport News, Virginia, 15-18 May 2002*

[76] J. Arrington, R. Ent, C. E. Keppel, J. Mammei and I. Niculescu, arXiv:nucl-ex/0307012 (submitted to Phys. Rev. Lett.)

[77] A. Fantoni [HERMES Collaboration], Eur. Phys. J. A **17**, 385 (2003).

[78] I. Niculescu *et al.*, Phys. Rev. Lett. **85**, 1182 (2000).

[79] A. Bodek and U. K. Yang, arXiv:hep-ex/0203009.

[80] D. Dolgov *et al.* [LHPC collaboration], Phys. Rev. D **66**, 034506 (2002) [arXiv:hep-lat/0201021].

[81] I. Niculescu, J. Arrington, R. Ent and C. E. Keppel, Phys. Rev. C **73**, 045206 (2006) [arXiv:hep-ph/0509241].

[82] X. Ji, Phys. Rev. Lett. **78**, 610 (1997).

[83] X. Ji, Phys. Rev. **D55**, 7114 (1997).

[84] A. V. Radyushkin, Phys. Lett. **B380**, 417 (1996).

[85] A. V. Radyushkin, Phys. Lett. **B385**, 333 (1996).

[86] J.C. Collins, L. Frankfurt, and M. Strikman, Phys. Rev. **D56**, 2982 (1997).

[87] A. V. Radyushkin, Nucl. Phys. **A711**, 99 (2002).

[88] M. Vanderhaeghen, Nucl. Phys. **A711**, 109 (2002).

[89] M. Diehl, hep-ph/0307382 (2003).

[90] C. Munoz Camacho, et al. nucl-ex/0607029 (2006).

[91] A. Psaker, W. Melnitchouk and A. Radyushkin, in preparation.

[92] D. Drakoulakos *et al.* [Minerva Collaboration], fine-grained detector in the NuMI beam," arXiv:hep-ex/0405002. Pgs. 99 - 108, 192 - 200.

[93] B.Z. Kopeliovich, hep-ph/0409079.

[94] M.K. Jones *et al.*, Phys. Rev. **C48**, 2800 (1993); R.D. Ransome *et al.*, Phys. Rev. **C46**, 273 (1992); R.D. Ransome *et al.*, Phys. Rev. **C45**, R509 (1992).

[95] D. Rowntree *et al.*, Phys. Rev. **C60**, 054610 (1999); B. Kotlinksi *et al.*, Eur. Phys. J. **A9**, 537 (2000).

[96] E. A. Paschos, M. Sakuda, I. Schienbein and J. Y. Yu, arXiv:hep-ph/0408185.

[97] M. Arneodo, Phys. Rept. **240**, 301 (1994).

[98] G. Piller and W. Weise, Phys. Rept. **330**, 1 (2000).

[99] B. L. Ioffe, V. A. Khoze, and L. N. Lipatov, *Hard processes: Phenomenology, Quark-Parton Model* (Elsevier Science Publishers, North Holland, 1984).

[100] G.B. West, Ann. Phys. **74** (1972) 464.

[101] S. V. Akulinichev, S. A. Kulagin, and G. M. Vagradov, Phys. Lett. B **158**, 485 (1985); S. V. Akulinichev, S. Shlomo, S. A. Kulagin, and G. M. Vagradov, Phys. Rev. Lett. **55**, 2239 (1985).

[102] S. A. Kulagin, Nucl. Phys. A **500**, 653 (1989).

[103] C. Ciofi degli Atti and S. Liuti, Phys. Rev. C **41**, 1100 (1990).

[104] F. Gross and S. Liuti, Phys. Rev. C **45**, 1374 (1992).

[105] S. A. Kulagin, G. Piller and W. Weise, Phys. Rev. C **50**, 1154 (1994).

[106] S. A. Kulagin, W. Melnitchouk, G. Piller, and W. Weise, Phys. Rev. C **52**, 932 (1995).

[107] S. A. Kulagin, Nucl. Phys. A **A 640**, 435 (1998).

[108] W. Melnitchouk, A. W. Schreiber and A. W. Thomas, Phys. Rev. D **49**, 1183 (1994).

[109] J. Gomez, *et al.*, Phys. Rev. D **49**, 4348 (1994).

[110] S. I. Alekhin, S. A. Kulagin and S. Liuti, Phys Rev. D **69**, 114009 (2004).

[111] S. A. Kulagin and R. Petti, paper in preparation.

[112] T. H. Bauer, R. D. Spital, D. R. Yennie and F. M. Pipkin, Rev. Mod. Phys. **50**, 261 (1978) [Erratum-ibid. **51**, 407 (1979)].

[113] C. A. Pickety, and L. Stodolsky, Nucl. Phys. B **15**, 571 (1970).

[114] S. L. Adler, Phys. Rev. **135**, B963 (1964).

[115] R. J. Glauber, Phys. Rev. **100**, 242 (1955).

[116] V. N. Gribov, Sov. Phys. JETP **29**, 483 (1970) [Zh. Eksp. Teor. Fiz. **56**, 892 (1969)] ; Sov. Phys. JETP **30**, 709 (1970) [Zh. Eksp. Teor. Fiz. **57**, 1306 (1969)].

[117] B. Z. Kopeliovich, and P. Marage, Int. J. Mod. Phys. A **8**, 1513 (1993).

[118] S. A. Kulagin, arXiv:hep-ph/9812532.

[119] E. A. Paschos and L. Wolfenstein, Phys. Rev. D **7**, 91 (1973).

[120] G. P. Zeller *et al.* [NuTeV Collaboration], Phys. Rev. Lett. **88**, 091802 (2002) [Erratum-ibid. **90**, 239902 (2003)] [arXiv:hep-ex/0110059].

[121] S. A. Kulagin, Phys. Rev. D **67**, 091301 (2003) [arXiv:hep-ph/0301045].

[122] S. A. Kulagin, arXiv:hep-ph/0406220.

[123] S. A. Kulagin, arXiv:hep-ph/0409057.

[124] D. H. Lu, A.W. Thomas, and K. Tsushima, arXiv:nucl- th/0112001, K. Tsushima, H. Kim, and K. Saito, Phys. Rev. C **70**, 038501 (2004)

[125] J.J. Aubert et al., Phys. Lett. **123B**, 275 (1983); D.F. Geesaman, K. Saito, and A.W. Thomas, Annu. Rev. Nucl. Part. Sci. **45**, 337 (1995).

[126] B. Buck and S.M. Perez, Phys. Rev. Lett. **50**, 1975 (1983).

[127] S. Dieterich, et al., Phys. Lett. B **500**, 47 (2001), S. Strauch et al., Phys. Rev. Lett. **91**, 052301 (2003).

[128] JLab experiment E3-104, co-spokespersons R. Ent, R. Ransome, S. Struach, P. Ulmer. `http://www.jlab.org/exp_prog/proposals/03/PR03-104.ps`

[129] C.H.Q. Ingram, Nucl. Phys. A **684**, 122 (2001).

[130] M. K. Jones *et al.*, Phys. Rev. C **48**, 2800 (1993).

[131] M. Nakahata *et al*, Nucl. Instrum. Meth. **A421**, 113 (1 999); E. Blaufuss *et al*, Nucl. Instrum. Meth. **A458** 638 (2001).

[132] M. Diwan and J. Nelson, NuMI-NOTE-STEEL-0639 (2000)

[133] PhD Thesis of C. Smith, University College London, London, 2002 *Calibration of the MINOS Detectors and Extraction of Neutrino Oscillation Parameters*; PhD Thesis of R. Nichol, University College London, London, 2003 *Calibration of the MINOS Detectors*

[134] PhD thesis of M. A. Kordosky, University of Texas at Austin, August 2004 *Hadronic Interactions in the MINOS Detectors*

[135] PhD thesis of P. L. Vahle, University of Texas at Austin, August 2004 *Electromagnetic Interactions in the MINOS Detectors*

[136] E. A. Paschos, L. Pasquali and J. Y. Yu, Nucl. Phys. B **588**, 263 (2000) and E. A. Paschos, J. Y. Yu and M. Sakuda [arXiv:hep-ph/0308130].

[137] D. Ashery *et al.*, Phys. Rev. **C23**, 2173 (1981).

[138] H. Gallagher, Nucl. Phys. Proc. Suppl. **112**, 188 (2002)

[139] NuMI Fluxes courtesy of Mark Messier

[140] The simulation assumed the active material was resistive plate chambers and the absorber was particle board (hydrocarbons).

[141] G.P.Zeller, submitted to proceedings of 2nd International Workshop on Neutrino - Nucleus Interactions in the Few GeV Region (NUINT 02), Irvine, California, 12-15 Dec 2002 [hep-ex/0312061]

[142] Kamiokande Collaboration, S. Hatakeyama *et al.*, Phys. Rev. Lett. **81** (1998) 2016; Soudan-2 Collaboration, W. W. Allison *et al*, Phys. Lett. **B 449** (1999) 137; MACRO Collaboration, Ambrosio *et al*, Phys. Lett. **B434**, 451 (1998)

[143] Y. Fukuda et al., *Phys. Rev. Lett.* **81** (1998) 1158; Erratum **81** (1998) 4279, B.T. Cleveland et al., *Astrophys. J.* **496** (1998) 505. W. Hampel et al. (GALLEX Collaboration), *Phys.Lett.* **B 447** (1999) 127., J.N. Abdurashitov et al. (SAGE Collaboration), *Phys. Rev.* **C 60** (1999) 055801 [astro-ph/9907113]

[144] Q.R. Ahmad *et al.* Phys.Rev.Lett.**89** (2002) 011302 nucl-ex/0204009

[145] Y. Fukuda *et al.*, Phys.Rev.Lett.**81** (1998) 1562 [hep-ex/9807003]; M. Sanchez et al., Phys. Rev. **D 68**, 113004 (2003)

[146] KamLAND Collaboration (K. Eguchi et al.), Phys. Rev. Lett.**90** (2003) 021802 [hep-ex/0212021]

[147] K2K Collaboration (M.H. Ahn et al.), Phys.Rev.Lett.**90** (2003) 41801 [hep-ex/0212007]

[148] B. Pontecorvo and J. Exptl, Theoret. Phys. **34** 247 (1958); Z. Maki, M. Nakagawa and S. Sakata, Prog. Theor. Phys. **28**, 870 (1962).

[149] M. Maltoni *et al*, submitted to New J. Phys, [hep-ph/0405172]

[150] By CHOOZ Collaboration (M. Apollonio et al.), Phys.Lett.**B466** (1999) 415 [hep-ex/9907037]

[151] W. Grimus and L. Lavoura, Phys. Lett. **B572**, 189 (2003); A. Aranda, C.D. Carone, R.F. Lebed, Phys. Rev. **D62**, 016009 (2000).

[152] "A Long Baseline Neutrino Oscillation Experiment at Fermilab", E.Ables *et al*, FERMILAB-PROPOSAL-0875, Feb. 1995, 241pp.

[153] "NOVA: Proposal to build an Off-Axis Detector to Study $\nu_\mu \rightarrow \nu_e$ oscillations in the NuMI Beamline", I. Ambats *et al.*, FERMILAB-PROPOSAL-0929, Mar 2004.

[154] Y. Itow *et al*, "The JHF-Kamioka Neutrino Project", KEK report 2001-4, June 2001. [hep-ex/0106019]

[155] J. Nelson, "MINOS Oscillation Results", Neutrino 2006, Santa Fe, NM, June, 2006.

bibitemingram C.H.Q. Ingram, Nucl. Phys. A **684**, 122 (2001).

[156] E. Gallas & J. Li., "Polishing Optical Fibers for the D0 ICD in Run II", FNAL-TM-2062, 1998.

[157] The MINERνA Collaboration,

Proposal to perform a high-statistics neutrino scattering experiment using

a fine-grained detector in the NuMI beam, Fermilab Proposal P-938, e-print

hep-ex/0405002; see Sect. 16.5.2.

[158] M. Bonkowski, *Magnetic Field Measurement Results*,

MINERνA note MINERvA-doc-88-v1, (measurements of December 2004).

[159] D. Cherdack and W.A. Mann, *Magnetic Shielding Capabilities*

of the MINERvA PMT Box, MINERνA note MINERvA-doc-164-v1.

[160] P. Adamson, et al., Nucl. Inst. Meth. A**492**,

325 (2002).

[161] P. Shanahan, priv. comm. (Nov., 2005).

[162] A. Cabrera, et al., NuMI-934 internal report.

[163] P. Harris (Sussex Univ.) provided excellent

guidance and some pieces necessary for prototyping.

[164] "MCM II and the Trip Chip", J. Estrada, C. Garcia, B. Hoeneisen and P. Rubinov, August 2002, FERMILAB-TM-2226.

[165] MINOS Technical Design Report, Chapter 5: Scintillator detector fabrication, Fermilab Public

[166] Specification 9216.000-ES-435360. Available through the Fermilab Particle Physics Division.

[167] Specification 9216.000-ES-435361. Available through the Fermilab Particle Physics Division.

[168] R. Bradford, *Assembly Roadmap from Prototype Studies*, posted to FNAL MINERνA Docdb as document number 561.

[169] R. Flight, *Detector Assembly Drawings, as of 11/15/05*, available in MINERνA Docdb as document number 226.

[170] R. Flight, *Mapper Drawings*, available in MINERνA Docdb as document number 897.

[171] R. Flight, *Fiber Routing Update*, available in MINERνA Docdb as document number 741.

[172] D. Casper, "The nuance Neutrino Physics Simulation, and the Future", *http://nuint.ps.uci.edu/nuance/files/nuance_nuint01.pdf*

[173] O. Benhar, [arXiv:nucl-th/0307061].

[174] K. Ruddick (private communication).

[175] L. Mualem (private communication).

[176] MINOS Collaboration, P. Adamson *et al.,* IEEE Trans. Nucl. Sci. **49**, 861 (2002).

[177] R. Fruhwirth, Nucl. Inst. Meth. **A262**, 444 (1987).

[178] "Studies of Extruded Plastic Scintillator for MINOS", Karol Lang and Todd Soesby, NuMI-NOTE-L-250, Feb 1997.

[179] M. Andrews, MINERνA Hazard Assessment, MINERνA Document 310 (2006)

[180] MINERνA Project Management Plan, MINERνA Document 59 (2006)

[181] L. Mualem, *The case for using Cesium-137 on the module mapper instead of Co-60*, NuMI-L-0653 (2000)

[182] American Institute of Steel Construction, Inc., *Manual of Steel Construction, Allowable Stress Design*, Ninth Edition

[183] American National Standard ANSI/ASME B30.20, *Below-the-hook lifting devices*

[184] Gage-Babcock & Associates, Inc. *Fire Protection/Life Safety Recommendations for the Fermilab NuMI Project* (1998)

[185] Fermilab ES&H Manual, Chapter 5032.2, Guidelines for the Design, Review and Approval of Liquid Cryogenic Targets (1995)

[186] J. Livengood, Letter to G. Brown, *National Environmental Policy Act (NEPA) Determination at Fermi National Accelerator Laboratory - "Main Injector Neutrino ExpeRiment ν–A(MINERνA)"* MINERνA Document 311 (December 2, 2005)